Biomagnetic field measurements and their interpretation using the dipole in a sphere model.

Thesis

BIOMAGNETIC FIELD MEASUREMENTS AND THEIR INTERPRETATION USING THE DIPOLE IN A SPHERE MODEL

PhD Thesis

September 1987

Balwinder S Janday MSc

Dept Of Physics

Open University

Milton Keynes

Date of submission: September 1987

Date of award: 23 February 1988

Biomagnetic Field Measurements And Their Interpretation Using The Dipole In A Sphere Model

Abstract.

Although biomagnetism has advanced considerably in the last twenty years in terms of instrumentation and application, the fundamental requirement of relating the detected field to the underlying sources still has to rely on simple models. Most often the current dipole in a conducting sphere model is used. The exact geometry of the system under study is often ignored and clinically crucial decisions may be taken without understanding the limitations of this model.

The work described in this thesis assesses those limitations, first by analysis of physical model generated data using the dipole in a sphere model. Dipole location, orientation, strength and sphere centre location were parameters used to fit calculated data to real data iteratively. These calculations were fully corrected for detector coil size and geometry. The systems investigated included whole and partial spheres and gel filled skulls. Dipoles placed in close proximity to boundaries were more difficult to fit to the dipole in a sphere model than those further away. As the boundary itself became more distinctly non- spherical, this difficulty increased. A goodness of fit parameter (R) was defined indicating

accuracy of signal fitting. Surprisingly, in some examples, a low R value could be obtained for a poor set of predicted dipole parameters. However, if the fitting procedure incorporates the model sphere centre position as additional fitting parameters and a search is made through model sphere centre parameter space the effect of these (fortuitously) low R values could be avoided.

The second half of the work applies the lessons of the first half to real biological systems. Magnetic fields emanating from a developing chick egg change during development. The egg provides a convenient system to investigate ionic fluxes involved with development and to test the appropriateness of the single dipole in a conducting sphere model in determining the source generators.

Finally the human visual evoked response was used to investigate the retinotopic representation of the cortex. The source locations suggested by this work using magnetic fields support earlier work which used electrical potential measurements, though a significant temporal difference of peak power between the two sets of sources is predicted by analysis of the data available from the two techniques.

Acknowledgment

This work has seen brain related research at the Open University Biomagnetism Lab evolve from nothing to significant contributions at international meetings within three years. The main thrust has been the improvement of modelling techniques which utilized data from novel experiments.

Being a multidisciplinary project, many people from the physics, biology and electronics departments made contributions ranging from encouragement to bending over backwards to help. I take this opportunity to thank them all. I am also indebted to the staff of the EEG department at St Thomas' Hospital, London and Aston Clinical Research Unit, Birmingham for initial training on evoked potentials. The radiography department of Milton Keynes General Hospital provided facilities to x-ray the skull models in order to determine exact location of the dipole.

The various stages of the project often threatened to engulf each other but this was averted by the expert guidance of Dr S J Swithenby, director of the biomagnetism group. He also played a major role in the development of the modelling programs. I take this opportunity to thank my friend Steve Swithenby for listening to me, teaching me (at times quite basic maths

and physics), encouraging me and being patient. Thanks also to David Grimes who wrote much of the data acquisition program used in the chick experiments, and to Roger Bence and Martin Sydee for building many weird and wonderful gadgets during my time at the Open University.

My special thanks go to Anji who was always on hand as expert subject, artist, tea maker and friend.

Contents

List of illustrations

Figure 7 Moving platform system for making 'dc' magnetic field measurements. x and y direction potentiometers determine exact position of the platform. The SQUID dewar can be moved in the z direction

Figure 8 The data acquisition involves scanning the sphere in a plane parallel to the plane of the detector pick up coil rather than scanning the pick up coil tangential to the spherical surface

Figure 9 Effects of adding random noise on the predicted dipole parameters using computer generated data. N/S is the ratio ([ave noise^2]$^{0.5}$/[ave signal^2]$^{0.5}$)

Figure 10 Cross section through Cuffin's head model and fissure. Three source locations are shown (situated 0.25 cm from the fissure)

Figure 11 Dipole within a conducting sphere. The inset shows details of dipole construction

Figure 12 Apparatus for energising the dipole and detecting the magnetic field signal

List Of Publications

Janday, B S and Swithenby, S J
Localisation of magnetoencephalographic (MEG) sources. Soc Proc. Electro Clin Neurophysiol Vol 30 p64 1986

Janday, B S and Swithenby, S J
Analysis of magnetoencephalographic data using the homogeneous sphere model: empirical tests. Phys Med Biol Vol 32 p105-113 1987

Janday, B S and O'Connell, J
Locating current sources within skulls using magnetometry. Radiography Vol 53 p287-92 1987

Janday, B S and Swithenby, S J
Use of the symmetric sphere model in MEG analysis. IN Functional Imaging - a goal for biomagnetism . Eds L. Narici and G.L. Romani. In press

Janday ,B S ;Swithenby, S J and Thomas, I M
Combined magnetic field and and electric potential investigation of the visual pattern reversal response. 6th International Conference on Biomagnetism. Tokyo (in press) 1987

Janday et al
DC magnetic fields from developing chick eggs. In Prep.

Janday et al

Retinotopic organisation of the cerebral cortex revealed by combined magnetic field and electric potential measurements. Submitted Electro Clin Neurophysiol.

Biomagnetic Field Measurements And Their Interpretation Using The Dipole In A Sphere Model

INTRODUCTION

1.1 Biomagnetism

Ionic currents and magnetic materials within an organism produce weak but measurable magnetic fields outside the organism. Considerable interest has been shown in developing techniques of measuring such fields for, among other reasons, they are non invasive in nature and are independent of frequency from dc to radio-frequencies. Biomagnetism is the study of magnetic fields arising from biological organisms. This thesis is concerned generally, with the development of biomagnetic methods in terms of techniques, fields of study and, most importantly, methods of modelling.

A crucial step in biomagnetic investigations is the identification of the underlying sources from the detected magnetic fields. This requires the assumption of a physical model for the organism. One of the most promising models is one in which the biological system is considered to be a uniformly conducting sphere. The source is assumed to be a current dipole (i.e a current source and sink linked by an infinitesimal current element). This idealized model has been applied by many authors to data from real systems where the conducting volume is not spherical and the source not necessarily a single dipole. Although useful to a first approximation, full justification for using this model has not been

established.

Within this context, a major theme of the present study was to investigate this model. In particular, we sought to establish the accuracy with which the dipole parameters could be predicted, and the means of identifying when accurate predictions were being made. Both ideal and non ideal (e.g non spherical) systems were investigated. These studies were carried out on artificial physical model systems. With the better understanding we gained of the interaction of the model and the analysis, real systems could be studied.

One such system we have considered is the visual cortex. Data obtained from pattern reversal checkerboard stimulated subjects were analysed using the dipole in a sphere model in an investigation of the effects of stimulating different regions of the retina on the response recorded over the primary visual cortex and hence on the activity of the cortex.

In another study, we exploited the dc capability of SQUID (Superconducting QUantum Interference Device) magnetometers in measurements of the dc magnetic fields outside developing chick eggs. The sources were unknown but analysis of the data was used to postulate possible sources. The work was extended by mechanically and chemically perturbing the developing system and by

correlating the observations with morphological development.

These two biological studies were of interest in their own right but they also served to demonstrate what is achievable with a dipole in a sphere model as the basis for analysis. Some contextual knowledge is required before the studies reported below can be evaluated. Ideas of basic biology are needed to give a context to how charge movements may arise; simple instrumental issues must be raised; and the link between currents and electromagnetic fields needs to be reviewed. These are dealt with in the following three sub-sections in the introduction to the thesis.

1.2 Basic Biology

Many of the processes of life involve the movement of charged particles, e.g. ions or proteins. Any net movement of charge constitutes an electric current. In this discussion of 'basic biology', I will outline where such currents occur.

The currents are most familiar in the context of action potentials in which information is transmitted in the form of short lived electrical pulses along the excitable membranes of nerves and muscles.

Although electrical potential differences exist across the membranes of essentially all cells, excitable membranes are, in the present context, those that exhibit a profoundly non-linear electrical response to an appropriate stimulus e.g a voltage pulse. If the stimulus intensity is below a threshold level, currents flow but the stimulus produces no significant change in membrane properties. However, if the stimulus intensity exceeds the threshold, dramatic changes in membrane properties take place, large ion fluxes occur and the trans-membrane potential alters markedly. This 'excitation' is self-propagating in that, once stimulated, the region of excited membrane stimulates neighbouring regions and the 'action-potential' pulse moves spontaneously outwards from the first point of excitation. In this way an excitation may be passed along the entire length of a cell, for

example a nerve axon, without decrement. Such an excitation pulse can pass to adjacent cells through chemical mediation at junctions or 'synapses'. The chemical transmitter substances are released by the first excited cell and passed to the second cell causing its membrane to be excited.

Depolarisation of cells is, generally, associated with rapid fluxes of sodium and potassium ions. Ion fluxes associated with both depolarisation and repolarisation can be considered as sources of many of the detectable magnetic fields outside the body.

Changes in the transmembrane potentials of groups of cells are responsible for the electric potentials and magnetic fields associated with activity of the brain. Both transient and longer lived phenomena can be detected. Neurons respond to excitations reaching them via synaptic connections in one of three ways, all of which give rise to measurable extra cellular potentials.

1 A relatively slow decrease (depolarisation) in the magnitude of the transmembrane resting potential.

2 A relatively slow increase (hyperpolarisation) of the resting potential.

3 The triggering of an action potential which propagates automatically once the threshold depolarisation is surpassed.

The first two types of responses are called 'graded potentials'. Neurons communicate with each other, at least over short distances, by all three types of potentials. Some early features of evoked responses occurring soon after stimulation but prior to cortical involvement may primarily be summated action potentials. However, many features of the electroencephalogram (EEG - electrical activity recorded from ionic flow within the brain) and the magnetoencephalogram (MEG -magnetic activity recorded as a result of ionic flow within the brain) are thought to arise from summated graded potentials. The limitations of EEG methods are described later.

For evoked responses the magnitude of the response is much smaller than the magnitude of the naturally occurring background activity of the brain during rest, and minute compared with muscular and cardiac activity also present. This is discussed further in a later section dealing with evoked responses.

In addition to the currents associated with excitable membranes, there are are other large quasi-static ionic currents present in biological organisms. Primarily we

are interested in those currents that are linked to development and regeneration. Current densities typically $1\mu Acm^{-2}$ are known to pass through many developing organisms, for example fucoid eggs, cecropia follicles, lily pollen grains and chick embryos (Jaffe and Nuccitelli 1971). The locations, strengths and timing of these currents correlate with the positions and timings of significant developmental activity. These developmental currents may act as a form of feedback by which an inhomogeneous distribution of charged cellular constituents is created. Developmental biologists are interested in currents because they may help to answer questions such as why an asymmetrical organism grows from a symmetrical, non-polar ovum. In addition to developmental occurrance there are also currents that can be detected during regeneration of, for example, amphibian limbs. (A large sodium current ($\simeq$10-100 μAcm^{-2}) leaves the stumps of amputated newt limbs for about a week after amputation. Blocking of this current inhibits regeneration while augmenting it, stimulates regeneration, -Jaffe and Stern 1982)

The role of ionic currents in the regeneration and development of biological systems is not completely understood and is highly controversial. Only electrical potential measurements have been carried out to date and the main investigative tool thus far has been the vibrating probe, which is capable of measuring local

current densities as small as 0.1 μAcm^{-2} with a spatial resolution of approximately 30 μm. Unfortunately, this technique is limited to electrolyte inhabiting organisms, only detects external current flow, and cannot therefore deal with the complete organism.

Attempts have been made to use other electrode techniques on complete organisms, but it is intrinsically difficult to monitor slow developmental activity using electrodes. Attachment of an electrode requires direct electrolytic contact, and therefore, a measurement within an organism always involves both mechanical damage and electrolytic contamination. In any study of regeneration or injury currents, the validity of such an invasive measurement must be suspect. As well as this fundamental limitation there is the technical problem in quasi dc measurements of overcoming drift.

Problems of contact potentials, drift, membrane formation over the electrode, puncturing and generally invasive measurements can, in principle, be avoided by using a SQUID magnetometer and looking at the magnetic fields outside the organism. The magnetic field created depends on the current density and the area of active membrane involved. In some cases, large current densities can be shown to be present (for example in Drosophila eggs) but the magnetic fields are too small to be detected as the ionic fluxes cover a very small area. However, a current

density of 1 μAcm^{-2} flowing in a $1cm^3$ region would give rise to a magnetic field of $\simeq$ 2.5 pT at a distance of 2cm from the source. This is easily detectable. (The relationship between current and field is developed later.)

Finally in this brief introduction of ionic current sources of biomagnetic signals, we note that, in general, the magnetic signals are very small, ranging from 100 pT from the heart to 100 fT from the brain. Table 1 shows typical amplitudes of some biomagnetic signal sources. It is clear that very sensitive magnetometers are required. SQUID magnetometer operation will be discussed later.

Table 1

Approximate amplitudes of some biomagnetic signals (recorded at an appropriate point outside the body)

Activity	Amplitude(pT)
Evoked Magnetoencephalogram (MEG)	0.1
Spontaneous MEG	1
Foetal Magnetocardiogram (FMCG)	1
Chick egg	5
Human leg	10
Magnetocardiogram (MCG)	50
Diamagnetic *	10000

*Diamagnetic response of body tissue to a field of 10^{-2}T

1.3 Detecting Magnetic Fields Using SQUID Magnetometers.

The very small magnitude of biomagnetic signals dictates that the most sensitive instruments be employed for field detection. The SQUID magnetometer is a device for converting a small magnetic flux change ($\Delta\Phi_{in}$) through a detection coil into a voltage output change ΔV_{out} such that

$$\Delta V_{out} \propto \Delta\Phi_{in} \qquad (1)$$

As the SQUID responds only to changes in flux, it has no quantifiable base line and, of itself, does not measure absolute field values. Ways around this problem are indicated later.

Physically a SQUID consists of a superconducting ring with one or more weak links (thin insulating regions separating the superconducting regions). Superconducting rings have the property of quantizing the magnetic flux through them, one flux quantum being h/2e, where h is Planck's constant and e is the electronic charge, i.e

$$\Phi_{ring} = \frac{nh}{2e} \qquad (2)$$

Flux conservation laws apply so that, if the flux imposed on a superconducting ring is changed, then a screening current I_s will flow in the ring so as to maintain the flux quantization condition.

$$LI_s = \Phi_{imposed} - \Phi_{ring} \qquad (3)$$

where L is the inductance of the ring.

Electron pairs can tunnel across the weak link from one superconducting side to another enabling a zero voltage current to pass. However, at a critical or maximum current (I_c), the weak link ceases to be superconducting and energy is dissipated.

Our SQUID system is an rf SQUID in which there is just one weak link (Figure 1). The operation of the device is complicated but may be briefly described as follows. The SQUID is inductively coupled to an rf tank circuit (fed from a constant current rf oscillator and attenuator system), which modulates the imposed flux and causes an rf screening current to flow. The amplitude of this screening current is greater than I_c. The energy dissipated when the screening current reaches I_c, is recovered from the rf tank circuit. When an appropriate rf current has been established, the instantaneous rf signal amplitude appearing across the tuned circuit is modulated by any additional magnetic flux Φ_{mod} coupled into the SQUID sensor. (This additional flux determines the rf current level at which I_c is reached). The response is perfectly periodic with a period equal to the flux quantum, h/2e (where h is Planck's constant and e is the electronic

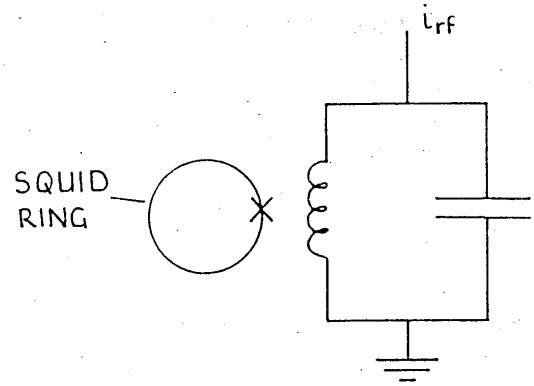

Figure 1 Schematic of rf SQUID resonant circuit

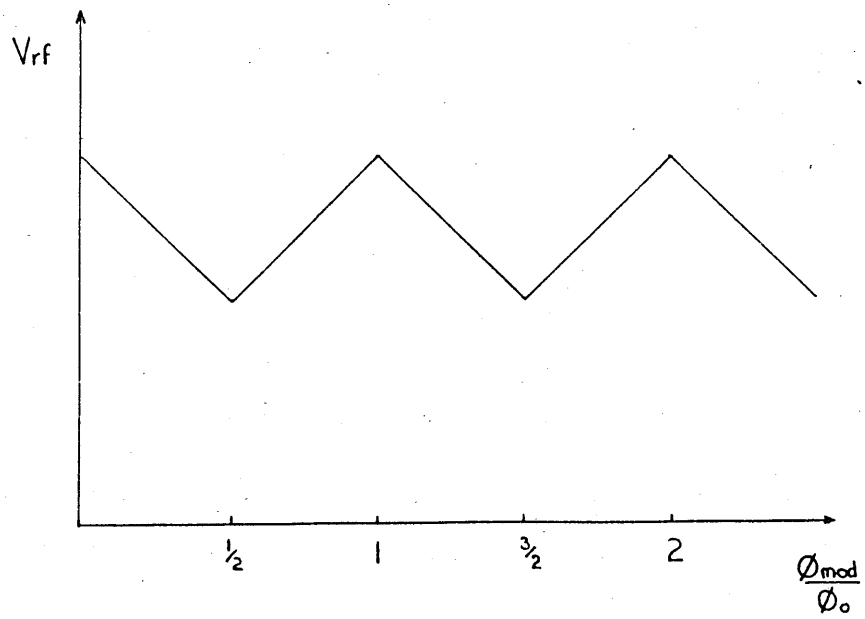

Figure 2 Periodic transfer function showing the variation in rf voltage with increasing modulation flux at a fixed rf bias current

charge). This periodic transfer function is shown in Figure 2. The effect of any further external flux coupled in to the SQUID is to produce a corresponding shift of the transfer function along the flux axis.The small signal transfer function is then just the slope of the triangle side.However, in practise, a negative feedback circuit locks the total flux at one of the extrema of the transfer function,the external flux change being proportional to the feedback current (monitored as a voltage across the feedback resistor).

SQUIDS can be used to sense a magnetic field directly (Zimmerman 1983), but for most biomagnetic studies, this is not the most practical arrangement. The principle reason is simply the need to minimize, in most systems, the sensitivity of the SQUID to ambient noise. Instead, a flux transformer is used to couple the SQUID to the field to be sensed. This transformer is a closed superconducting circuit usually fabricated from niobium wire. It has a primary detection coil or coil set (of inductance L_d) and a secondary input coil (of inductance L_i) as shown in Figure 3. There is an additional inductance (L_e) associated with the leads.

When a magnetic flux Φ_{app} is applied to the detection coil a current I_i circulates around the transformer to maintain the total flux through the transformer circuit constant. The current is given by the flux conservation equation

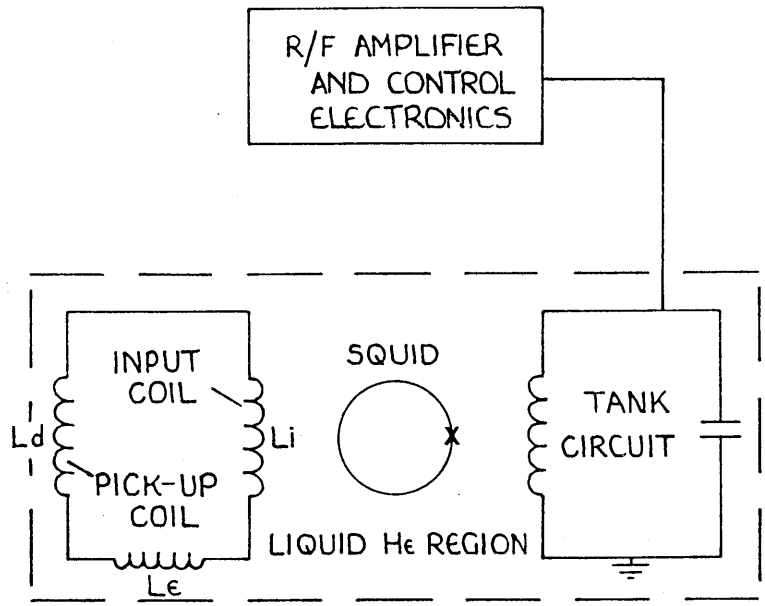

Figure 3 The input circuit of an rf SQUID consisting of a pick up coil connected in a superconducting circuit to an input coil inductively coupled to the SQUID

$$I_i = \frac{\Phi_{app}}{(L_d + L_i + L_e)} \qquad (4)$$

Thus the flux Φ_s ($= M_i I_i$ where M_i is the mutual inductance between the input coil and the SQUID) which the flux transformer secondary applies to the SQUID is proportional to Φ_{app}. The useful sensitivity of any SQUID is limited by the efficiency with which the signal Φ_{app} can be coupled to it. For maximum sensitivity, a large mutual inductance between the secondary and the SQUID is required.

At the other end of the flux transformer, another important parameter, when considering sensitivity, is the size of the pick up coil. A large diameter coil will have a large amount of flux threading it and will be more sensitive to field changes but it will have a poor spatial resolution. In addition it will have a large self inductance. In practice the optimum compromise is reached when the inductances of the pick-up coil and the input coil to the SQUID (the secondary) are matched (i.e $L_i = L_d$).

When the sensitivity problem has been overcome, the second problem, of overcoming interference from the background fields, is solved by a variety of means. Reducing the background field (by $\simeq 10^3$) within the experimental region

by using Helmholtz coils eliminates signals from local para and diamagnetic material. Uniform noise fields are discriminated against by employing a gradiometer arrangement for the input circuit. The second order axial gradiometer used for the work described, consists of a set of three coils with the same diameter, the lowest of which is the pick up coil. The lowest and upper-most coils are wound in one direction while the middle coil, with twice as many turns, is wound in the counter direction. A uniform field or field gradient threading all three coils will have zero total flux linkage. It is intrinsically difficult to construct mechanically perfect gradiometers. A balance of 1 part in 10^3 is achievable with good construction but this can be improved to about 1 part in 10^6 by utilizing appropriately positioned pieces of superconductor in close proximity to the coils.

An alternative method of reducing external noise is to use a magnetically shielded chamber. This solution is costly and can be claustrophobic for the subject.

Thus far, only the possible causes of signals from biological sources and the detection of fields by SQUID magnetometers have been discussed. In the next section the relationship between source current densities and their associated magnetic fields will be explored.

1.4 Electromagnetic Theory

In this section, the calculation of the field produced by a current distribution will be discussed. The analysis presented is based on the work of several authors (Geselowitz 1970, Cuffin and Cohen 1977 and Sarvas 1987). Only the main steps in the argument are presented. Starting with the general expression for the magnetic field produced by a region of arbitrary current density, expressions are developed for fields produced by current dipoles within simple bound geometries.

A region of space in which there is current density $\mathbf{J}(\mathbf{r}')$ will give rise to a magnetic field. The magnetic induction $\mathbf{B}(\mathbf{r})$ outside the region is given by

$$\mathbf{B}(\mathbf{r}) = \frac{\mu_0}{4\pi} \int_{v'} \mathbf{J}(\mathbf{r}') \times \frac{\mathbf{R}}{R^3} \, dv' \qquad (5)$$

where $\mathbf{r}'$ is the vector from the origin of the coordinate system to the source point and $\mathbf{R}$ is as defined in Figure 4. The integral is over all volume elements.

The total current density can be divided into an impressed and a volume current density, where the impressed current is that produced by some energy source (active tissue in a biological context), and the volume current is the term given to the currents set up by the electric fields.

$$\mathbf{J}(\mathbf{r}') = \mathbf{J}^i(\mathbf{r}') + \mathbf{J}^v(\mathbf{r}') \qquad (6)$$

The volume term is related to the conductivity σ and the electric field $\mathbf{E}$ so that

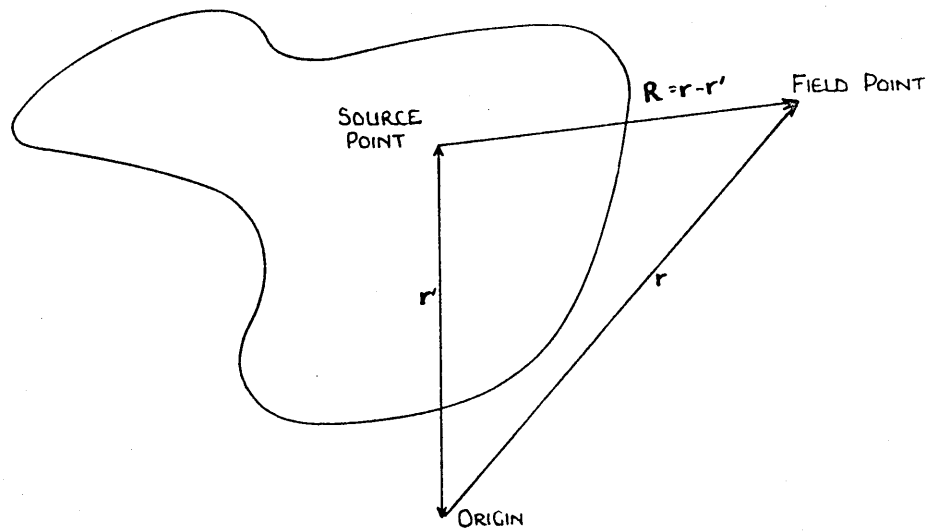

Figure 4 A region of space with current density J(r') where r' is the vector from the origin of the coordinate system to the source point. R is defined as r - r'

$$\mathbf{J}(\mathbf{r}') = \mathbf{J}^i(\mathbf{r}') + \sigma(\mathbf{r}')\mathbf{E}(\mathbf{r}') \tag{7}$$

where $\mathbf{E}(\mathbf{r}') = -\nabla V(\mathbf{r}')$, V being the electric potential. Now equation 5 can be rewritten as

$$\mathbf{B}(\mathbf{r}) = \frac{\mu_0}{4\pi}\int_{V'}\left[\mathbf{J}^i(\mathbf{r}') \times \frac{\mathbf{R}}{R^3} - \sigma(\mathbf{r}')\nabla V(\mathbf{r}') \times \frac{\mathbf{R}}{R^3}\right]dv' \tag{8}$$

for an arbitrary conducting volume.

To find **B** for an arbitrary distribution $\mathbf{J}(\mathbf{r}')$ it is convenient to consider the volume to be made of N sub volumes. The conductivity of each subvolume is assumed to be homogeneous and the contribution from each can be summed to obtain the total field.

$$\mathbf{B}(\mathbf{r}) = \frac{\mu_0}{4\pi}\int_{v'}\mathbf{J}^i(\mathbf{r}') \times \frac{\mathbf{R}}{R^3}\,dv' - \sum_{n=1}^{N}\int_{v'}\sigma_n\nabla V(\mathbf{r}') \times \frac{\mathbf{R}}{R^3}dv' \tag{9}$$

We further assume the impressed current density to consist of M current dipoles (source sink pairs separated by infinitesimal current elements), such that

$$\int \mathbf{J}^i(\mathbf{r}') \times \frac{\mathbf{R}}{R^3}\,dv' = \sum_{j=1}^{M}\mathbf{P}_j \times \frac{\mathbf{R}_j}{R^3_j}$$

If we now use the vector identity $\nabla \times \left[V\,\frac{\mathbf{R}}{R^3}\right] = \nabla V \times \frac{\mathbf{R}}{R^3}$

and apply Stoke's theorem, equation 9 can be rewritten as

$$\mathbf{B}(\mathbf{r}) = \frac{\mu_0}{4\pi}\left[\sum_j \mathbf{P}_j \times \frac{\mathbf{R}}{R^3} - \sum_n \int_s \sigma_n V(\mathbf{r}')d\mathbf{S} \times \frac{\mathbf{R}}{R^3}\right] \tag{10}$$

where $d\mathbf{S}$ is a surface element of the n^{th} sub volume.

The surface integral in equation 10 is taken over the surfaces of all sub volumes. Each surface element will make a contribution from the sub volume on each side. These may have differing conductivities. If we define σ' to be the inner conductivity and σ'' to be the outer, a general formula for the external field $\mathbf{B}$ for a set of current dipoles $\mathbf{P}_j$ in a piecewise homogeneous conducting body can be written

$$\mathbf{B}(\mathbf{r}) = \frac{\mu_0}{4\pi} \sum_j \mathbf{P}_j \times \frac{\mathbf{R}}{R^3} - \left[\frac{\mu_0}{4\pi} \sum_n (\sigma' - \sigma'') \int_s V(\mathbf{r}')d\mathbf{S} \times \frac{\mathbf{R}}{R^3} \right] \quad (1.1)$$

This result shows how the volume currents $-\sigma\nabla V$ affect $\mathbf{B}$. In equation 1.1 the terms $V d\mathbf{S}$ and $\mathbf{P}_j$ have the same role, and it follows that the volume current contribution has the form given by a distribution of surface current dipoles orientated perpendicular to the local surface with magnitude proportional to the potential V.

Similar forms of this general equation have been quoted by other authors notably Geselowitz who showed that the field is given by

$$\mathbf{B} = \frac{\mu_0}{4\pi} \int \mathbf{J}^i \times \nabla \frac{1}{R} \, dv' + \frac{\mu_0}{4\pi} \cdot \sum_n \int (\sigma' - \sigma'') \, V \nabla \frac{1}{R} \times d\mathbf{S}_n \quad (1.2)$$

when the identity $\frac{\mathbf{R}}{R^3} = -\nabla \frac{1}{R}$ is used. This form is also used by Cuffin and Cohen (1977) amongst others. Sarvas (1987) chooses to retain the vectors $\mathbf{r}$ and $\mathbf{r}'$ rather than using $\mathbf{R}$.

In general, evaluation of **B** from equation 11 or 12 is complex. However, in special cases of high symmetry, such as a spherically symmetric, cylindrically symmetric or horizontally layered conductor, **B** is simpler to compute. If a dipole is located on and orientated along the axis of a volume conductor having axial cylindrical symmetry, then **B** = 0 everywhere outside the conductor (Cohen and Hosaka 1975). Two examples of special symmetry are considered below.

Infinite Half Space

A current dipole that is parallel to the surface of an infinite half-space produces an external field but the field component perpendicular to the surface has no contribution from the volume current term (Cuffin and Cohen 1977), which only generates fields perpendicular to the surface vectors **dS**.

For such a tangential dipole **P** pointing in the y direction and located at (0,0,-d) beneath the surface occupying the plane z = 0, the z component of field is given by

$$B_z = \frac{-\mu_0 P_y}{4\pi} \cdot \frac{x}{(d^2+x^2+y^2)^{3/2}} \qquad (13)$$

The lines of constant field magnitude in a plane parallel to the surface show a pattern of two sets of "circles", one for field going into ($B_z < 0$) and the other for field out of ($B_z > 0$) the surface. The separation Δ of the extrema is related solely to the depth of the source

beneath the measurement plane, i.e

$$\Delta = 2^{1/2}d \tag{14}$$

The field magnitude at each extremum is

$$B_{max} = 0.385 \frac{\mu_0 P}{4\pi d^2} \tag{15}$$

Homogeneously Conducting Sphere

Since a radially orientated dipole in a homogeneously conducting sphere is an example of a cylindrically symmetric system it produces no external field, and only a tangential dipole need be considered. Without loss of generality the tangential dipole may be assumed to be pointing in the positive x direction and located at $r = a$, $\theta = 0°$ and $\varphi = 0°$ as shown in Figure 5.

The radial component of magnetic field from this dipole can be calculated from equation 11. The radial component of field is given by

$$B_r = \mathbf{B} \cdot \hat{\mathbf{r}}$$

$$= \frac{\mu_0}{4\pi} \frac{\mathbf{P} \times \mathbf{R}}{R^3} \cdot \hat{\mathbf{r}} - \frac{\mu_0}{4\pi} \left[\sum_n (\sigma' - \sigma'') \int_s V(\mathbf{r}') d\mathbf{S} \times \frac{\mathbf{R}}{R^3} \cdot \hat{\mathbf{r}} \right] \tag{16}$$

In the second term

$$(d\mathbf{S} \times \mathbf{R}) \cdot \hat{\mathbf{r}} = (d\mathbf{S} \times (\mathbf{r} - \mathbf{r}')) \cdot \hat{\mathbf{r}}$$

$$= -(d\mathbf{S} \times \mathbf{r}') \cdot \mathbf{r}$$

$$= 0 \qquad \text{(as } d\mathbf{S} \text{ is parallel to } \mathbf{r}')$$

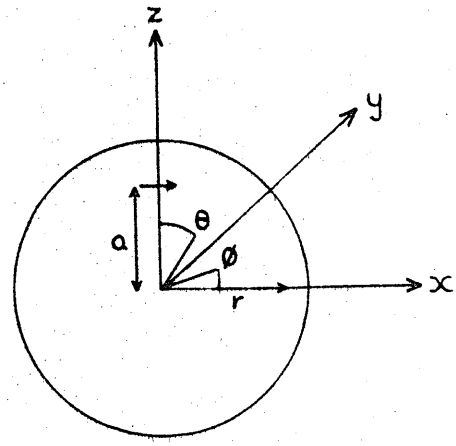

Figure 5 Coordinate system for the current dipole in a homogeneously conducting sphere. The dipole is pointing in the positive x direction and is located at spherical polar coordinates r = a, θ = 0° and φ = 0°

It follows that B_r depends only on the source dipole and does not depend on the volume currents:

$$B_r = \frac{\mu_0}{4\pi} \frac{(\mathbf{P} \times (\mathbf{r} - \mathbf{a})) \cdot \hat{\mathbf{r}}}{R^3} \tag{17}$$

$$= -\frac{\mu_0}{4\pi} \frac{(\mathbf{P} \times \mathbf{a}) \cdot \hat{\mathbf{r}}}{R^3}$$

$$= \frac{\mu_0}{4\pi} \frac{P_x a \hat{\mathbf{y}} \cdot \hat{\mathbf{r}}}{R^3} \qquad \text{(where } \mathbf{P} = P_x \hat{\mathbf{x}}\text{)}$$

But $y = r \sin\theta \sin\varphi$

therefore

$$B_r = \frac{\mu_0 a P_x \sin\theta \sin\varphi}{4\pi r^3 \gamma^{3/2}} \tag{18}$$

$$\text{where } \gamma = 1 - \frac{2a \cos\theta}{r} + \left[\frac{a}{r}\right]^2$$

Equation 18 represents the radial component of the field from a dipole in a sphere. Similarily the φ and θ components can be derived by a method involving a Legendre series expansion of the vector potential. The method is somewhat complex and only the results are shown here (Cuffin and Cohen 1977).

$$B_\theta = \frac{\mu_0 a \sin\varphi P_x}{4\pi r^3 \gamma^{3/2}} \left[\frac{\gamma \cos\theta}{\sin^2\theta} \left[\cos\theta - \frac{r}{a} + \frac{r\gamma^{1/2}}{a}\right] - \left[\frac{a}{r}\left[\cos\theta - \frac{a}{r}\right]\right]\right] \tag{19}$$

$$B_\varphi = \frac{\mu_0 \cos\varphi P_x}{4\pi r^2 \gamma^{1/2} \sin^2\theta} \left[\frac{r}{a} - \cos\theta - \frac{r\gamma^{1/2}}{a}\right] \tag{20}$$

These equations can be used to calculate the field from a given dipole located in a conducting sphere. Calculating the field from equivalent dipoles (or sources) is known as the forward problem. In biomagnetism, the fields can be

detected but the underlying sources need to be determined. In the next section the basic assumptions necessary for determining the sources are discussed.

1.5 Analysing The Field Data - General Remarks

Determining the relationship between the surface or extra organism electromagnetic fields and the underlying sources is one of the greatest challenges in electrophysiology. This process of going from the surface effect to the underlying sources is known as the inverse problem. Solutions to the general biomagnetic inverse problem are non-unique. There are in effect an infinite number of different source distributions whose surface fields are identical. This is easily seen for certain geometries from the existence of magnetically silent source distributions; e.g. any radial current dipole in a sphere. Only when the problem is reduced to a given parametric model can a unique solution be obtained. Of course, an arbitrarily complex parametric source distribution cannot be determined from a finite number of surface measurements. In general, it is desirable to estimate a small number of parameters from a large number of surface measurements to optimise the inverse calculation, even though the simple model utilized may have a limited functional relationship with the system or process under study.

Simple models such as a single current dipole within a volume conductor of simple geometry are often used to describe the system (Williamson and Kaufman 1981). The source of the cardiac field, the source of steady fields associated with the eye and the source of the neural fields of the brain evoked by sensory stimuli have all

been modelled by a single dipole model.

For the heart, it is usual to model by a dipole in a half space where the field normal to the surface is due solely to the current dipole and there is no contribution from volume currents (Cohen and Hosaka 1975). In the case of neural sources from the head, the first and crudest models would be a single dipole in a conducting half space for a source near the surface and a dipole in a conducting sphere model for deeper sources. Here too, as previously noted, the component of the field lying normal to the surface arises only from the current dipole. This remains true if the electrical conductivity of the sphere varies with radius but has concentric symmetry (Okada 1985). Some improvement in the sphere model could be achieved by taking into consideration the local curvature of the head at the appropriate region when defining the centre and the radius of the model sphere. A more sophisticated model would take into consideration the intricate shape and conductivity of the local conducting volume and the postulated source would be needed. The quality of the data, however, needs to justify the type of model used for the analysis and hence accuracy quoted for the signal source.

When modelling real data, a further complication arises from the nature of the signal. A SQUID system provides an output signal that is proportional, not to the field at a point but, to the **total magnetic flux** which threads its

detection coil set. For a magnetometer, or a gradiometer having a sufficiently long baseline (the distance between the pick up loop and the middle cancellation loop), this is approximately the flux which passes through the lowest coil. If the diameter of the pick up coil is of comparable size to the distance separating the two extrema of the detected field, significant smearing of the field occurs. Now, for example, if the half space model is assumed without allowing for this smearing, the measured separation will predict a much greater depth and magnitude than a pick up coil with a much smaller diameter.

Another practical difficulty in analysing magnetic field data from neural sources, is the assumption of stationarity (constancy of the response to a defined stimulus over time). With a limited number of input channels, data acquisition can be a lengthy process during which the subject undergoes physiological or psychological changes (Nunez 1986). Stationarity has to be checked rather than assumed through the course of the experiment.

Once these difficulties have been overcome, an equivalent dipole, or dipoles, can be found by matching the predicted field data with detected field data through convergent iterative forward calculation. These dipoles have to be physiologically reasonable (i.e take account of neurological and anatomical observations). If ionic flow is predicted by a model, can it be verified by using other

techniques such as electric potential measurements at the surface of the scalp? The major question (and the starting point for this thesis) is whether the model used for the forward calculation is adequate or even appropriate.

1.6 An Overview Of The Thesis

Thus far only a brief introduction to relevent aspects of experimental biomagnetism has been presented. In the next chapter the instrumentation used for biomagnetic studies in our laboratory will be discussed, in general terms. Each experiment had its own minor variations that are described in later chapters. The next chapter includes sections on data acquisition and details of the analysis used for the forward calculations essential for the iterative method of solving the inverse problem.

The first experimental results are presented in chapter 3. It starts with a review of recent and concurrent work on the dipole in a sphere model and its application to biomagnetism. The use of a dipole in a sphere model is evaluated empirically with successive physical models of sphere-like systems. The problem of dealing with more than one dipole is touched on briefly before a general discussion concludes the sphere chapter.

Spheres are replaced by the (geometrically complex) skull in chapter 4. Effects of different dipole location within the skull and the relative ease of applying the dipole in a sphere model for analysing the results are explored. Examples of the effects of different internal skull geometries on the detected field pattern and the accuracy of dipole characterization are presented rather than a complete catalogue.

The second half of the thesis is concerned with applying the lessons of the first half to real biological systems. Magnetic fields emanating from a developing chick egg change during development but are constant over short (e.g 1 hour) times. At first sight the chick egg provides an easily accessible system for assessing the appropriateness of the dipole in a sphere model in determining the source generators. As the sources were not known, predictions of the model had to be tested using other techniques. The chick egg study is described in chapter 5.

Chapter 6 then describes experiments exploring the retinotopic representation of the visual fields on the cerebral cortex. Magnetic field and electric potential evoked responses to a reversing checkerboard pattern were recorded. Source generators were postulated using the dipole in a sphere analysis. Some differences between the electric and magnetic reponses, not previously reported, were noted.

The final chapter contains concluding remarks concerning the dipole in a sphere model and its applicability in analysing biomagnetic data as well as suggestions for further work on this topic.

Instrumentation And Analysis

In this section the instrumentation and analysis common to most aspects of the work presented will be briefly outlined. There are two distinct types of experiment, one where the subject is stationary during data acquisition and the other where the subject is scanned beneath the detector. In this section the latter more complicated experiment will be concentrated upon. The section may be subdivided into three parts.

1 Instrumentation related to signal detection (i.e the magnetometer)
2 Instrumentation related to the source itself (i.e the mounting platform)
3 Instrumentation related to data acquisition and analysis.

2.1 Signal Detection

The magnetometer consists of a commercial second order gradiometer (Swithenby 1980) inductively coupled to an rf SQUID. The gradiometer is formed from eight turns of niobium wire wound onto a 23.5 mm diameter quartz former. Two turns at the bottom of the gradiometer form the pick up coil and are wound in the same sense as the two turn top coil (with a 64mm separation between the two sets of coils). The four turns forming the centre coil are wound in a counter direction. Since the gradiometer coils have a

common vertical axis, the magnetometer is sensitive to the z component of the magnetic field at the gradiometer. Being second order, the gradiometer discriminates against uniform fields and against uniform field gradients. This enhances the signal to noise ratio.

In series with the gradiometer is an input coil which inductively couples the detected flux to a toriodal hybrid SQUID (TSQ) loop. Also coupled to the SQUID loop is an rf tank circuit oscillating at 19MHz, a part of the SQUID electronic system. The system has an overall intrinsic field sensitivity of $\approx 3 \times 10^{-14} T/Hz^{1/2}$ (related to average field over the lowest coil). The actual noise spectrum (Figure 6) shows the greatest noise contribution at the lowest frequencies. This is mainly due to the low frequency ambient fields in and around the laboratory. The response of the SQUID system is wideband (0-10kHz); much of the noise can be rejected by operating with a low pass filter (e.g with a 100 Hz cut off frequency) and a line frequency notch filter.

The gradiometer, SQUID loop and the rf feedback tank circuit make up the biomagnetic probe assembly (SHE Corp 1980). This entire assembly is housed in a 6 litre capacity glass fibre dewar. Insulation between the 4K and the 300K environments is provided by a vacuum of better than $\approx 10^{-6}$ torr together with aluminized mylar radiation

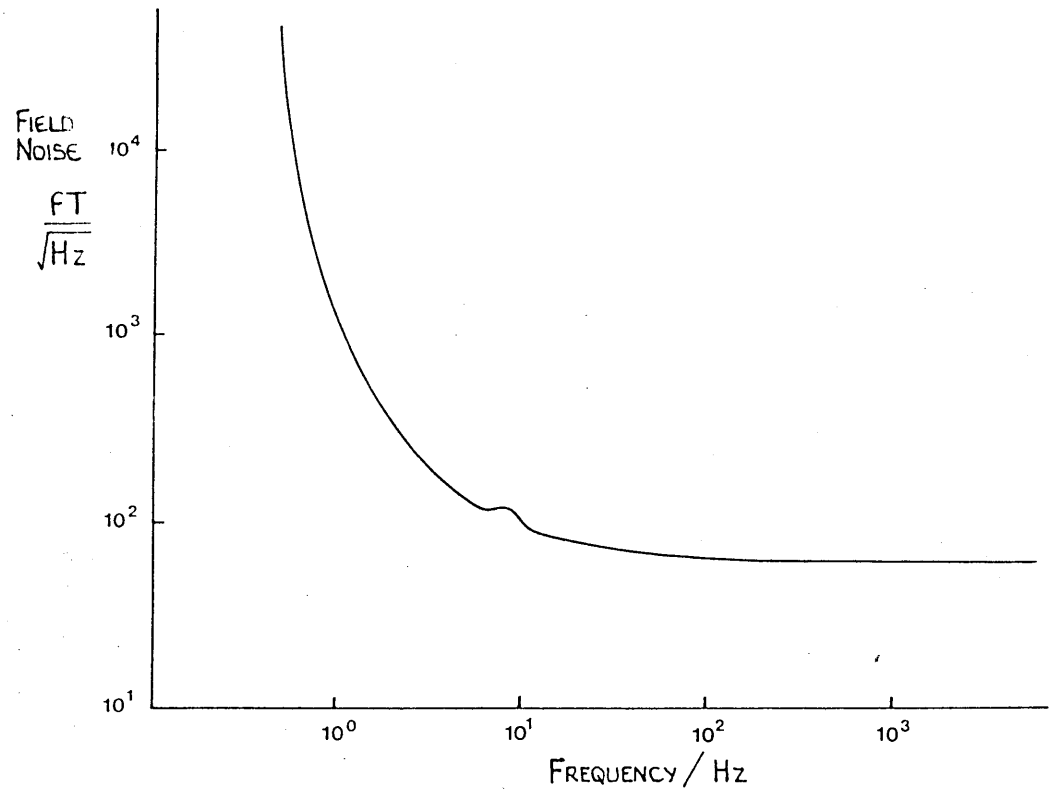

Figure 6 Smoothed noise spectrum for our SQUID magnetometer with a 50 Hz notch filter. The increase in noise at the low frequency end necessitates movement of the subject when recording pseudo- d.c fields.

shields between the inner and outer chambers of the dewar. This insulation serves to eliminate the necessity for liquid nitrogen cooling. It is important to minimize the distance between the gradiometer and the source outside the dewar because the field strength becomes rapidly weaker with increasing distance. The present system has a gap such that the coil-300K distance is 11mm when the dewar is warm and 12mm when it is cold. The difference is due to thermal contraction of the inner chamber.

Only the biomagnetic probe is maintained at 4K and, apart from the rf tank circuit, all circuitry for supplying power or feedback is maintained at 300K. An rf headbox is mounted on top of the dewar and remote from the dewar is a SQUID control box. The control box houses a set of filters and various oscillators as well as gain controls for the SQUID electronics.

Without further equipment the simple magnetometer can be used to detect changes in magnetic flux. Time varying signals (e.g activity from the brain) can be detected by placing the detector in close proximity to the source. For mapping a complete region, the detector is sequentially moved to a new position. It is important to know the position of the detector relative to the source volume if source localization is to be attempted.

If the magnetometer remains in a fixed position relative

to the source, it would not be sensitive to the dc and pseudo-dc fields that are of interest to us. Detecting these fields is the subject of the next section.

2.2 Detecting Steady Fields

The SQUID magnetometer responds to changes in flux and in a fixed position is not sensitive to dc and pseudo-dc fields that are of interest. This problem is overcome by moving the signal source relative to the detector to create a varying field.

With the present system, the detector remains stationary in the x and y directions, but between measurements it can be moved to positions varying by up to 20cm in the z direction. In experiments involving steady fields, the signal source is made to move in the xy plane on a travelling platform onto which it is securely placed. The position of the platform itself is monitored by computer in the form of voltage changes across potentiometers. The two potentiometer shafts are mechanically linked to the platform. For y-direction movement, the link is direct; for the x-direction it is via a nylon gear wheel and a toothed drive belt system (Figure 7). Movement of the platform itself causes resistance changes in each potentiometer to which a constant current is supplied resulting in a voltage change.

In the usual procedure, the platform is driven a fixed distance of 60 cm, (limited by the size of the Helmholtz coils to be described later), in the x direction by a powerful electric motor coupled to the platform by an aluminium shaft and nylon parachute cord which passes over

Figure 7 Moving platform system for making 'dc' magnetic field measurements. x and y direction potentiometers determine exact position of the platform. The SQUID dewar can be moved in the Z direction

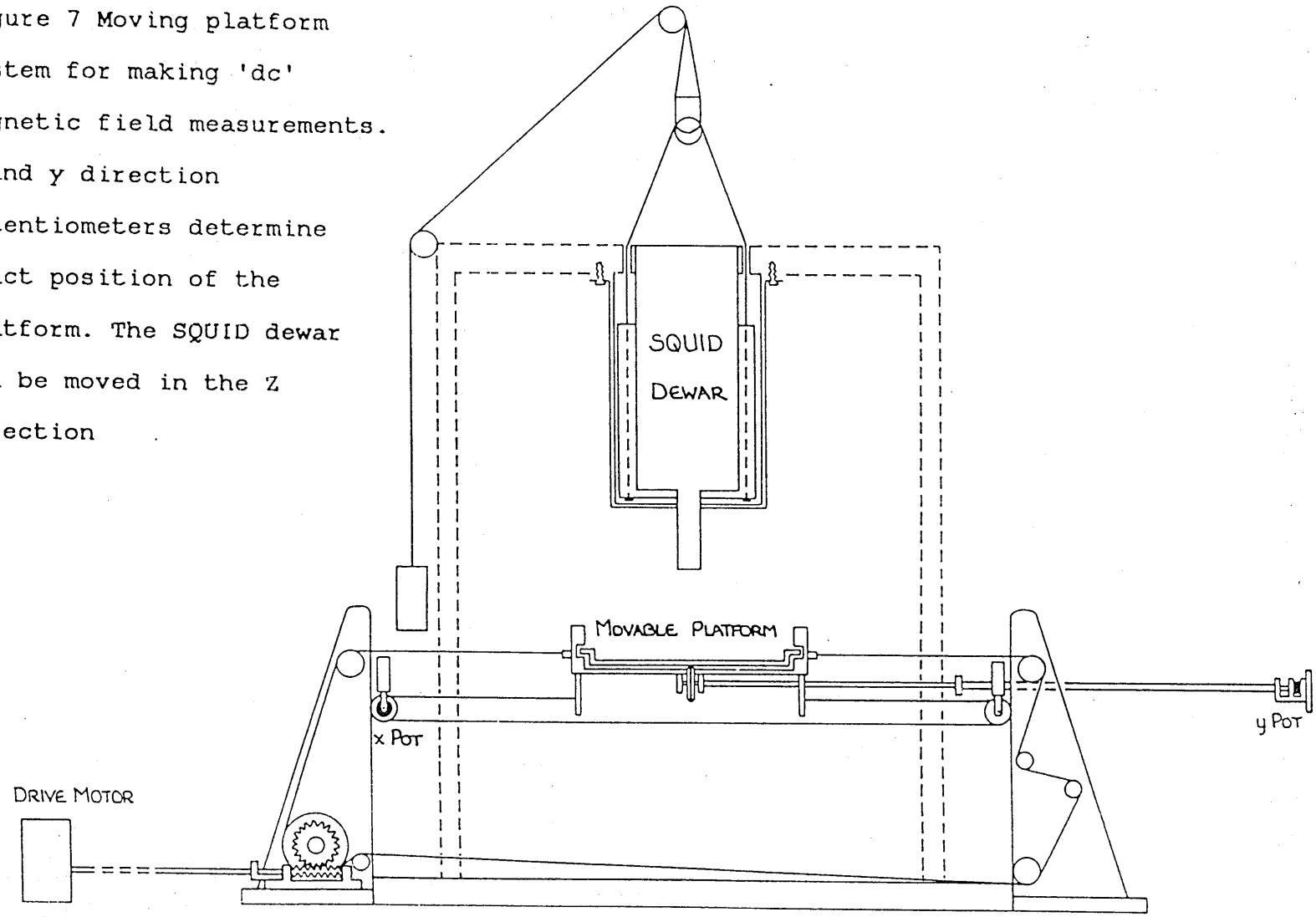

a series of pulleys. A worm drive gearing system is used to reduce the effective speed of platform travel. Contact switches prevent the motor from running on after the end of platform travel has been reached. The motor itself is placed 3 m from the SQUID (hence the aluminium coupling rod) and is shielded to reduce electromagnetic interference.

The SQUID voltage output shows the change in magnetic flux through the detector coils as the subject is moved. To a first approximation it records B_z along a horizontal line.

A problem arises if the measurements are made in the presence of an external magnetic field, since the magnetic susceptibility of the object will contribute to the change in magnetic flux, and the voltage output will reflect the magnetic susceptibility of the object as well as any currents within it. Biological media are made up on average of 60% water, which has a susceptibility of $9 \times 10^{-6}.m^{-3}$; the susceptibility related signal is typically larger than the possible magnetic fields emanating from the organism as a result of current flow.

By nulling the ambient field, the susceptibility effect can be reduced to negligible proportions. This is achieved by employing two sets of 1.8 m diameter Helmholtz coils formed from 18 swg copper wire (1.22 mm diameter) and orientated north-south and vertically. A central region of

0.6 m diameter can be maintained with a field of magnitude less than $4x10^{-7}$ T using a current of ≈0.58 A through the horizontally orientated 80 turn coils to null out the vertical component of the field and ≈0.75 A current through the vertically orientated set to null out the north-south field component. For nulling of the east-west field component, 14 turns of 34 swg wire (0.5 mm diameter) in the form of square coils are used. There is no component of the earth's field in this direction but this set was necessary to null magnetic fields from ferromagnetic materials in the surrounding laboratory and corridor.

The ambient field varies typically by 1% in 24 hours, a result of fluctuations in the Earth's field and movement of metal furniture or laboratory equipment. The field around the SQUID dewar is checked intermittently using a Thorn racetrack type fluxgate magnetometer (FG 413) and the current through the Helmholtz coils adjusted to maintain the field at less than $\approx 4x10^{-7}$ T. This was especially important for the chick experiments.

The mechanics of how a signal is detected by our second order gradiometer and how susceptibility effects are reduced have been described. The next section describes how the signal is recorded and processed.

2.3 Data Acquisition and Analysis

The data acquisition is by a dedicated PDP11-23 MINC II mini-computer system (Digital Corp 1978). During any experiment involving movement of the platform, the SQUID output and the outputs of the x and y potentiometers are all continuously sampled by a 12 bit ADC and spatially averaged. For a given x direction increment, for example 5mm, the ADC will continously sample the SQUID output voltage at ≈900 Hz and average over the total number of samples within the spatial increment.

It is important to calibrate the potentiometers to indicate sample position over the entire travel range at the start of each experiment. This is achieved by recording the potentiometer output values at the limits of platform travel in the x-y plane. These remain fixed and define a laboratory x-y coordinate system. Positions within that system can be found by moving the subject on the platform to a position fixed relative to the detector by marker values manually input into the computer.

In the usual protocol, the platform was moved over the full length of travel in the x direction at fixed y. Any number of traverses of the platform (usually 3 to 5) may be averaged in order to improve the signal to noise ratio. Data can be accepted or rejected for each traverse and extraneous artefacts, e.g from moving cars or closing doors, can be removed before averaging. The final signal

is then plotted out onto paper and stored on magnetic disk for subsequent analysis. The entire process is then repeated at a new y position.

A series of data files, each corresponding to a scan at a different y value, are required before a full field mapping can be achieved. Usually the files are used to form contour maps before any analysis. This can be carried out either by the MINC II computer or, more frequently, the data is transferred to the Open University mainframe computer (DEC 20 Digital Corp). Contouring is carried out by employing appropriate routines from the SIMPLEPLOT library (J.Butland 1982).

The analysis usually entails iterative fitting of the dipole in a sphere model to the data. Accuracy of fit is signalled by the minimization routine E04FDF (Nag library). The rest of this section goes on to describe the dipole in a sphere analysis routines.

Analysis Program

The analysis entailed iterative fitting of the data calculated using the forward solution of the dipole in a sphere model to the experimental data. The equations presented earlier for B_r, B_θ and B_Φ give the radial and tangential components of the field. In our experiments we are sensitive to all three components, because we scan in the plane of the detector pick up coil rather than tangential to a spherical surface as shown in Figure 8.

Utilizing the standard coordinate transforms for spherical polar to cartesian coordinates and summing the earlier formulae, an equation can be written for the field perpendicular to the scan plane (Swithenby -personal communication).

$$\frac{10^7\ \gamma^{1/2}\ r^2}{P_x} B_\perp = \frac{a \sin\theta \sin\Phi}{r^2 \gamma\ \rho} \left[x\rho_x + y\rho_y + z\rho_z\right] + \left[\frac{\sin\Phi}{\gamma\rho}\left[\frac{\gamma\cos\theta}{\sin^2\theta}\left[\cos\theta - \frac{r}{a} + \frac{r\gamma^{1/2}}{a}\right] - \frac{a}{r}\left[\cos\Phi - \frac{a}{r}\right]\right]\right.$$
$$\left.\left[\cos\theta\cos\Phi\,\rho_x + \cos\theta\sin\Phi\,\rho_y - \sin\theta\,\rho_z\right]\right]$$
$$+ \left[\frac{\cos\theta}{\sin^2\theta\ \rho}\left[\frac{r}{a} - \cos\theta - \frac{r\gamma^{1/2}}{a}\right]\left[-\sin\Phi\,\rho_x + \cos\Phi\,\rho_y\right]\right] \qquad (21)$$

x, y, z are the coordinates used by Cuffin and Cohen in which the dipole is at (0,0,a) and is oriented along $\hat{x}$. r is the radial distance in this frame and ρ is the perpendicular from the dipole to the scan plane.

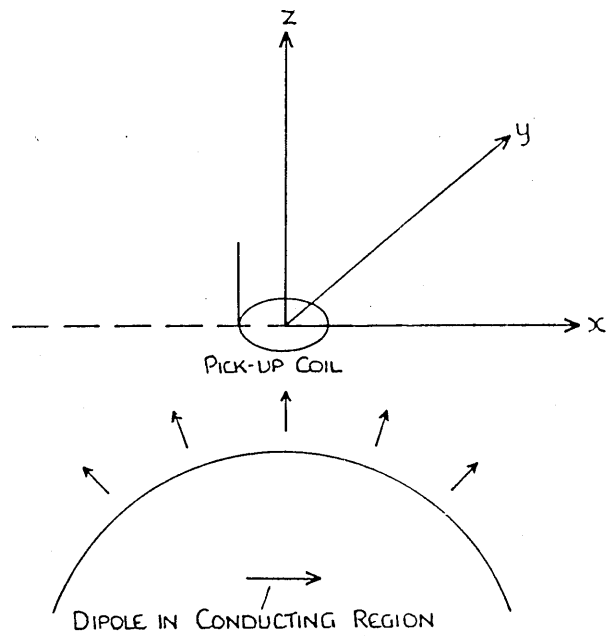

Figure 8 The data acquisition involves scanning the sphere in a plane parallel to the plane of the detector pick up coil rather than scanning the pick up coil tangential to the spherical surface

Our measurements are made in the laboratory frame (X_l, Y_l, Z_l) which we chose such that the sphere centre (at the origin in the x, y, z frame) is at (0,0,-h). The dipole is at (X_D,Y_D,Z_D) where $Z_D = -\rho$. In order to use equation 21, a set of transform equations between these frames is required.

These can be found via an intermediate frame (X, Y, Z) defined with $\hat{Z} = \hat{Z}_l$, and with its origin at (X_D, Y_D, 0) in the laboratory frame. The $\hat{X}$ axis is chosen to lie on the projection of the dipole into the XY plane. The relationship between the Cuffin and Cohen frame and the intermediate frame is algebraically defined by

$$\hat{X} \times \rho = \text{constant} \times \hat{Y}$$

$$X \cdot Y = 0$$

$$\hat{X} \times \hat{Y} = \hat{Z} = \hat{\rho}$$

By simple manipulation we find

$$x = \frac{c}{\rho} X + \frac{\rho_x}{\rho} Z + \rho_x \qquad (22)$$

$$y = -\frac{\rho_x \rho_y}{\rho c} X + \frac{\rho_z}{c} Y + \frac{\rho_y}{\rho} Z + \rho_y \qquad (23)$$

$$z = -\frac{\rho_x \rho_z}{\rho c} X - \frac{\rho_y}{c} Y + \frac{\rho_z}{\rho} Z + \rho_z + a \qquad (24)$$

where $c = \left[\rho_x^2 + \rho_y^2\right]^{1/2}$

The X, Y, Z and the X_l, Y_l, Z_l frames are superimposed by

a translation and a rotation by α about the $\hat{Z}_1$ axis. The final transform equations are

$$x = \frac{c}{\rho}\cos\alpha\, X_1 + \frac{c}{\rho}\sin\alpha\, Y_1 + \frac{\rho_x}{\rho} Z_1 + \left[-\frac{c}{\rho} F_1 + \rho_x\right] \quad (25)$$

$$y = \left[-\rho_1\cos\alpha - \frac{\rho_z}{c}\sin\alpha\right] X_1 + \left[-\rho_1\sin\alpha + \frac{\rho_z}{c}\cos\alpha\right] Y_1 + \frac{\rho_y}{\rho} Z_1 + \left[-\rho_1 F_1 - \frac{\rho_z}{c} F_2 + \rho_y\right] \quad (26)$$

$$z = \left[-\rho_2\cos\alpha + \frac{\rho_y}{c}\sin\alpha\right] X_1 + \left[-\rho_2\sin\alpha - \frac{\rho_y}{c}\cos\alpha\right] Y_1 + \frac{\rho_z}{\rho} Z_1 + \left[\rho_2 F_1 - \frac{\rho_y}{c} F_2 + \rho_z + a\right] \quad (27)$$

where $\rho_1 = \frac{\rho_x\rho_y}{\rho c}$; $\rho_2 = \frac{\rho_x\rho_z}{\rho c}$

and $F_1 = X_D\cos\alpha + Y_D\sin\alpha$; $F_2 = Y_D\cos\alpha - X_D\sin\alpha$

The components of ρ are given by

$$\rho_x = \frac{\rho F_1}{\left[F_1^2 + (h-\rho)^2\right]^{1/2}} \quad (28)$$

$$\rho_y = \rho(h-\rho)F_2\left[\frac{1}{F^2{}_1 + (h-\rho)^2}\right]^{1/2}\frac{1}{a} \quad (29)$$

$$\rho_z = \rho(h-\rho) / a \quad (30)$$

The above equations fail if $X_D = Y_D = 0$ and $(h-\rho) = 0$, i.e the dipole is at the centre of the sphere.

With these transforms the problem of dipole characterisation becomes one of finding the parameters X_D, Y_D, $\rho = -Z_D$, α and P_x when given the experimental data.

The program compares field values at a number of data points in the scan plane with fields calculated using the forward solution whilst iteratively varying the dipole parameters. The difference between the calculated S_t and experimental S_e data is characterised by a function R defined as

$$R = \frac{\Sigma(S_e^2 - S_t^2)}{\Sigma S_e^2} \qquad (31)$$

where the sums are taken over the set of points.

The NAG library routine E04FDF was utilised within the analysis program to minimise R.

This program was evaluated by generating data with known dipole parameters and then inverting to predict the dipole parameters. Effects of random noise added to the generated data and the use of different starting points for the iterative search of dipole parameters were investigated. The procedure was repeated to determine average errors in the prediction of position, orientation and magnitude.

The effects of noise on the identification of a dipole at (0,0,-3.5cm) with orientation α= 30° and strength P_x= 8E-6Am, are shown in Figure 9. It is clear that noise has a limited effect on the identification of X_D and Y_D but a more serious effect, at higher noise levels, on Z_D. The error in angle α was small (10^0 with a noise to signal ratio of 30%). By far the greatest change between the

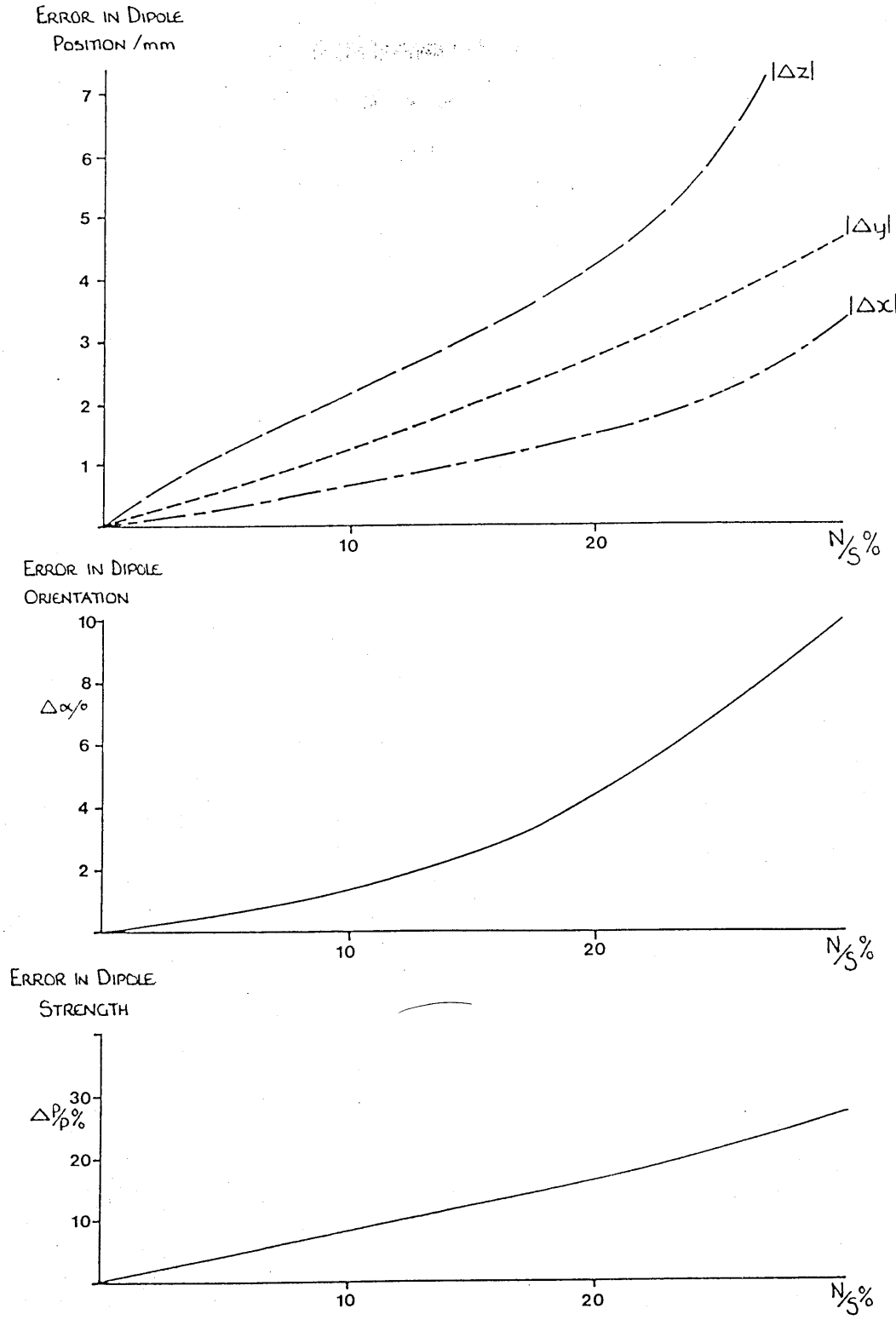

Figure 9 Effects of adding random noise on the predicted dipole parameters using computer generated data. N/S is the ratio ([ave noise^2]$^{0.5}$/[ave signal^2]$^{0.5}$)

generated and predicted parameters was for the dipole moment where $\Delta P/P$ was 25% with a 30% noise to signal ratio. This data can be used to estimate the errors in dipole parameters in later experiments.

Table 2 shows the effect of an incorrect choice of sphere centre to scan plane distance on the predicted dipole parameters (for a dipole at 0.1,0.2,-0.3cm). The choice of model sphere centre does not appear likely to have a significant effect on the accuracy of dipole characterization. It is interesting to note a point that is not evident from Table 2; overestimates of dipole strength and depth are correlated. This difficulty will reoccur in later studies. Finally it is noted that, for all reasonable iteration starting points, the eventual dipole parameter predictions were insignificantly different.

Table 2

Effect of variation in sphere centre to scan plane distance on the predicted dipole parameters.

Data was computer generated with an assumed distance of 8 cm between the scan plane and the sphere centre. The inverse calculation was carried out for the four values of Z_D listed.

Distance Z_D	X_d	Y_d	Z_d	α	P/E-6	R
cm	mm	mm	mm	°	Am	
8	1	2	3	30	1	5E-11
9	0.9	1.92	2.9	31.7	0.9	6E-4
10	0.8	1.82	2.9	32.1	0.8	1E-4
6	1.1	1.94	3.1	25.4	1.1	7E-3

Dipole In A Sphere Model

3.1 Recent And Concurrent Work

The dipole in a sphere model has been applied to many forms of biomagnetic data. It assumes that the source is a simple dipole, that the nonsphericality of the conducting volume does not affect the predicted dipole parameters greatly and also it implies that conductivity inhomogeneities make little difference to the magnetic field distribution. To date the dipole in a sphere model has been most successful in modelling neuronal activity of the brain where the cranial vault is considered to be spherical and the active nerves to constitute a dipolar source. Is the use of this model justified in this or any other case?

It is important to systematically determine the limits and errors expected in the location of current dipoles and other complex sources using superconducting magnetometers. Results of computer simulations and modelling have important implications for these considerations, but the accuracy of location in these studies is determined by the assumptions used in generating the data. For this reason (amongst others) several groups have also attempted to assess the theoretical models empirically by using physical models of dipoles in spherical and skull-like conductors. I will briefly describe both these and relevant computer data studies.

The dipole in a sphere model has been examined most recently by Hansen et al (1987). A dipole with twisted wire leads was suspended in a spherical flask filled with a conducting solution. Several flasks with different radii and dipole positions were used. Exact positioning of the dipole was determined by laser alignment. A radially orientated second order gradiometer was used to scan over Θ with $\Phi = 0^0$. After correcting the detected field values to allow for flux transformer geometry by assigning weighting factors to each loop but without field averaging over the coil area, predicted and measured fields were compared at a number of points. The dipole location was determined by using a least squares fit to the signal variation with θ to identify the angle at which the signal was a maximum and then making a simple calculation of the source depth from knowledge of the angle. An agreement of better than 1 mm was achieved between predicted and measured dipole locations when the signal to noise ratio (SNR) was greater than 10 dB with only 8 points used to cover the whole of the area of interest. Good location accuracy could be achieved with a SNR of greater than 40 dB even when only 4 data points were used. With very few data points, many sets of dipole parameters can be fitted to the data.

This study was of limited value. The scanning method was one dimensional, ie only along Θ. It is not obvious how this method would extrapolate to two dimensions. To date

only ideal systems (perfect spheres and single dipoles) have been reported by this group.

Another group, Weinberg et al (1986) used a gel filled skull with three dipoles located in it as their physical model. Each dipole was 22 mm in length and constructed from aligned ends of a pair of insulated wires forming the top of a 'T'. All the wire tips were capped with 1 mm solder blobs. The three dipoles formed an equilateral triangle at the end of a plastic mount and were positioned 6 mm below the parietal bone with the posterior corner of the triangle located at the skull vertex. Exact locations were confirmed by radiographs.

A third order gradiometer (38 mm sensing coil and 55 mm intercoil separation) was used to detect the magnetic field normal to the skull. This data was fitted to a dipole in a homogeneous sphere model. The radius chosen for the model sphere used in the calculation was the mean of the radii at the 25 measurement points with respect to a common origin at the 'cranial centre'. Two methods of source location, via peak field location and a least squares iterative fit to the entire data set, but not including the peak field values, were used with the latter yielding better results. The mean (3 dimensional) location acuracy for the three dipoles was 3.5 mm. These dipoles were very superficial (6 mm below the parietal bone). However, these workers failed to resolve multiple dipoles

(where two of the dipoles were simultaneously activated) probably due, partly at least, to the large size of the pick up coil. The analysis did not take coil size, geometry, or the orientation of the dewar with respect to the skull into consideration. It is also worth noting that their use of external skull dimensions to define the model sphere ignored the difference between the external and the more relevant internal skull curvatures.

Barth et al (1987) used both perfect spheres and skulls as physical models. Their dipole was placed at four different depths and at random orientations, within the sphere. In their calculations, they allowed for the existence of several coils in their gradiometer but not for the variation of the field over each coil (i.e did not field average).

The first part of the study, which involved dipoles in perfect spheres, was analysed using the dipole in a conducting sphere model and resulted in the mean error between the predicted and actual dipole locations of 1.5 mm.

Results were not so favourable for the skull experiments, where the dipoles were placed in the left temporal region at five depths and the gradiometer axis was orientated perpendicular to the skull at the measurement sites. The magnetic fields from the skull-dipole system did not

appear to have simple dipolar forms, ie they were distorted from a simple concentric pattern. (The authors suggested that self cancellation of secondary sources may not be complete in the cranium because the insulating boundary is not spherical.) Analysis was again based on a best least squares fit of the field to the dipole in a sphere model with the sphere centre located at a cranial centre defined by measuring the posterior and superior curvatures of the skull. Only enough data points to cover the two field extrema were used. However the data was corrected for the non radial detector orientation (though tangential field components were ignored) and the deviations of the measurement positions from ideal sphere locations, especially over the cheek area. The predicted dipole depths were overestimated for superficial sources and underestimated for deeper sources with a mean error of 9.3 mm in depth. In addition there was an average 5.1 mm error in transverse location. It is interesting to note that by fitting to the gradient of the field rather than the detected field itself, the mean error improved to 3.2 mm and 1.8 mm respectively. The magnitude of the dipole was not considered in the analysis.

This study also considered examples of the effects of inhomogeneities within the conducting region; a craniotomy and an artificial insulating balloon (diameter ≈3cm) placed within the skull (within 1cm of the dipole) had only minor effects on the dipolar patterns. Dipole

locations were affected by no more than 1mm by these gross perturbations. This insensitivity is somewhat surprising but may be linked with the ignoring of tangential field components. The model can be fitted more easily to a small set of data than to a large set.

These examples provide a limited assessment of the usefulness of the dipole in a sphere model. Computer based studies, which will now be described, have provided further insight into the effect of deviations from perfect conducting spherical geometries.

The role of computational experiments in biomagnetic modelling has been recently reviewed by Cuffin (1987). Small symmetrical perturbations from spherical geometry (for example to a prolate spheriod shape), do not affect the magnetic field pattern greatly (Tripp 1977). Formulae for calculating the field from a dipole within an oblate or a prolate spheriod (Cuffin and Cohen 1979) can be generated by perturbation from a starting point of a dipole in a perfect sphere model. These authors found that, for spheroids which were approximately head shaped, the perpendicular field component was produced completely or mostly by the dipole alone. However conductivity inhomogeneities corresponding to pathologically sized lesions in the brain were shown to change the detected field patterns by detectable amounts (Ueno et al 1985).

Inhomogeneities within the conducting region have also been examined by Cuffin (1985) who used computer simulations to investigate the effect of fissures on the detected magnetic field. Fissures in the brain are filled with cerebrospinal fluid which has a conductivity three times greater than the brain tissues in which the sources are located. Such changes in conductivity are known to affect the potentials detected at the scalp. For example, the smearing of EEG data by the changing conductivity can make sources appear much deeper than they actually are (Nunez 1986). Amplitude changes in the scalp EEG can be as large as 25%.

In Cuffin's computer model the sources were located as shown in Figure 10. The surfaces of the volume conductor, including the fissure, were represented by triangular elements and the average potential of these elements calculated. The magnetic field perturbation due to a fissure is similar to the field produced by two secondary dipoles located on the internal side boundaries of the fissure and orientated perpendicular to the fissure surface. Analysis of the data with a simple dipole in homogeneous sphere model showed no significant differences in source location parameters caused by small fissures, but Cuffin calculated that an interhemispheric fissure might produce an error in location of up to 0.75 cm.

In assessing the value to be placed on these computer

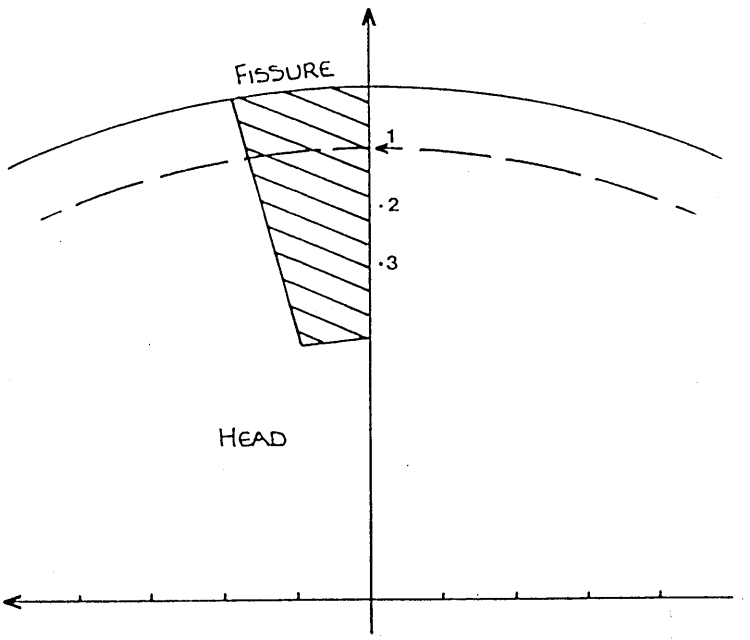

Figure 10 Cross section through Cuffin's head model and fissure. Three source locations are shown (situated 0.25 cm from the fissure)

based observations, it is important to note that the source model used has several assumptions. For example, the dipole is always assumed to be in a region of uniform conductivity but, in reality, that may not always be the case. Cuffin's group have gone on to attempt to validate their calculations by placing artificial dipoles in rabbit brains (Melcher 1986). These contain a single central fissure. This group reported that the magnetic field data were not significantly affected by the fissure. However these experiments are somewhat imprecise. Problems may arise from mechanical perturbations caused by the dipole placement and the appreciable size of the dipole with respect to the neurons in the local region.

Stok et al (1987) have investigated by computer the relationship between different models in forward and inverse problem analyses. A single current dipole was used as a source. Bare dipoles (i.e infinite medium), sphere, concentric spheres and a realistic head model were used to investigate volume conduction effects on the MEG and EEG. Forward computation with each model generated different field and potential distributions with the same source dipole. One model was used to compute the field generated by an input dipole using the forward procedure and another model used to compute the equivalent (i.e best fit) dipole from this field using an inverse procedure. The difference between the input dipole and the equivalent dipole reflected the difference between the models.

With all pairs of models, discrepancies beteen the dipole locations increase with increasing depth of dipole. A bare dipole inverse calculation and a sphere model forward calculation (signal to noise ratio of 10 dB) produced positional errors averaging 11mm. This result indicates significant differences between the bare dipole and the dipole in a sphere approximation.

Only the forward problem was tackled with the realistically shaped head model, with the main aim of the study being a comparison of fields produced in the head and sphere models. (The elemental nature of the realistic head model renders the inverse problem in this model numerically intractable.) The authors note from their brief examination, that the divergence between the predictions of the head and sphere models is small for superficial dipoles and increases with source depth.

This brief review of recent work on physical and computer models indicates some of the many problems associated with attempting to use and validate a dipole in a homogenous sphere model for human brain studies. The various reports suggest that, in brain studies, equivalent dipoles may be locatable with an accuracy of a few mm. However, there are indications of additional difficulties and inaccuracies that may exist in investigations of deep sources. In addition there remains some uncertainty over the effects

of nearby insulating boundaries. Clearly, a fuller survey is needed. In the next section, I will describe our own experiments and analysis in this field.

3.2 Apparatus And Analysis

Theoretical and empirical studies of ideal current dipoles within homogeneous conductors of idealised geometry (sphere, oblate, and prolate spheroids) have been reviewed briefly in the previous section. The investigations reported here were based on physical systems (as opposed to computer simulations), each consisting of an ideal current dipole within a conducting medium which is spherical, part spherical or (in the next chapter) skull shaped. The aims were to find the accuracy with which the position, orientation and strength of the dipole could be determined for the various geometries using a sphere model.

Methodology

The first system studied consisted of an 'ideal' dipole within a 'perfect' sphere. This investigation was intended to validate the accuracy of our techniques. The choices, of physical size and strength of the dipole, were constrained by the requirements of minimising the disruption to the volume current flow paths and preventing local ionic imbalances which would be caused by large current densities. The conductors bringing current to and from the dipole had to be arranged in a way that minimised stray magnetic fields. Magnetic materials, whose fields would obscure those from the dipole, were avoided.

For the dipole, a central silver wire (0.25mm diameter)

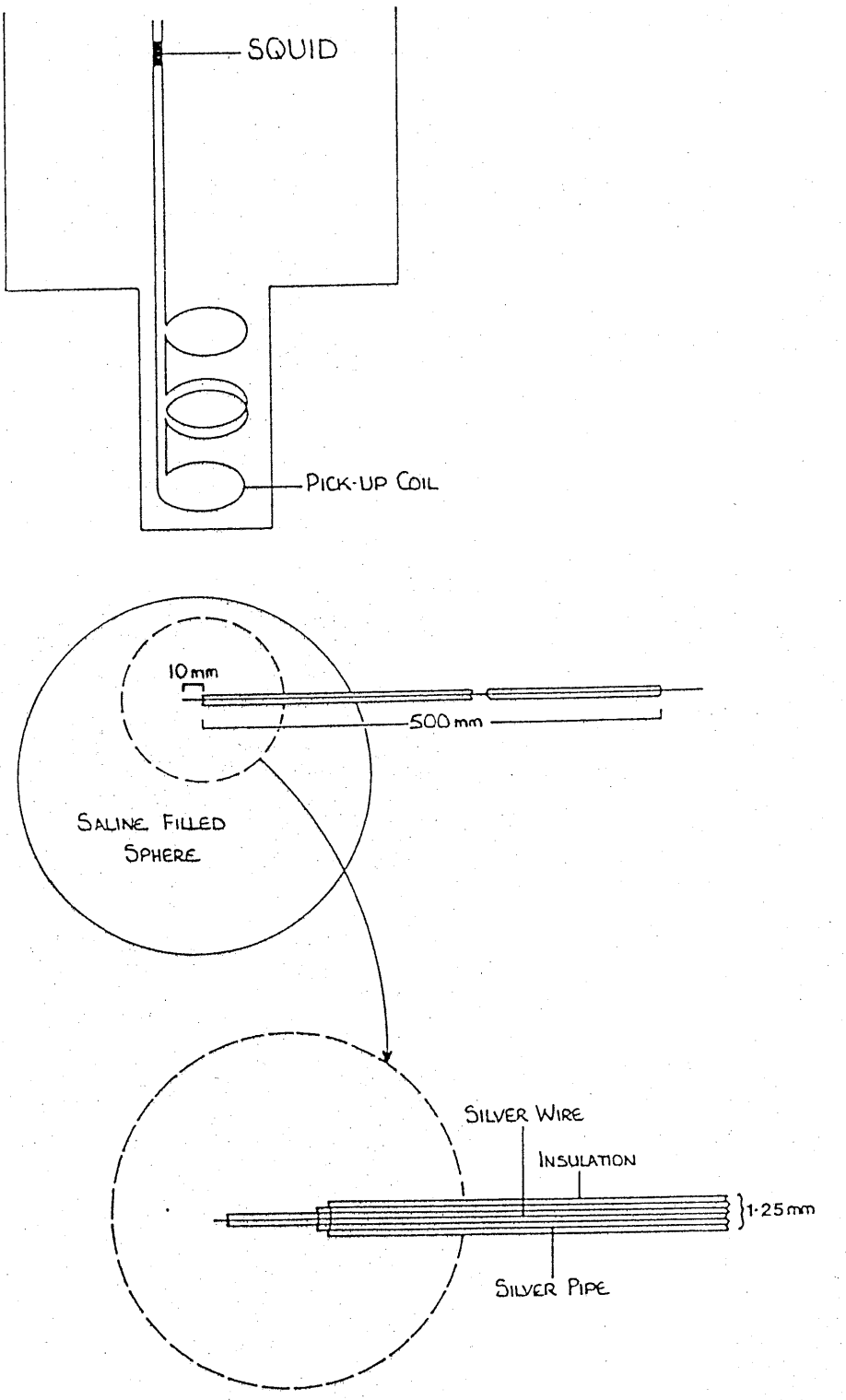

Figure 11 Dipole within a conducting sphere. The inset shows details of dipole construction

emerging from the end of a concentric silver pipe (internal diameter 0.75mm) was used as shown in Figure 11. The exposed conducting regions of the wire and the pipe (approximately 1mm length for the wire and 0.50mm length for the pipe) were chlorided to provide a stable reversible electrode system.

This dipole would itself, as a current element, give rise to a magnetic field of order 10^{-10} T at 5cm from the dipole if a current of 0.3mA and a 10mm dipole length were used. Because of the small fields involved, care had to be taken to ensure that the current leads to the dipole were non inductive. If the inner silver wire had been systematically displaced by 0.2mm from the cylindrical axis, a magnetic field of order 10^{-11} T would have arisen at the measurement site, with the same current. A 0.4mm o.d nylon coated glass tube with hair wrapped around it was used as the insulating sleeving around the wire and also to centralize the wire within the pipe.

0.1M potassium chloride solution in a 1 litre round bottom glass flask suitably modified with silicon rubber seals for solution and dipole entry was the arrangement used to create a spherical conductor. The magnetic field was generated by passing a sinusoidal current of appropriate frequency (180Hz) through the dipole from a Brookdeal signal source (Model 7473). After setting up the apparatus as shown in Figure 12, the dipole was positioned within

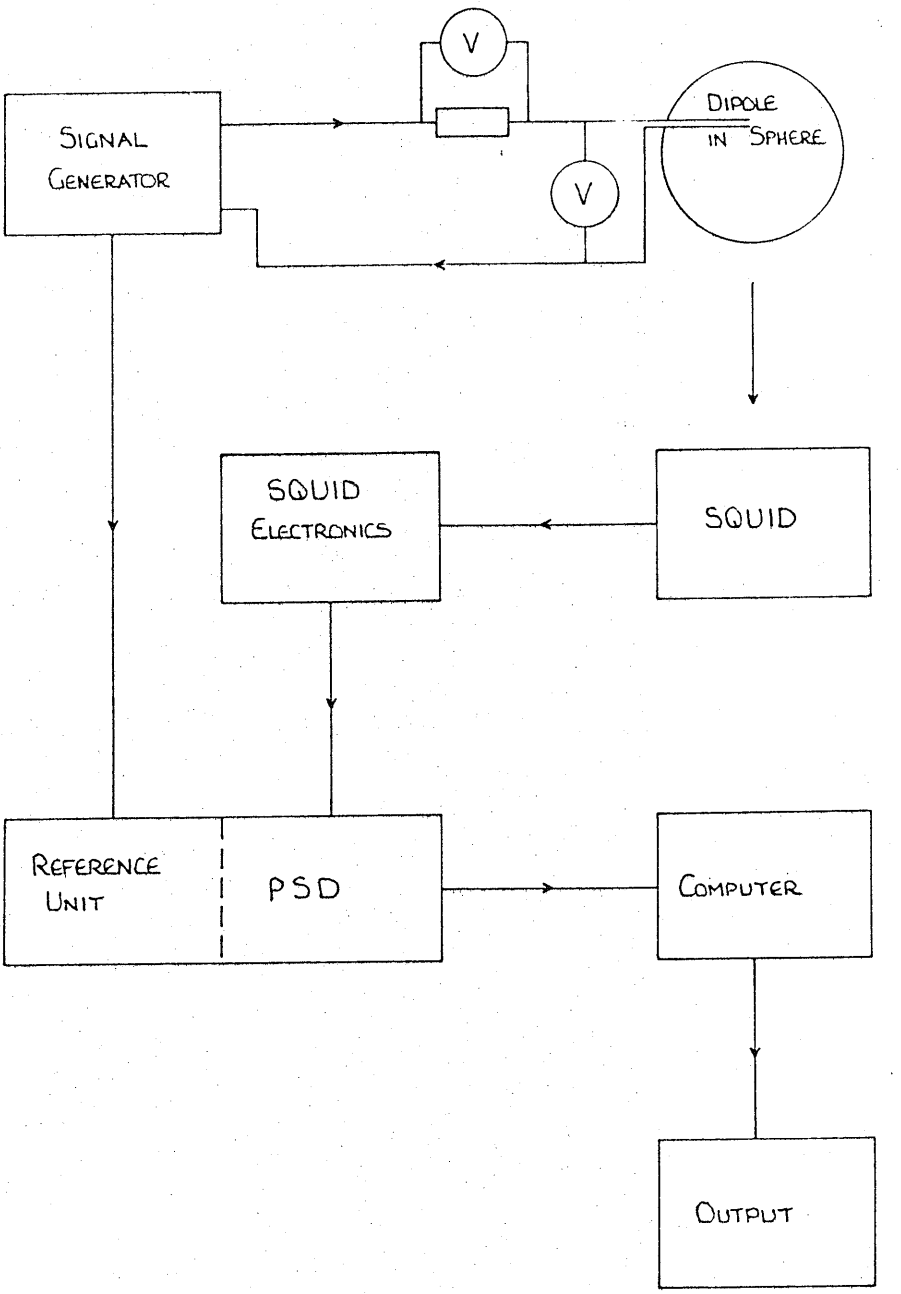

Figure 1.2 Apparatus for energising the dipole and detecting the magnetic field signal

the sphere at a fixed angle and orientation. Exact positioning was checked by laser alignment. The laser beam entered on one side of the sphere, crossed the dipole within the solution and emerged on the other side. A number of measurements of exit and entry points enabled the position to be calculated to an accuracy of ± 2 mm.

The ac current was monitored by measuring the voltage across a 10kΩ resistor in series with the dipole while another voltmeter, across the dipole itself, indicated any dc potential. The monitoring of these potentials allowed us to identify any local electrolytic effects which might alter the dipole's characteristics.

The magnetic fields produced by the dipole/conductor system were sensed with the SQUID magnetometer described previously. The filter (Kemo VBF/4) was replaced by a phase sensitive detector (Brookdeal 9305-SC) : the signal source that energised the dipole was used as the reference for the PSD. Output from the PSD was input to the computer as before.

An important feature of our measurement procedure is that the detector remains at a fixed position while the dipole/conductor system is moved in the horizontal XY plane below the detector coils. The more familiar strategy of orientating the detector along perpendiculars to the conductor surface is motivated by the wish to capture the

largest possible signal and by the observation that, for a spherical conductor, the radial field component is independent of the volume currents set up by the dipole source. The choice of planar scanning involves some loss of signal as, on average, the detector is further from the source than it would be if the scans were concentric about a sphere but, for non-spherical conductors, it involves making fewer assumptions in the modelling procedure (for example the insensitivity of the measurements to volume currents). It also avoids the introduction of errors due to incorrect orientation of the detector along perpendiculars to an often complex curved surface.

In each magnetic field mapping, the volume conductor (i.e sphere or skull) was moved along seven scan lines parallel to the X axis, usually separated by 1.4cm. The SQUID output at the excitation frequency was continuously sampled. The output signal from the SQUID electronics was input into the computer, via the PSD. This signal was averaged into bins corresponding to 5mm intervals of the X axis. For each scan line, data corresponding to seven of these bins at an appropriate spacing (usually 2 cm), were used as the input data for the fitting procedure (ie 49 data points in total). The locations of these measurement sites were accurate to better than 1mm.

The systems investigated in the first experiments consisted of perfect spheres with the dipole location

varying within the sphere. In the next stage, we considered spheres with defined distortions, again containing one dipole. However in biological systems there is often more than one dipole present. In these cases it is far from clear whether the dipole in a sphere model would be adequate. To address this question, a preliminary study involving two dipoles energised simultanously within a single conducting sphere was carried out. In each case a perfect conducting sphere was used with the two dipoles energised in parallel from the same signal generator. Individual potentiometers in series with each dipole ensured equal currents through the dipoles.

3.3 Results

Perfect Sphere

Three dipole positions (with the dipole central, slightly offset and extremely offset) were investigated. The signal (field) contour diagrams for each are given in Figure 13, together with the corresponding contour diagrams generated from the fitted dipole parameters (Table 3). I will discuss each of these cases briefly.

The magnetic field from a dipole, located at $X_d = Y_d = 0$, $Z_d = -3$ cm, in a perfect 6.5 cm radius sphere, centred at 0,0,-7.8cm, had a characteristic dipolar pattern (Figure 13a). Analysis of the field by the program previously described, yielded an excellent fit indicated by a low value for the misfit parameter ($R \approx 2 \times 10^{-3}$). The signal to noise ratio in the data would of itself, suggest a minimum value of R of this order. Choice of starting point in dipole parameter space did not affect the quality of the final fit. We have also, for this dipole, investigated the effect of errors in assigning the position of the sphere centre. These results are also summarized in Table 3. For the small shifts considered the predicted dipole location altered by less than 2mm for any axis. The diagrams regenerated from the fitted dipole parameters compare well with contour data from the experiment.

Moving the dipole to the position $X_d = 0.7$ cm, $Y_d = 0$ cm,

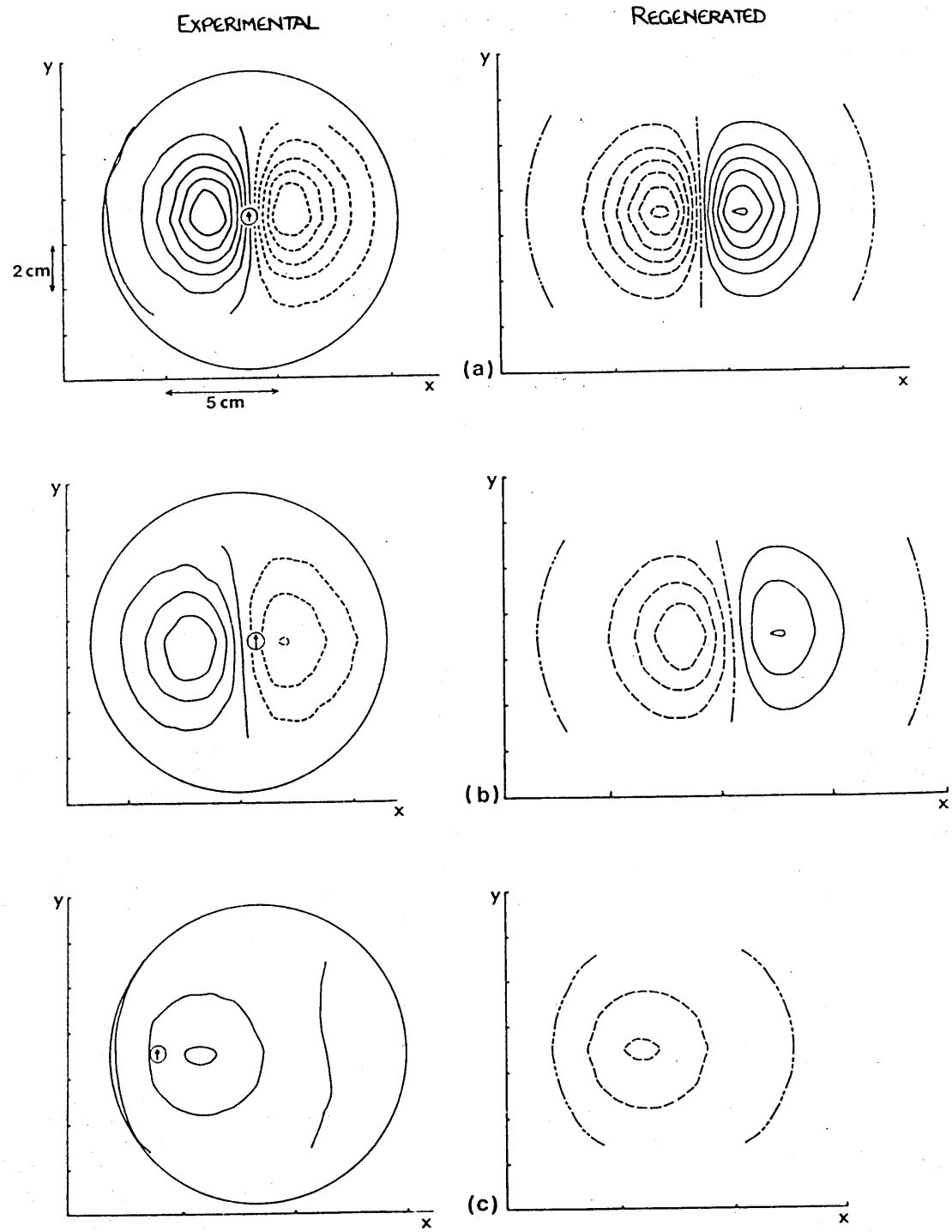

Figure 1.3 Experimental (solid lines denote positive field values) and regenerated (dashed line positive) data contour diagrams for the perfect sphere. a) dipole centrally located, b) dipole at X = 0.7 cm and c) dipole at X= -4.7 cm. Contours are at 4 pT

Z_d = -3.4 cm had little effect on the symmetry of the field pattern. The dipole parameters yielded by the model fitting procedure were close to the correct values with an error of less than 2 mm in dipole location. The quality of fit, as indicated by the value of R, was again close to the noise limit.

With an extremely offset dipole (X_D = -4.7 cm, Y_D = 0 cm, Z_D = -5.4 cm) the detected magnetic fields changed markedly to one that was highly asymmetric. The pattern was reminiscent of that given by a horizontal current loop, as might be expected given the path of the return current flow. The fitting algorithm predicted the dipole location with an accuracy of better than 6mm for each coordinate. Again the regenerated data contour map was similar to the contour map from the experimental data and the value of R was correspondingly low (although higher than the other two examples because of the reduced signal to noise ratio).

Clearly the experimental procedures and the fitting algorithm are validated by the above results for a perfect sphere with a centralized dipole. The data suggests experimental uncertainties of $\Delta X_D = \Delta Y_D = \Delta Z_D \approx 2$ mm, $\Delta\alpha$ = 2° and $\Delta P/P$ = 6%.

Table 3

Differences between the predicted and known dipole parameters for the perfect sphere data. There was no observable correlation involving the sign of the errors and they are only shown as magnitudes.

Dipole	ΔX_d/cm	ΔY_d/cm	ΔZ_d/cm	$\Delta\alpha$/°	$\Delta P/P$ %	R/E-3
Central 1	0.00	0.20	0.09	1.8	5.6	1.87
Central 2	0.03	0.21	0.22	1.8	2.0	1.86
Central 3	0.10	0.40	0.09	1.9	4.7	1.89
Offset	0.12	0.12	0.10	3.9	17.0	1.90
Extreme Offset	0.60	0.18	0.10	4.6	0.06	11.00

The effect of choosing an incorrect model sphere centre position is indicated by fitting the data from the central dipole with the known sphere centre position (Central 1), with a 1 cm greater scan plane to sphere centre distance (Central 2) and with the sphere centre shifted to y = 0.5 cm (Central 3).

The dipole was offset by 11% of the sphere radius from the central z = 0 axis for the offset dipole and 73% for the extreme offset dipole.

Partial Spheres

In this section the effects of simple departures from perfect sphere conducting volume are reported. The sphere was partially filled with a non conducting resin which formed an insulating region with a known plane boundary. This partial sphere geometry has some similarity to the skull with its 'flat floor', 'planar' temporal surfaces and 'spherical' posterior surface. In the first example, the lower half of the volume was occluded (Figure 14a). A dipole located at $X_d = Y_d = 0$ cm and $Z_d = -2.8$ cm gave a characteristic dipolar pattern and when analysed by the fitting program, yielded an excellent fit as indicated by a low R value (Result 1 Table 4a).

All other experiments on partial spheres involved vertical boundaries i.e the Z axis lies in the plane of the boundary. Figures 14 and 15 show the position of the boundary and the dipole position for the 8 examples considered. In all of these cases the dipole was parallel to the plane boundary. This orientation was chosen for simplicity and also because, in the brain, detectable signal sources are located adjacent to fissures and are approximately parallel to boundaries.

Analysis of data from non-spherical conducting geometries using a sphere model is complicated by the necessity to choose a position for the centre of the effective conducting sphere. In effect, this introduces a further

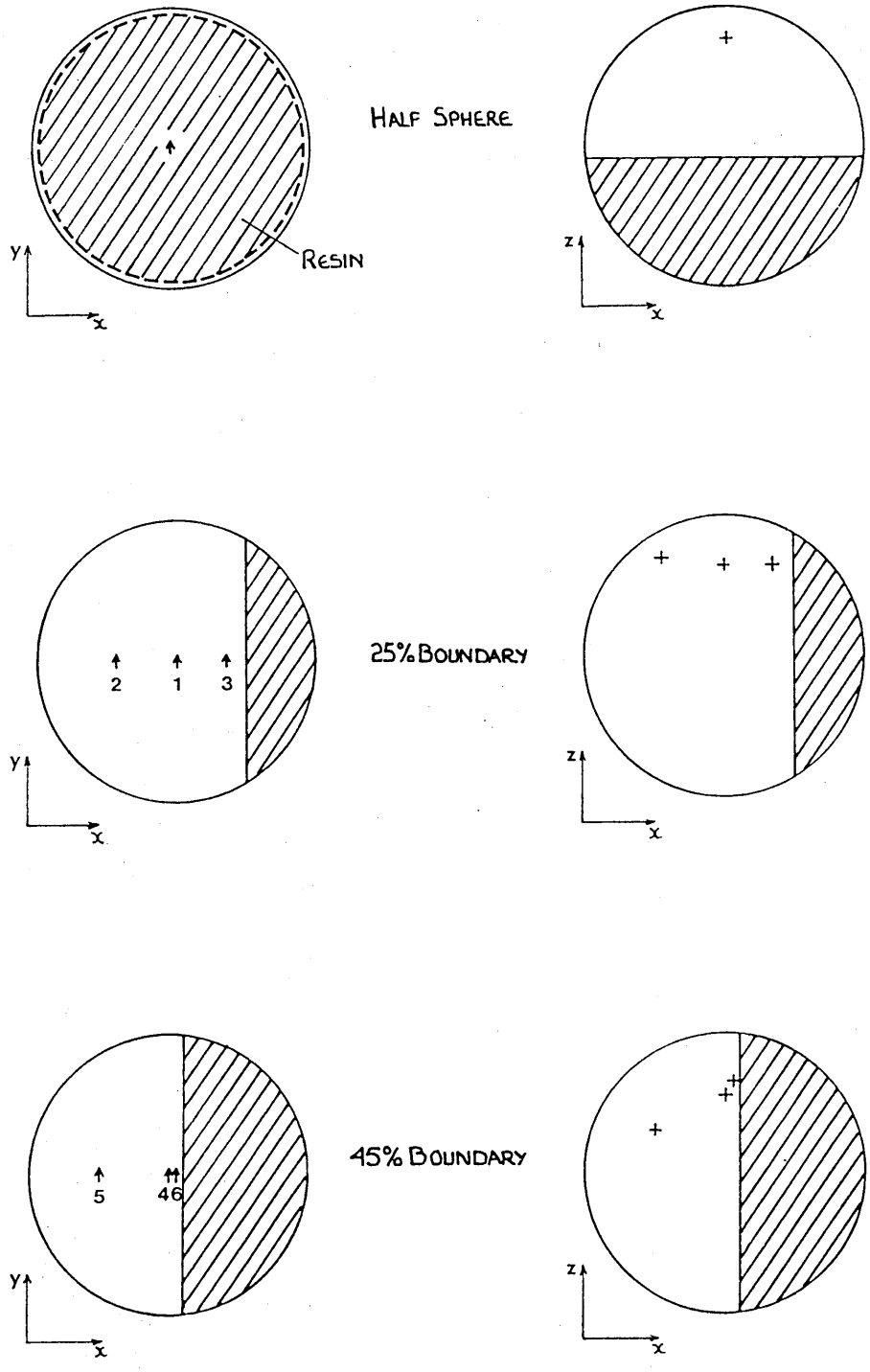

Figure 14 Dipole location and boundary extent for partial sphere experiments

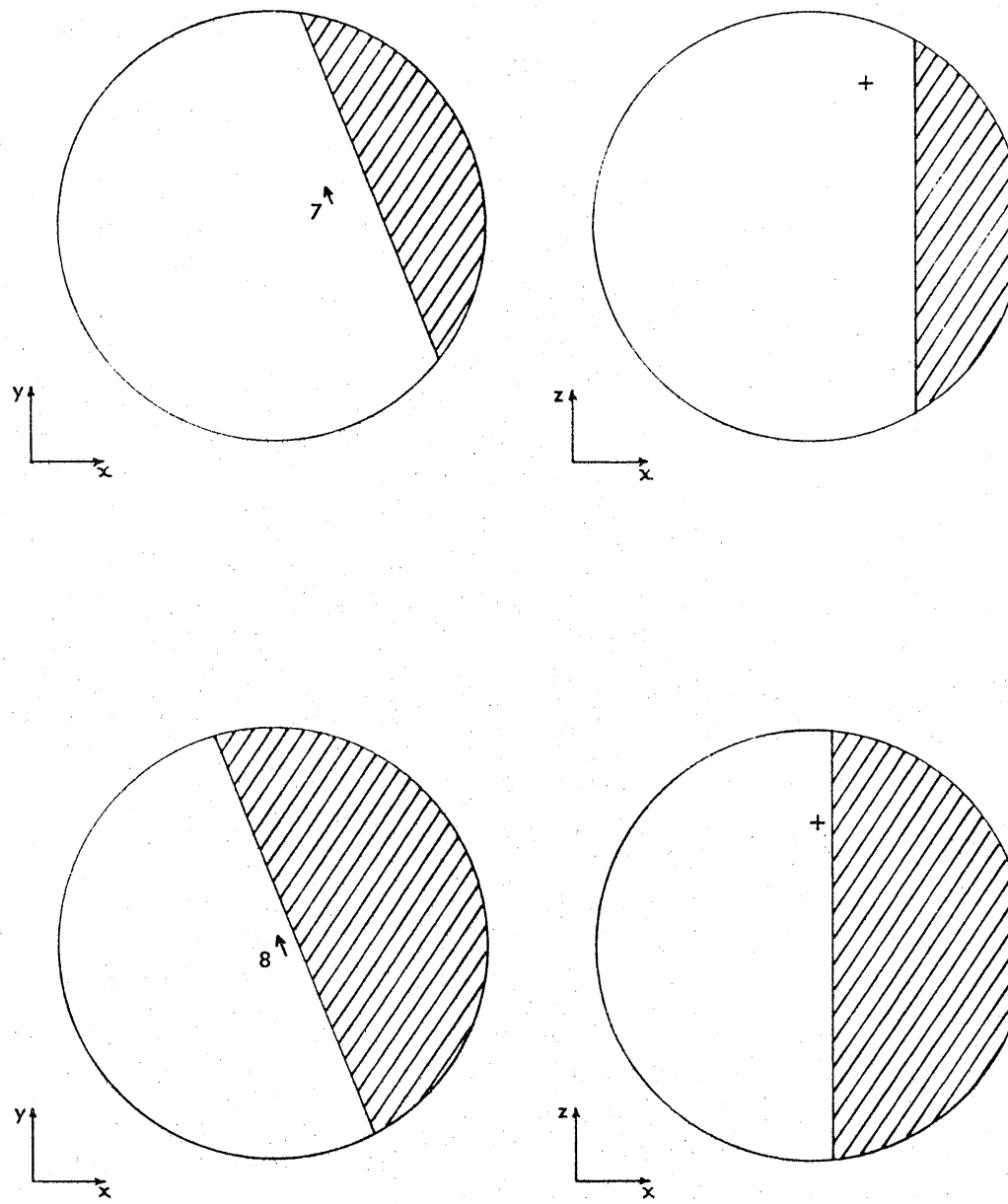

Figure 15 Dipole locations and boundary extent for generalized dipole experiments

three unknown parameters into the fitting procedure. We have investigated how both the accuracy of prediction of the dipole parameters and the accuracy of fitting the data, which is quantified by the minimized error parameter R, depend on the choice of model sphere centre. For each system, the fitting program was run several times, choosing in turn the model sphere centre to lie on the points of a three-dimensional cubic grid of spacing 1cm. The value of R and the corresponding dipole parameters were found to depend strongly on the choice of model sphere centre. The whole issue of best fit had to be reappraised.

One possible model sphere centre is the centre of the glass sphere itself. This choice, used for the perfect sphere data, was reasonably successful in five of the nine systems in that the dipole parameters were predicted with an accuracy broadly consistent with the estimated uncertainties in known dipole parameters. The minimized error parameter showed some degradation in the quality of the fit when compared with the perfect sphere results but the quoted average value of $R = 0.036$ (Table 4a) still represents only a 6% difference between fitted and measured signal at each data point. However, in one case, a partial sphere in which the dipole was only 9mm from the electrolyte-resin boundary, the discrepancies were large with this choice of model sphere centre and so was the corresponding minimised error parameter.

Table 4a

Moduli of differences between predicted and known dipole parameters for partial spheres

	ΔX_D/cm	ΔY_D/cm	ΔZ_D/cm	$\Delta\alpha$/°	$\Delta P/P$%	R/E^{-3}
Half sphere	0.02	0.00	0.34	4.7	6	1.5
A Using sphere centre value						
25% boundary						
Central (1)	0.18	0.01	0.08	0.3	22	7.6
Away (2)	0.15	0.16	0.27	1.2	36	8.9
Close (3)	0.13	0.43	0.18	0.0	19	29.4
45% boundary						
Central (4)	0.75	0.76	1.33	17.3	49	71.2
Away (5)	0.12	0.21	0.52	2.6	43	16.0
Close (6)	0.70	0.60	2.05	6.0	108	87.0
Average discrepancies using sphere centre values						
	0.33	0.36	0.73	4.5	46	36.6
B Using lowest R values						
(1)	0.14	0.00	0.09	1.2	20	5.4
(2)	0.13	0.17	0.29	1.2	40	7.9
(3)	0.12	0.27	0.13	0.0	8	10.2
(4)	0.20	0.25	0.33	0.8	13	17.1
(5)	0.14	0.10	0.40	1.0	32	13.0
(6)	0.23	0.35	0.50	6.0	49	19.0
Average discrepancies						
	0.16	0.19	0.29	1.7	27	12.1

Table 4b

Differences between predicted and known dipole parameters for dipoles 7 and 8. A refers to values corresponding to sphere centre position, B to lowest R position and C the composite prediction from nine lowest R positions

	ΔX_D/cm	ΔY_D/cm	ΔZ_D/cm	$\Delta\alpha$/°	$\Delta P/P$%	R/E-3
Generalised dipole 25% boundary (7)						
A	0.60	0.50	0.11	4.0	9	21.2
B	0.98	0.00	0.48	7.0	29	17.3
C (lowest 9 R)	1.03	0.03	0.56	8.0	49	17.8
Generalized dipole 45% boundary (8)						
A	1.05	0.76	1.04	16.0	66	57.0
B	0.77	0.11	1.65	84.0	21	15.0
C	0.26	1.06	0.60	45.0	18	17.0

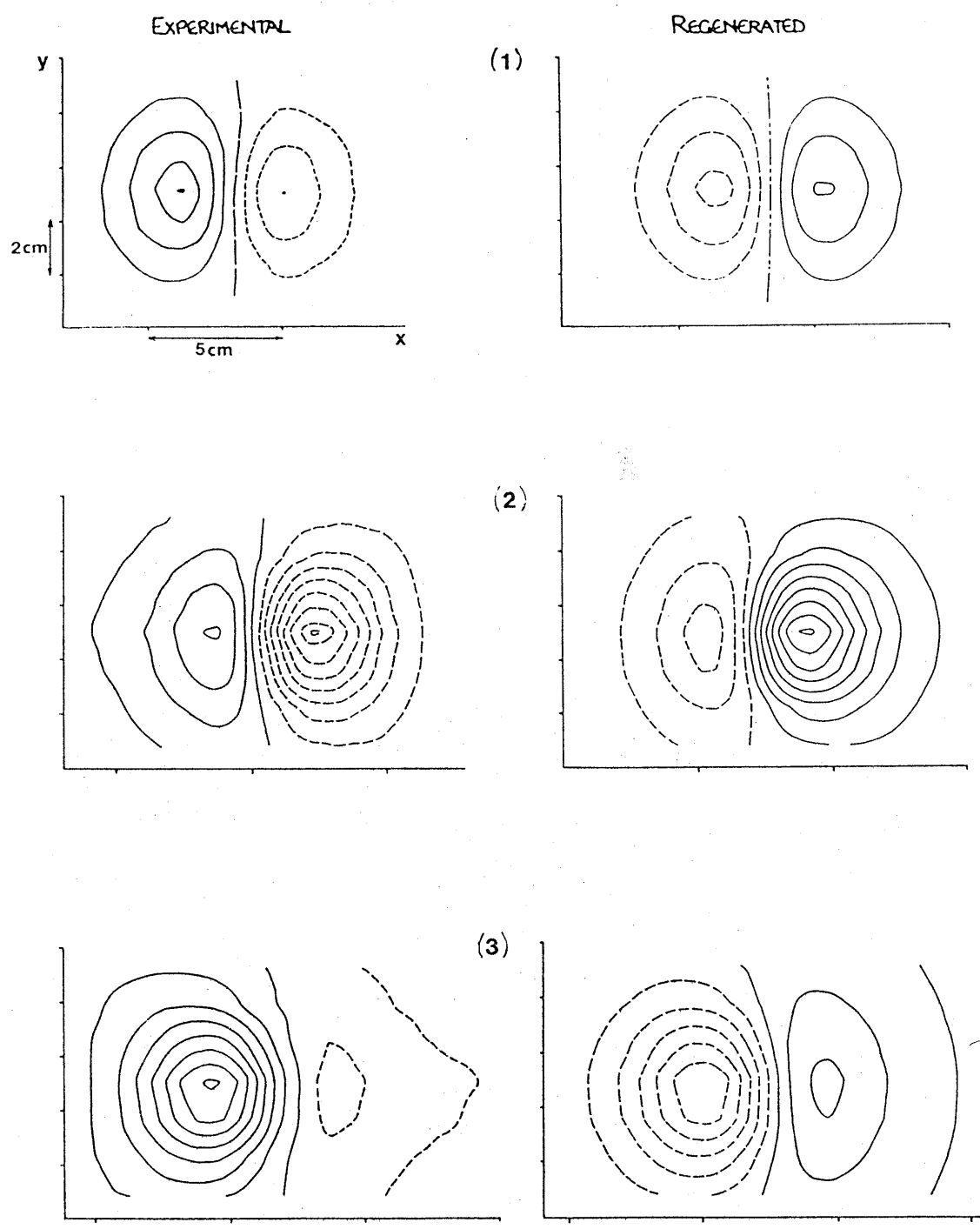

Figure 16 Experimental (solid lines positive) and regenerated (dashed lines positive) data contours for the 25% occluded volume. Dipole locations 1, 2, 3 are shown on Figure 14

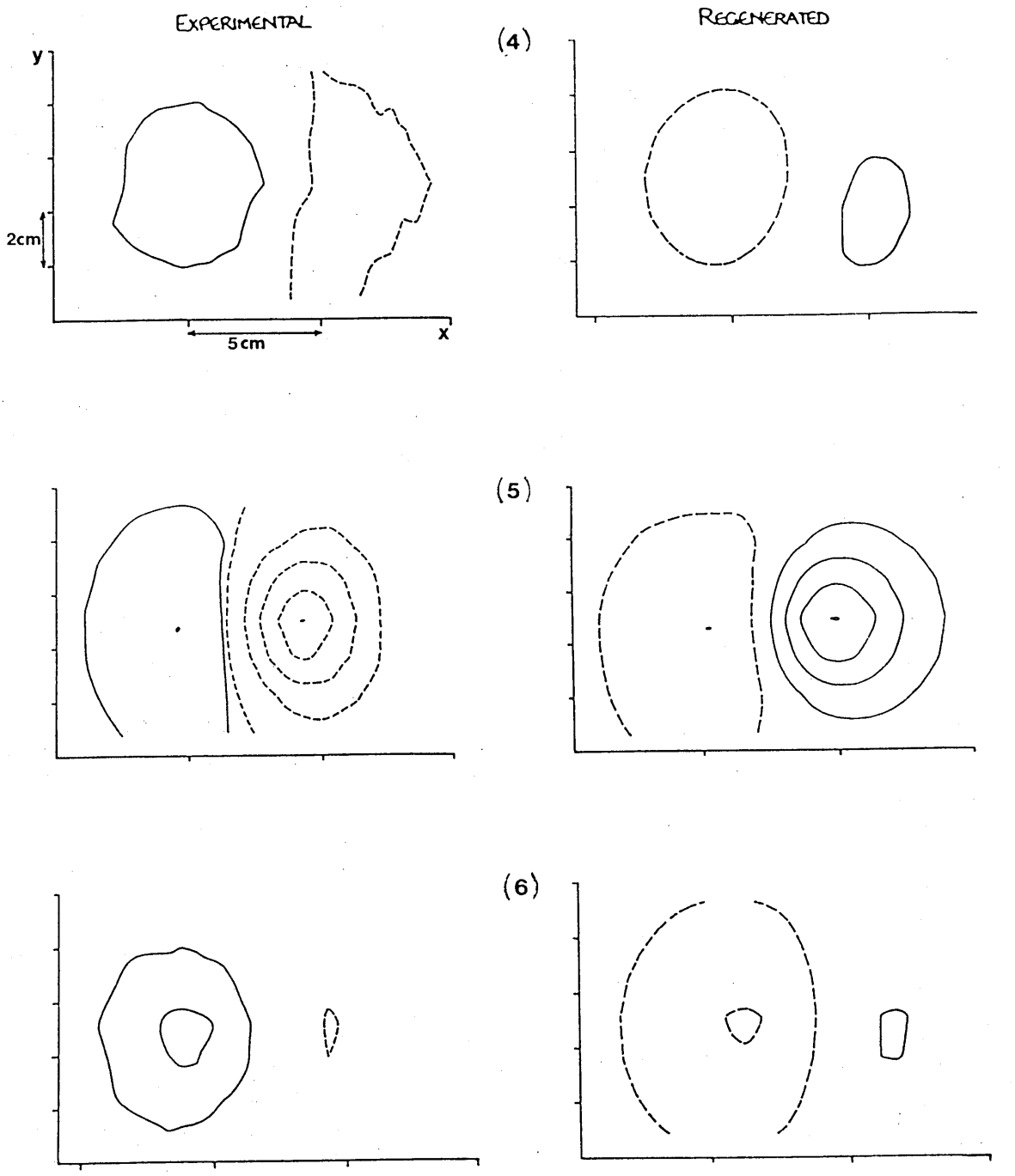

Figure 17 Contour diagrams of the experimental (solid lines positive) and regenerated (dashed lines positive) data for dipoles in a conducting sphere with 45% of the volume occluded. Dipole locations 4, 5, 6 are shown on Figure 14

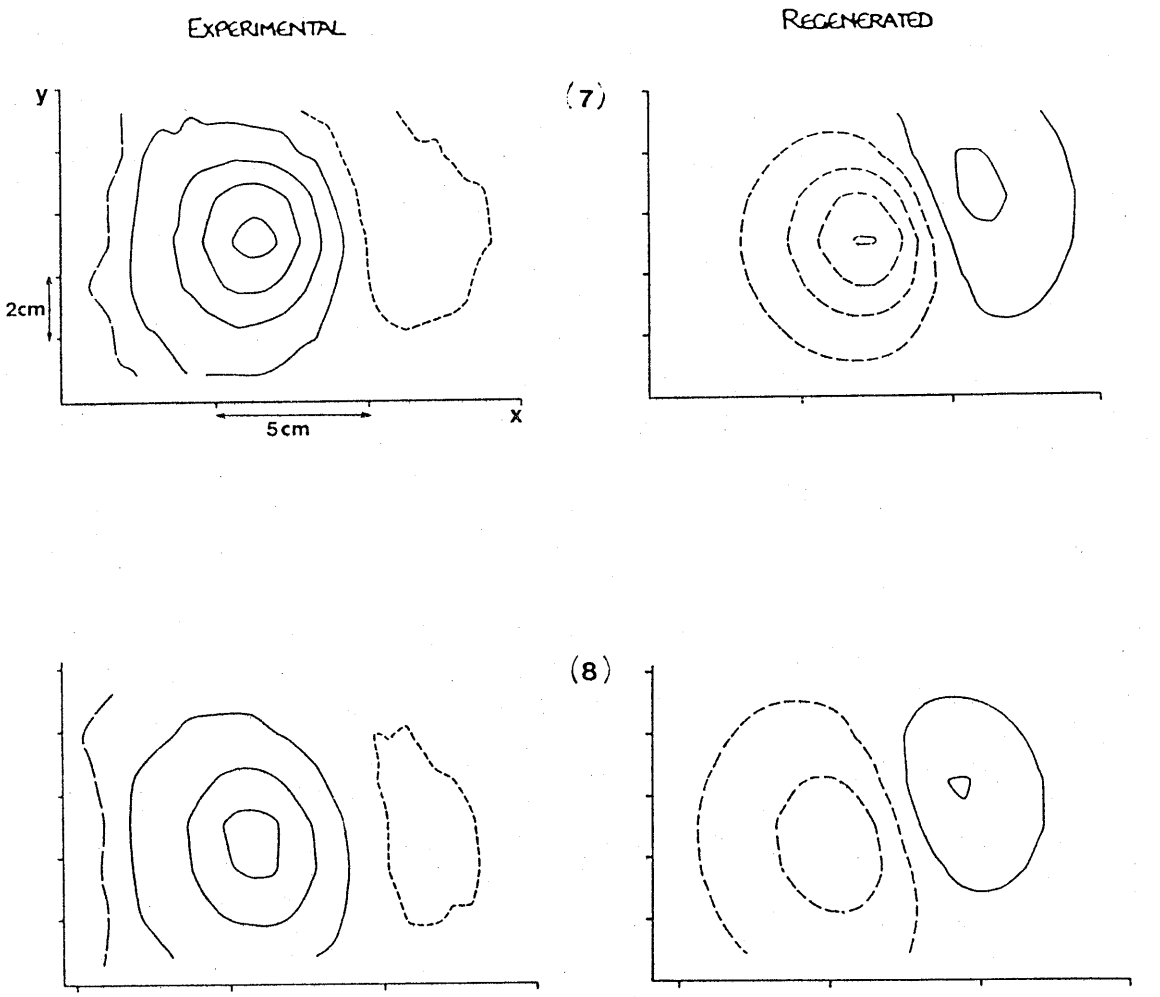

Figure 18 Generalised dipoles; comparison of experimental (solid lines positive) and regenerated (dashed lines positive) data contour diagrams. Dipole locations 7, 8 are shown on Figure 15

A second possible method of choosing the model sphere centre is to identify the position corresponding to the lowest value of R, designated as choice B in Table 4a. With this choice the accuracy of the dipole identification is not significantly improved for four of the partial spheres 1-6. Systems 4 and 6 were improved. The discrepancies between known and predicted dipole parameters using this method are given in Table 4a. Contour data is regenerated using these predicted dipole values and compared with data from experiment (Figures 16-17).

The two remaining dipole systems were of a more general nature in that the boundary did not lie along the Y axis. At this point it is worth noting that there is a correlation between the value of R and the accuracy of dipole characterization, but it is quite loose. This can be illustrated by considering the dipole parameter predictions for partial sphere system 8. For the restricted set of sphere centre positions corresponding to R less than 0.10 there are variations of ΔX_D =1.0cm, ΔY_D =0.8cm, ΔZ_D =0.7cm, $\Delta\alpha$ =60^0 and $\Delta P/P$ =80% in the predicted dipole parameters. The variation of R with the sphere centre position for this system is shown in Figure 19. From this figure, it is clear that a 'good fit' can be obtained for a wide variety of model sphere centres, suggesting that the model is robust. However this view must be qualified by the observation that, for all the

systems studied, the good fits obtained with small radius spheres centred near the dipole tend to provide poor dipole characterisation.

Figure 19 suggests an alternative method of 'choosing the sphere centre position'. If contours of the R value are drawn over the cubic grid of model sphere centre space, any abrupt changes in R can be identified and reconsidered. Then by taking an average of the predictions obtained by several of the best fits, a set of dipole parameter values can be obtained that are not prone to error resulting from one sphere-centre position yielding (fortuitously) a low value of R but poor dipole prediction. Nine best fits, identified by the values of R (but not including any obviously erroneous solutions), were averaged to provide composite predictions designated as C in Table 4b. Similar values were obtained for most of the error parameters for all nine best fits. This strategy appears to be partially successful in that the localization of the dipole for the problematic case, system 8, is significantly improved. However, this process of averaging is of little value for the (majority of) systems where the accuracy is close to the calculated limit set by error contributions from the signal noise and positioning errors.

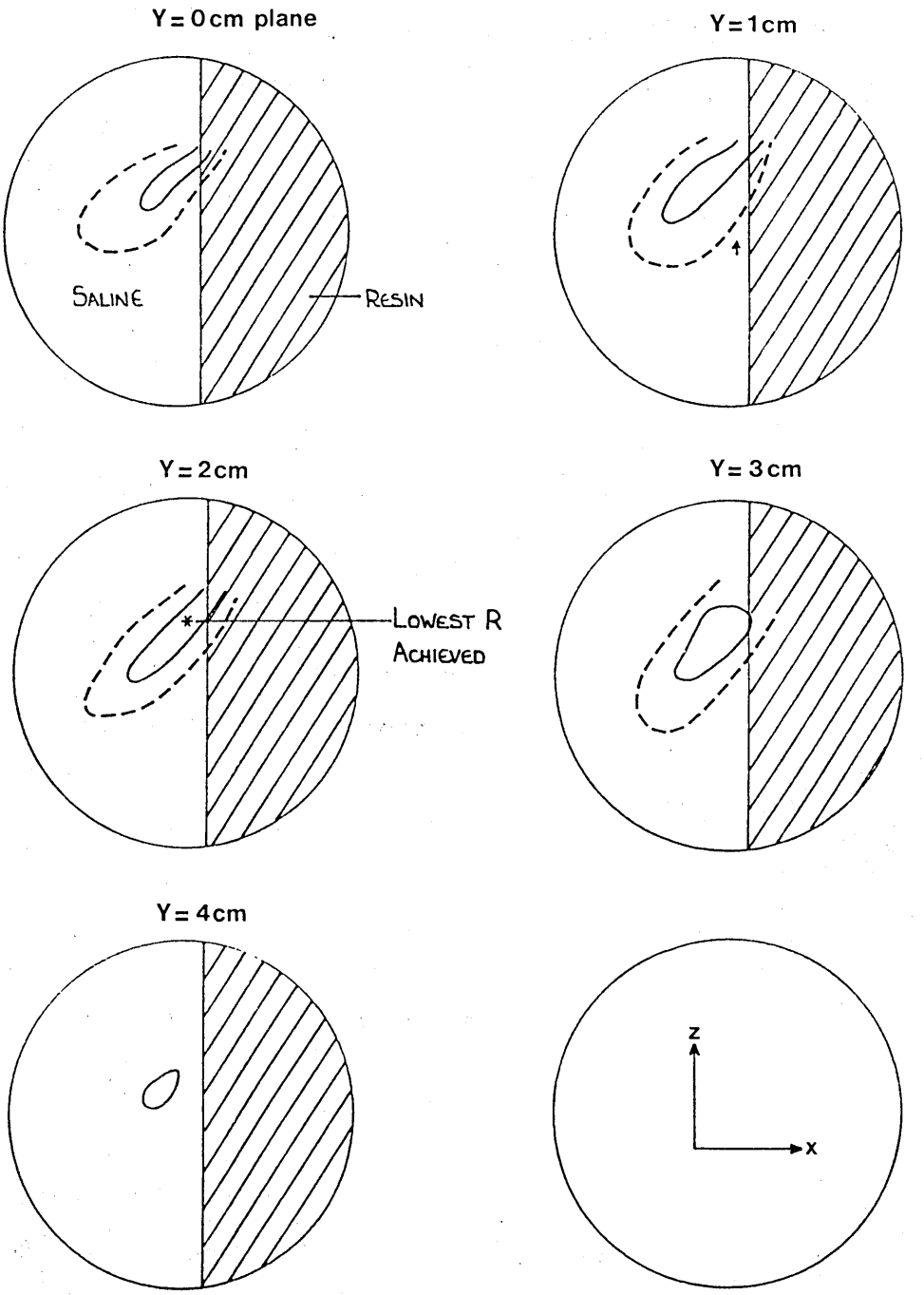

Figure 19 Dependence of the 'goodness of fit' parameter (R) on the choice of model sphere centre for the 45% boundary generalized dipole example. The diagram shows a series of xz plane cross sections. Contours link model sphere centre positions giving equal values of R (R= 1E-2 solid line, R= 2E-2 dashed line)

Multiple Dipoles

Figure 20 shows contour diagrams and locations of dipoles for 4 of the multiple dipole experiments. In the first case (Figure 20a), the dipoles were separated by 64 mm along the X axis and 8 mm along the Y axis. Two overlapping but discernably distinct dipolar patterns can be seen. In the central region between the patterns, another dipole with opposite orientation could be postulated. As the separation between the dipoles is reduced below the diameter of the pick up coil, the field pattern comes to resemble that of a single dipole. The dipole separation in Figure 20b was 22mm along the X axis with a common Y coordinate. Our pick up coil has a diameter of 23.5 mm.

Increasing the separation of the dipoles along the Y axis tended to elongate the dipolar pattern (Figure 20c) but, at least in this example, there remained a strong resemblance to a single dipole contour map.

A special case of two dipoles separated by 5 mm along both X and Y axis but with a 20 mm separation along the Z axis and with the currents in the opposite directions yielded a complex contour pattern (Figure 20d).

The multiple dipole data was again analysed using the single dipole in a conducting sphere model. By exploring the model sphere centre space, dipole parameters could be

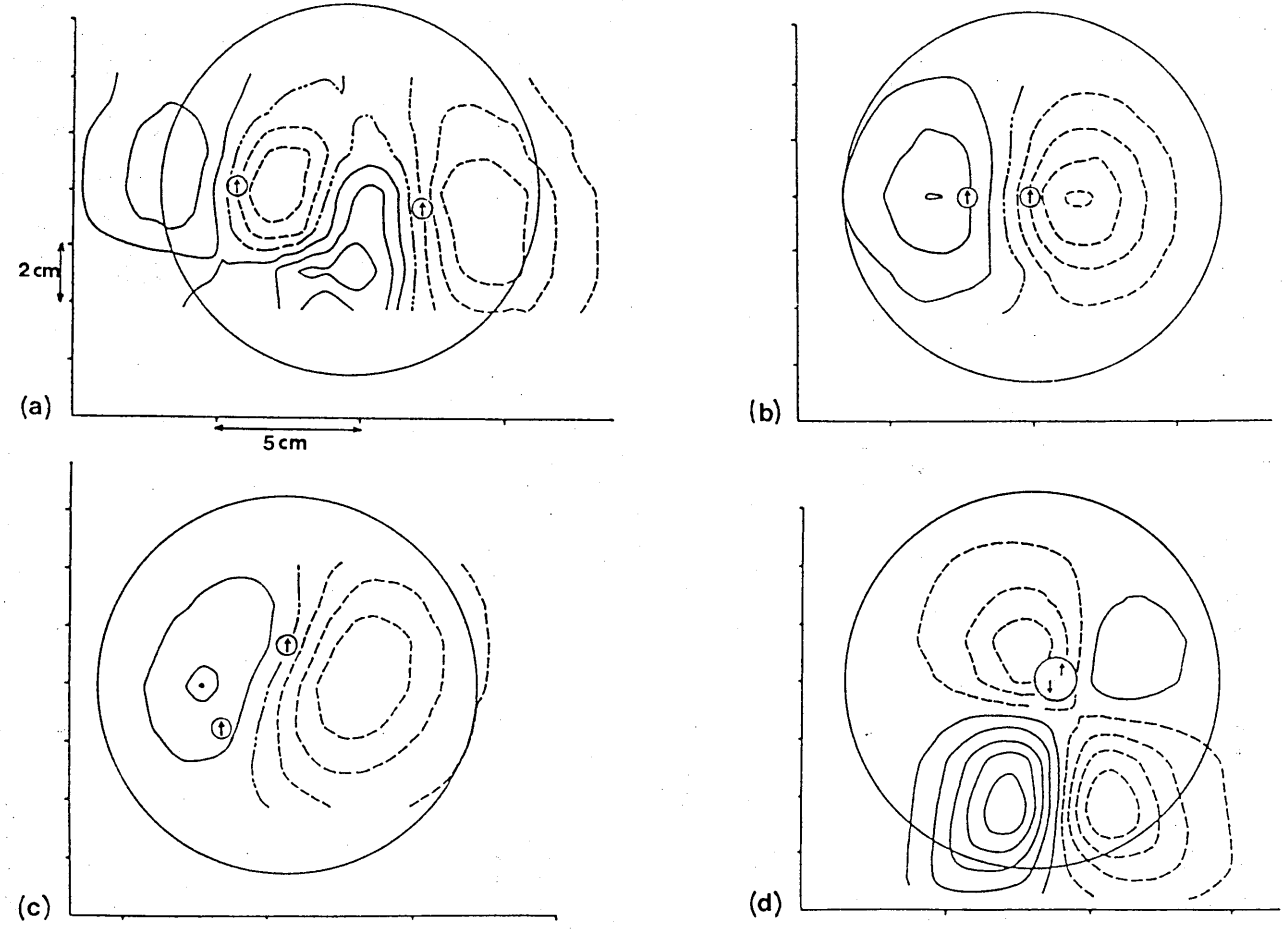

Figure 20 Multiple dipoles in a conducting sphere (experimental data). The region of the conducting sphere and the locations of the dipoles are shown on the field signal contours

successfully predicted in some instances. In example (b), an equivalent dipole could be easily found. This was not surprising because of the strong resemblance to a single dipole pattern. The equivalent dipole parameter values represent an average of the dipole location parameter values but with greater strength and depth.

An equivalent dipole could also be readily found for example (c). This time however, the R value was larger. This and the systematic differences between the contours predicted by the equivalent dipole and the experimental data contours may be used as an indication that something is wrong, i.e may indicate the presence of more than one dipole.

The two remaining examples pose problems. If, in example (a), the entire data set is taken, a consistent equivalent dipole cannot be predicted. However, by spatial partioning of the data into two regions resembling dipolar patterns, and then analysing each subset separately, two equivalent dipoles can be predicted. The average location errors were less than 0.95 cm (with the greatest error in depth), 28° in orientation and 68% in magnitude for each dipole when only data points close to the dipole were considered. The average R value was 2.3×10^{-2} indicating, in each case, a good fit comparable to the fits obtained for single dipoles in the partial sphere experiments. The number of data points chosen for each fit was 21 instead of 49: it

is probable that the reduction in the number of data points reduces accuracy.

For the current reversed system (example d) a whole series of possible equivalent dipoles resulted from the analysis with little indication as to which was the most appropriate, thus emphasizing that there is no point in trying to deduce equivalent dipoles if the contour map is obviously not of dipolar form. Spatial partitioning in this instance was not successful. Perhaps scanning in a different plane or considering the radial component as well would be more successful in situations like this.

3.4 Discussion

The results in this section show that for the simple, single dipole cases considered, it is possible to use a homogeneous sphere model in attempting to characterise a dipole field source in a non-spherical volume conductor. In all but two examples the accuracy in the predicted dipole position was better than 5 mm for each axis and the discrepancy in orientation was less than 10° (when the most appropriate values A, B, or C were chosen). However, the magnitude prediction was less satisfactory, with errors of ≈50% observed even when the lowest R values were chosen. There were no systematic discrepancies in the dipole parameters, except for a linking between an overestimate of Z_d (i.e dipole depth below the detector scan plane) and an overestimate of dipole strength. This compensation is predictable and obviously occurs too for underestimates.

It is useful to consider the example (Figure 15) where our fitting procedure was least successful. In this case, the inaccuracy of dipole characterization was signalled by the significantly larger values of R suggesting that quoting a value for this misfit parameter is a useful (though not infallible) indicator of the confidence to be placed in a particular dipole prediction. The reason for the apparent inappropriateness of the sphere model in this example may well be the close proximity of the dipole to the non-conducting boundary (9mm gap). Given the length of the

dipole (7mm) our physical model may not be adequate, but, even assuming that this is not a significant factor, the large values of potential on the nearby surface will tend to produce an appreciable volume current term in the observed field.

Perhaps the most important technique introduced in this section is the inclusion of the sphere centre position (3 parameters) in the fitting procedure. The potential usefulness of this more generalized analysis is indicated by the improvement in dipole characterization for system 8 and by the observation that reliable dipole parameter predictions seem to occur for regions of sphere centre parameter space where R is insensitive to small displacements

Although the data is only exploratory and does not constitute a full survey, the multiple dipole cases do suggest that by careful analysis of spatially differentiated subsets of the data, more than one equivalent dipole can be predicted. This technique is worthy of fuller investigation. However it is clear that prediction of parameters for dipoles in close proximity may be limited by the size of detector and by the overlap of the contributions of the separate dipoles to the observed field.

DIPOLE IN A SKULL.

4.1 The sphericality Of The Cranial Vault

After investigating the effects of plane boundaries on the detected magnetic fields, the experiments were further refined to take account of the complex internal geometry of the cranium. Several authors have quantified the non sphericality of the skull. Pistella et al (1987) used an electromechanical craniometer, Meijs et al (1986) used NMR data and several groups are using 3-D location digitizers. However these and the above observations do not appear to take into account the radical departures from sphericality in certain regions within the cranium. The inner and outer surfaces of the skull differ markedly in their profiles. We have investigated the effects of these departures empirically. Before detailing the dipole experiments, I will discuss briefly our method of determining the sphericality of the cranium. The remarks are not meant to be an exhaustive description, but rather to illustrate the complexity of the geometry.

A perspex frame 20x20x20cm was designed to hold a dry human skull in a fixed position (Figure 21). A series of brass pins 13cm long and of 4mm diameter with cone shaped tips were inserted horizontally at 1cm intervals through a square frame holder that could be moved on the frame in the vertical direction. The pins were pressed in to touch the skull at a given common height. This yielded an outline of the skull in a given XY plane from the amount

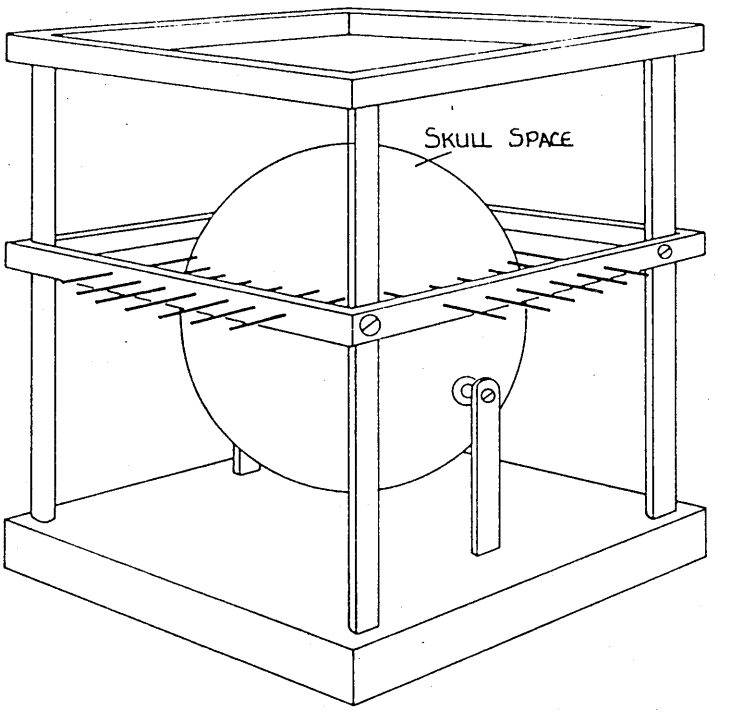

Figure 21 Pin gauge for accurate measurement of the external curvature of the skull

of pin protruding from the frame. Each point of contact on the skull was marked. The holder assembly was then moved through 1cm in the Z direction and the process repeated until all cross sections were obtained.

The skull was sectioned and a micrometer with an enlarged and angled throat was used to measure the skull thickness at the points of contact with the pins. Care was taken to ensure that the micrometer was held so that the thickness was measured in the same direction as the pin for each point of contact. The inner profile of the cranial vault was then calculated. (Although orthogonal radiographs were utilised to determine the outer profile of the skull as a whole, they were not sufficient to determine the variablity of the inner profile of the cranium). Comparison of the inner and outer profile for just one cross section are shown in Figure 22. Some regions with much greater thickening of the bones than other regions can clearly be seen. Curvatures of the outline were measured to fit spheres of appropriate radii around the skull. The cranial centre, (designated by a 64 mm radius sphere for the sagittal plane depicted in Figure 22) may be appropriate in some cases, but for dipoles located in the posterior regions other sphere centres (i.e a 48 mm sphere to fit the local curvature) may be equally appropriate.

This brief illustration emphasises that analyses which

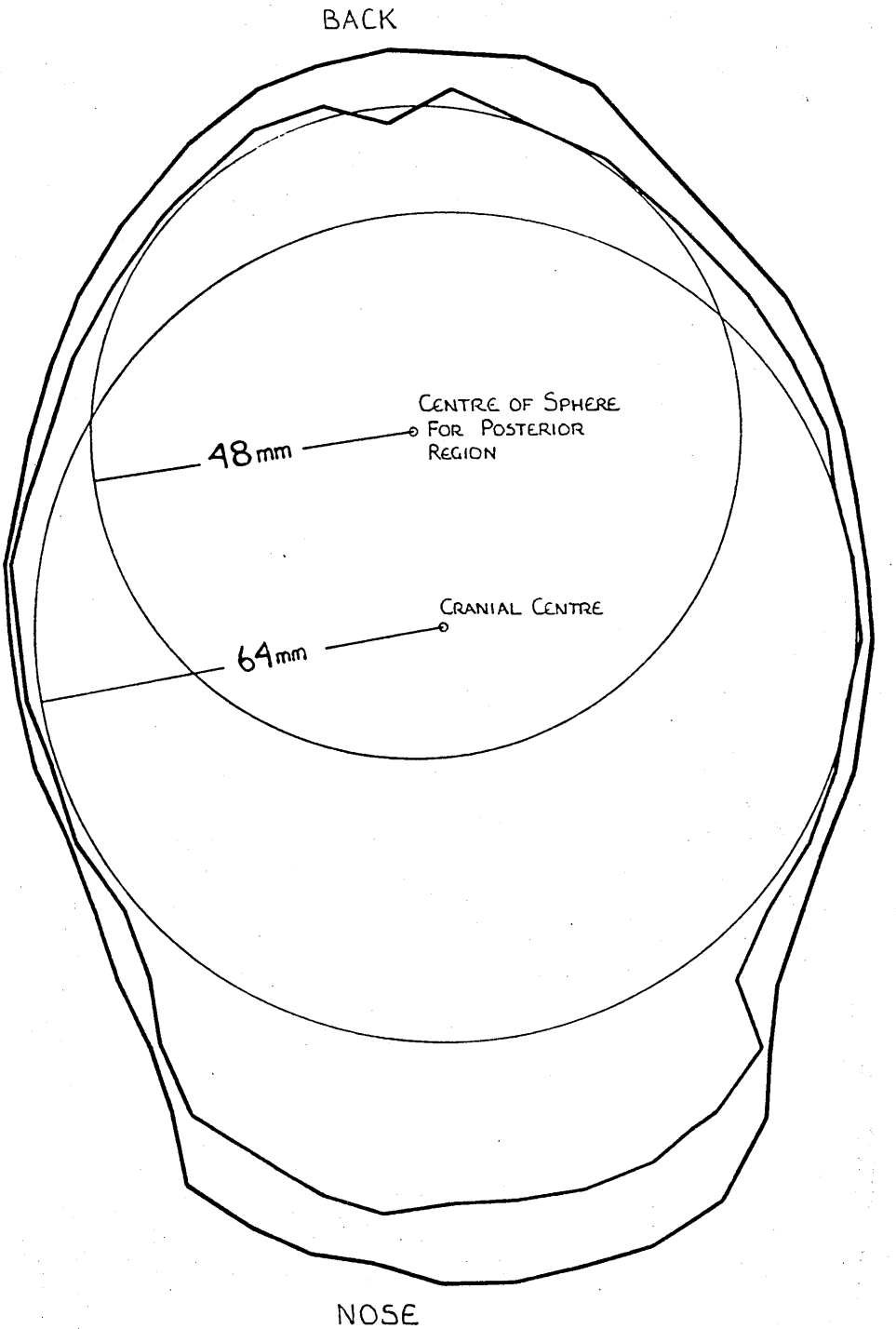

Figure 22 Comparison of the internal and external cross sections of the skull along a sagittal plane. Various model spheres can be located within the local skull volume

proceed on the basis of a homogeneously conducting sphere with an assumed centre may contain a serious source of error. The appropriate choice of sphere centre is not obvious. In our method of analysis this difficulty is overcome by scanning through all reasonable sphere centre positions.

4.2 Dipole In A Skull - Physical Arrangement

In this section, the preparation of the dipole in a skull model will be described. A thin layer of sealant was painted onto the inner surface of the dry skull to prevent any moisture uptake from the gel. Small quantities of Camjel (Picker) were syringed into the skull through a small drilled aperture. Care had to be taken to avoid aeration of the gel as any small bubbles created would impede current flow. This was particularly important in the region of the dipole where cavitation might lead to significant distortions in the current path. After allowing the gel to settle, more gel was syringed in until the skull was completely filled.

The skull was positioned in an X-ray translucent frame with the dipole (as previously described for the sphere experiments) in a defined location and orientation. Anterior posterior (AP) and superior-inferior (SI) X-radiographs were taken to confirm the position of the dipole within the skull. To assist this process, radio opaque markers were stuck using Araldite at defined points

on the skull. A Siemen's Orbix X-ray machine based on the Dulac system was used throughout. Absolute sizes were calculated by knowing the focal plane to object distance and the object to film distance. Geometric enlargement was confirmed by the markers on the skull. The position of the skull relative to the frame was the same for the X-ray study and the magnetic field study.

The dipole was energised as described previously. Seven different dipole locations, as shown in Figure 23, were investigated. As in the sphere experiments, data was taken along seven scan lines in a plane above the skull. In each case the measurement plane was chosen to be tangential to the skull at a point that minimised the dipole-scan plane distance, e.g for the dipole in the position corresponding to the motor cortex, the plane was tangential to the skull over the parietal region.

4.3 Results

Each set of data was analysed using the dipole in a homogeneous sphere model. For this, 49 data points with a spacing sufficient to encompass the significant signal region were used. The analysis was repeated for a large number of alternative sphere centre positions on a cubic grid. Table 5 shows the error in dipole parameter prediction for the dipoles shown in Figure 23. In each case the prediction is that obtained with the sphere centre in the position that gave the lowest value of R.

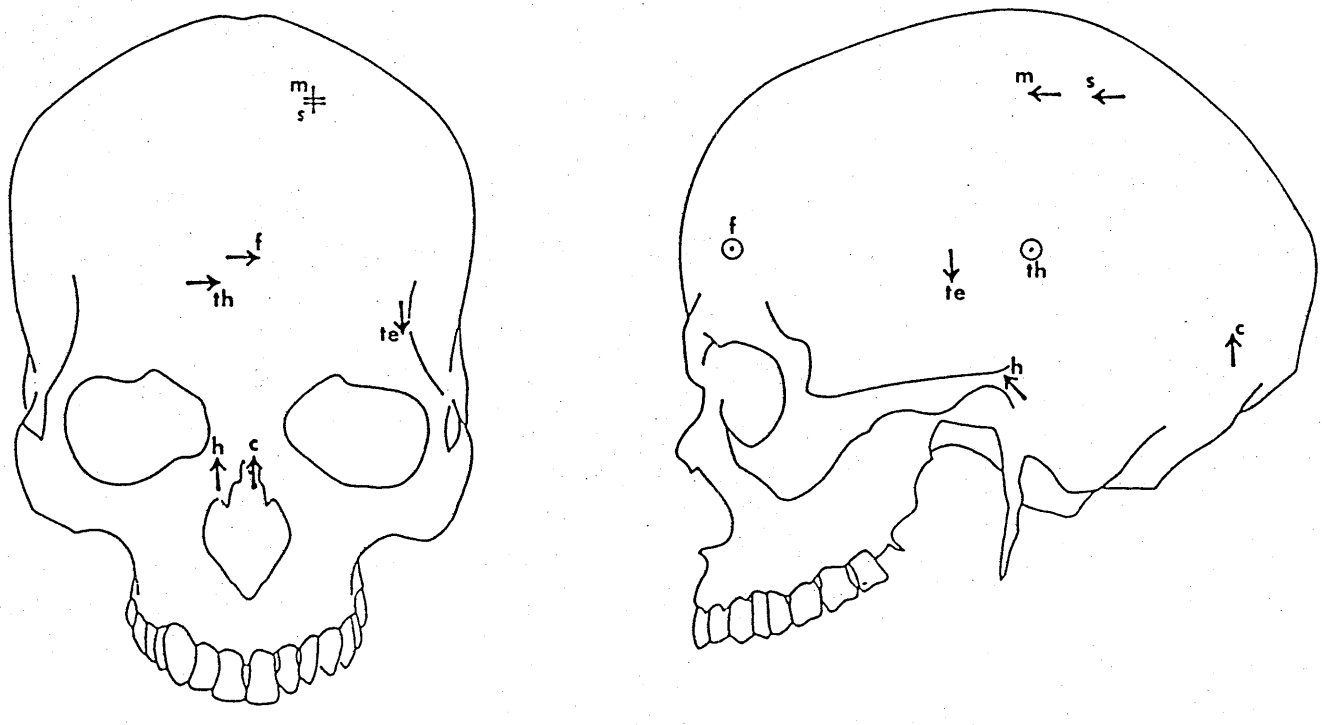

Figure 23 The dipole locations within the skull for the 7 examples studied. (m motor, s somatosensory, te temporal, f frontal, th thalamic, h hippocampal, c cerebellar)

Figures 24 and 25 compare the experimentally determined field contours with those predicted from the best fit dipole parameters. Accuracy of dipole parameter prediction varied with location. The individual dipole locations will now be discussed in turn.

Motor, somatosensory and cerebellum locations

The low R values for these dipoles indicates the quality of the fitting of the data and this is reflected in the accuracy of the localization. For the motor cortex and cerebellar dipoles, the error is largest in the depth coordinate (Z_D) with a compensating error in the dipole magnitude. This interplay of depth and magnitude is commonly observed. Because of the strong dependence of signal strength on depth (proportional to $1/r^3$ to first order), small depth errors can be coupled to large magnitude errors.

Estimated average uncertainties in the 'known' dipole parameters are 0.34 cm in each of the position coordinates (with the greatest error in Z_D), 38% in magnitude and 6.7° in orientation. It is clear that dipole localization by field measurement is accurate to an upper limit of $\simeq$ 5mm. The greatest uncertainty is in the dipole strength prediction.

Frontal

For this dipole the quality of the fitting (in terms of

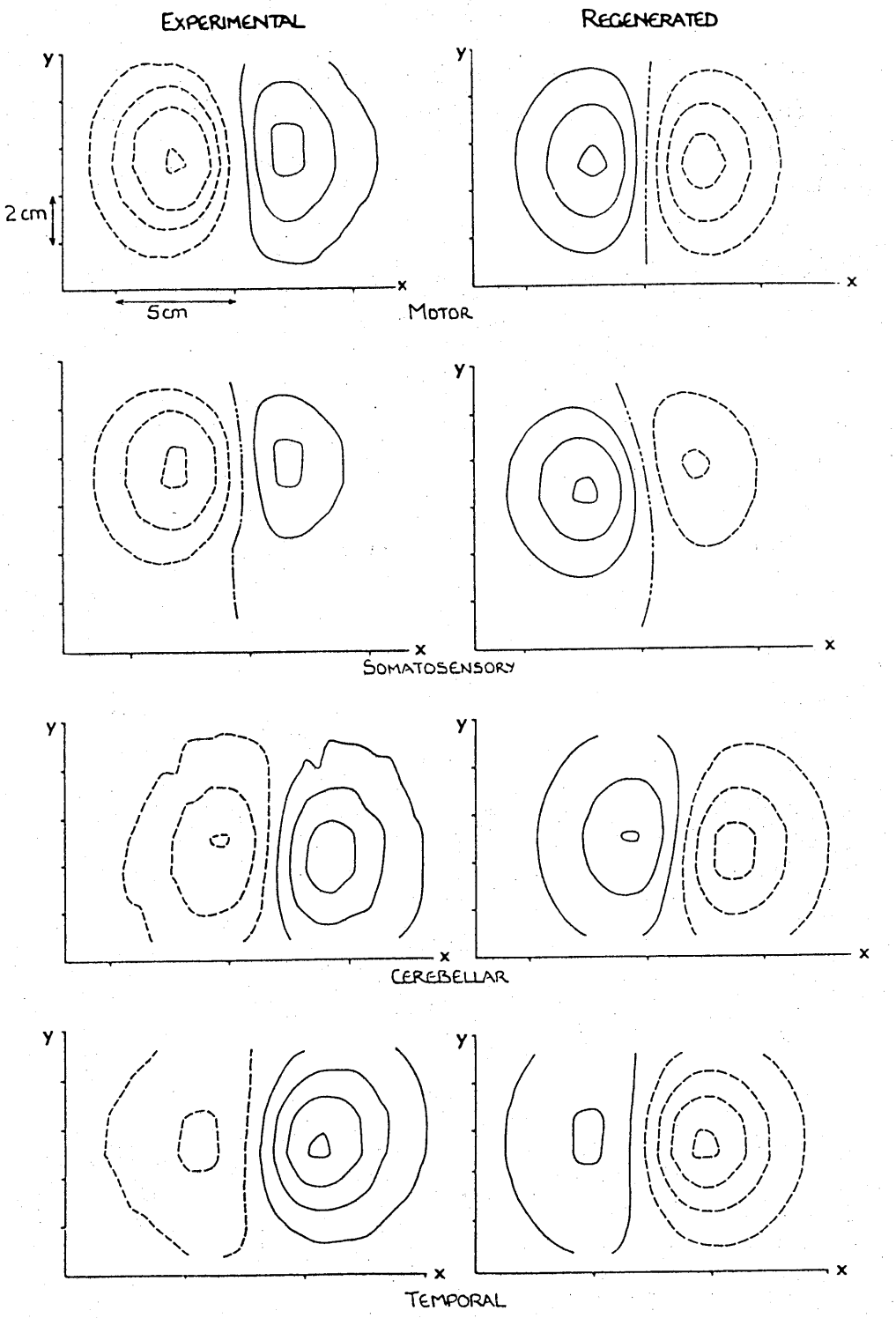

Figure 24 Contour diagrams for experimental and regenerated data for 'superficial' locations within the skull. Contours are at 4 pT. Dipole is now oriented at 270°. Solid lines (experimental) and dashed lines (regenerated) denote positive fields

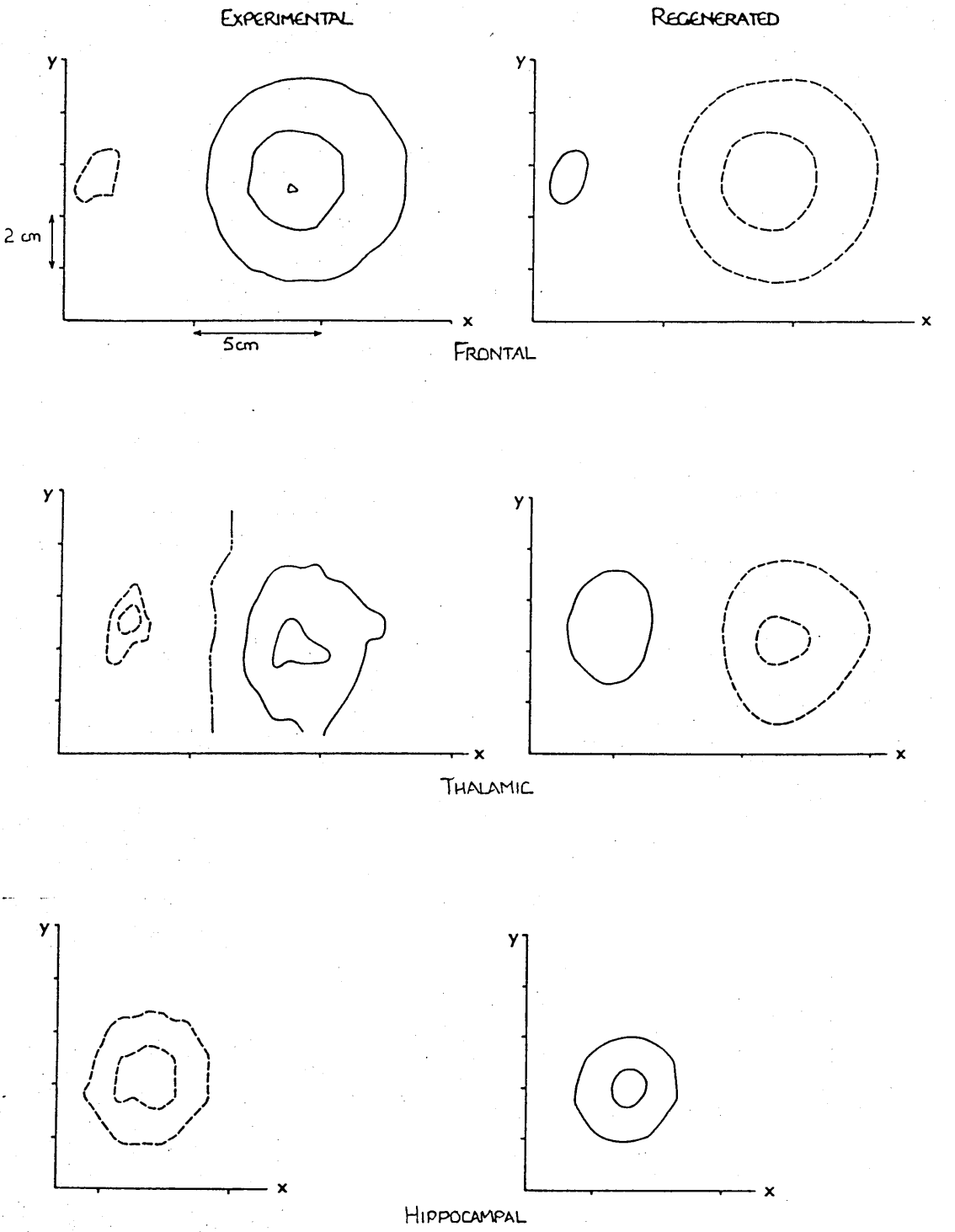

Figure 25 Contour diagrams for experimental and regenerated data for the deeper sources Solid lines (experimental) and dashed lines (regenerated) denote positive fields

the minimum achievable value of R) is degraded, although visual inspection of the fitted and measured contour diagrams would still indicate excellent agreement. The relatively large error in X_D is probably caused by the distortion from sphericality of the conducting volume by the frontal crest.

For the four dipole positions mentioned above, the minimum value of R occurred with the sphere centre chosen to be near the cranial centre. The dipole parameter predictions and the values of R were insensitive to small (± 2cm) shift in the position chosen for the sphere centre. For these dipoles, the sphere model appears robust and reliable.

Temporal

For this dipole, the lowest value of R was achieved with a conducting sphere centred at a position close to the cranial centre (at a depth of ≈7cm below the skull surface). The dipole location indicated by the algorithm is insensitive to small shifts in the assumed position of the sphere centre although the quality of the fit, as measured by the R value, deteriorates rapidly. However, if the sphere centre is placed at a more superficial position, the fitting is again of high quality (a low R value) and different predictions are obtained for the dipole parameters, which are now more sensitive to the assumed sphere centre. This suggests that the low R value

with the smaller radius sphere was somewhat fortuitous, reflecting current flow in the partially enclosed middle fossa region of the cranium.

Thalamus and Hippocampus

There were significant difficulties in fitting the data for these deeper dipoles. Reasonable fits can be obtained but the point of convergence in parameter space is sensitive to the sphere centre and to the iteration starting point. Similar values for R can be obtained with quite different sphere centre locations. For example, for the hippocampal dipole, an R value of 3.68×10^{-2} is obtained with a sphere centre shifted by over 8 cm from the position corresponding to the data in Table 5. The corresponding changes in dipole parameter predictions are $\Delta X_D \simeq 0.8$ cm, $\Delta Y_D \simeq 4.14$ cm, $\Delta Z_D \simeq 0.15$ cm, $\Delta P/P \simeq 21\%$ and $\Delta\alpha \simeq 175°$! The large changes in the predicted values for Y_D and P arise because the fields produced by a dipole close to the centre of the sphere are similar to those produced by an oppositely oriented dipole on the opposite side of the sphere centre. Although the lowest values for R for the dipoles located in the regions corresponding to the thalamus and the hippocampus gave reasonably accurate predictions for their parameters, there must still be considerable doubt as to whether, in an experiment on a live human brain, the weak differentiation between alternative solutions and the uncertainties arising from poor knowledge of the appropriate sphere centre would

allow similar accuracy of prediction from magnetic measurements alone.

It is interesting at this stage, to look at the effects the choice of model sphere centre has on dipole parameter prediction. Figures 26 and 27 show examples of contours of errors in somatosensory and thalamic dipole parameter prediction in sphere centre position space. In each case the variation in just one XZ plane is shown. The sphere centre position corresponding to the lowest R value is indicated by an asterisk. Regions of low error for each parameter can be seen but at differing sphere centre locations. The spacing of the contour lines indicates the relative sensitivity of a parameter to choice of sphere centre. We might expect that, if the model was appropriate, the sensitivity would be small.

Again, as for the dipoles 7 and 8 in a partially conducting sphere described in the last chapter, by taking an average of the 9 best fits (as indicated by low R values), it may be possible to obtain a better set of predictions. A location error $S = \sqrt{(\Delta X_D^2 + \Delta Y_D^2 + \Delta Z_D^2)}$ can be defined to encompass the three location parameters. Table 6 compares S and R values from the best fit and the averaged best fits for all the dipole locations.

Table 5

Moduli of differences between the experimental and predicted dipole parameters using the lowest R value.

Location	ΔX_D/cm	ΔY_D/cm	ΔZ_D/cm	$\Delta P/P$	$\Delta\alpha$/°	R/E-2
Motor	0.10	0.36	0.55	68%	2	0.23
Somatosensory	0.29	0.25	0.46	12%	20	0.08
Cerebellum	0.18	0.35	0.53	36%	8	0.48
Frontal	0.78	0.17	0.47	12%	6	1.75
Temporal	0.24	0.04	0.08	19%	9	0.29
Thalamus	0.60	0.39	0.67	45%	4	2.69
Hippocampus	0.15	2.29	0.89	48%	75	3.24

Table 6

Comparison of averaged and lowest R value with dipole location accuracy

Location	Lowest R		Averaged	
	R/E-2	S/cm	R/E-2	S/cm
Motor	0.23	0.66	0.48	0.29
Somatosensory	0.08	0.60	0.44	0.17
Cerebellum	0.48	0.66	0.58	0.54
Frontal	1.75	0.93	1.87	0.59
Temporal	0.29	0.26	0.57	0.24
Thalamus	2.69	0.98	2.94	0.79
Hippocampus	3.24	2.46	3.85	0.85

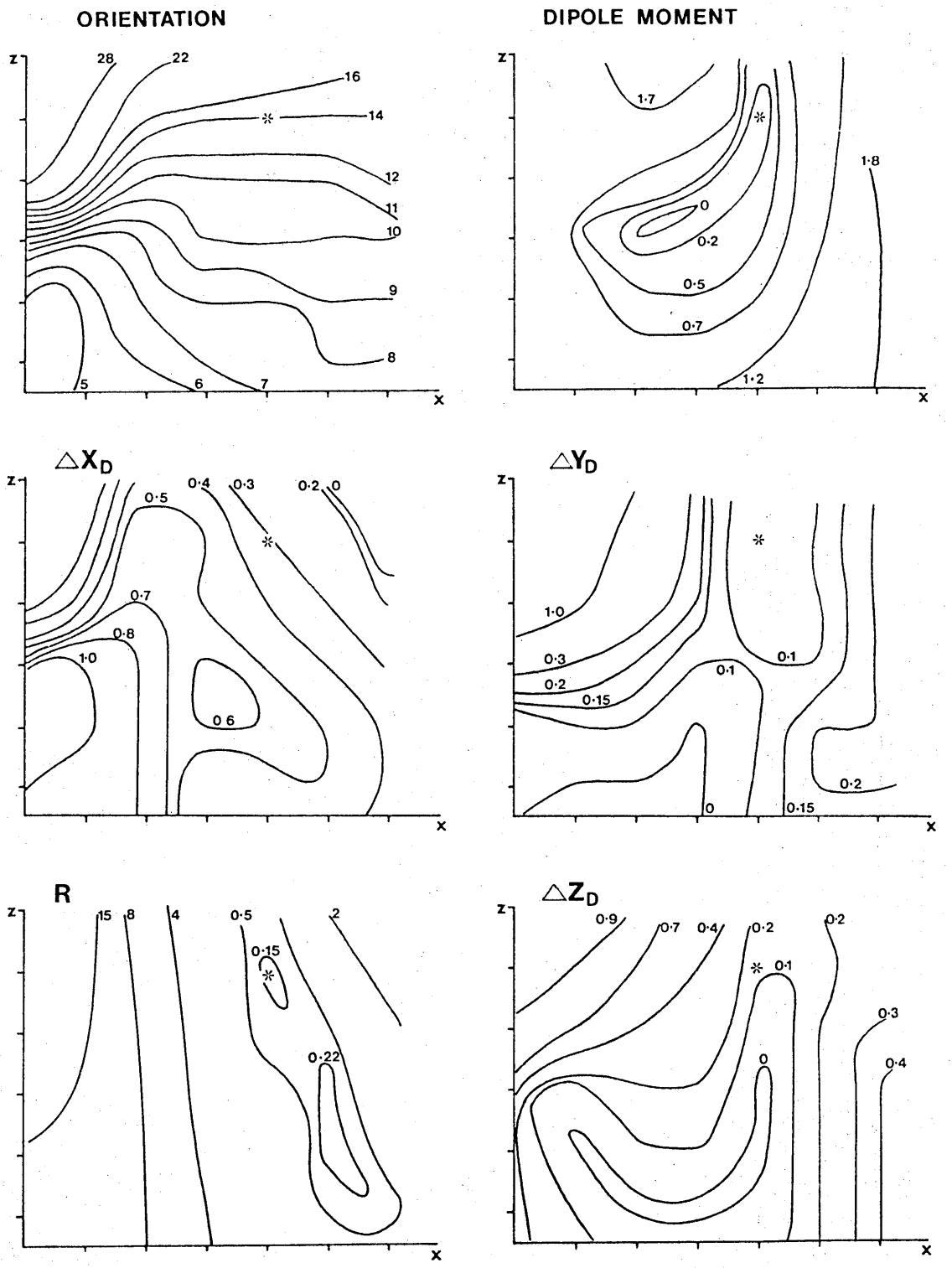

Figure 26 Variation of residual errors in dipole parameters as a function of model sphere centre space (in one xz plane) for the dipole located in the somatosensory region

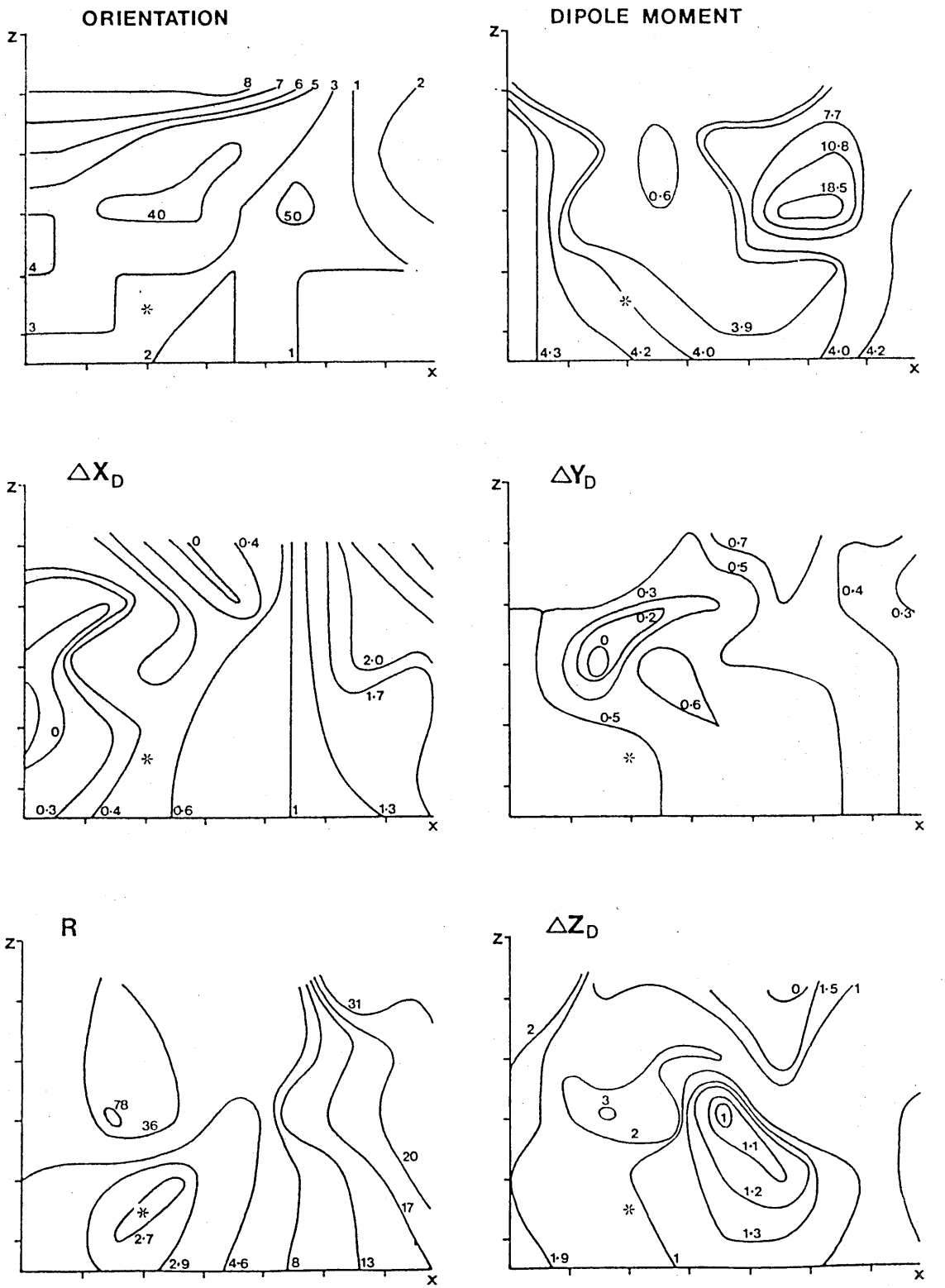

Figure 27 Residual dipole parameter errors as a function of model sphere centre space for the thalamic region

For the deeper sources, the values of R and the dipole predictions are significantly worse than for the superficial ones. One possible cause might be an apparently worse noise to signal ratio for the data obtained from these dipole locations. Seven data points (separated by 1.5 cm) within the noise region (i.e where the signal was negligible) for each of the scan line (49 points in all) were squared and summed to obtain a noise power. Similarly a signal power was also obtained. The ratio of the noise power to the signal power can be defined as R_{noise}. For the motor cortex this ratio was 1×10^{-2} and for the thalamic dipole this ratio increased to 4×10^{-2}. For the hippocampal dipole, the ratio was 4×10^{-2}. These ratios are similar to the R value defined for the analysis program. These figures suggest that, with optimum sphere centre position, the residual error is dominated by noise rather than systematic misfit. However, computer simulations (Swithenby - private communication) show that the dipole predictions would not be expected to be significantly degraded by the noise levels in these experiments.

4.4 Final Remarks

In Chapter 3 the magnetic fields arising from a dipole within a spherical geometry were successfully modelled using a dipole in a sphere model. Simple but significant deviations from the spherical shape were successfully dealt with. In this section the difficulties that might arise when the spherical geometry is replaced by a skull-like geometry were explored. Again the dipole in a sphere model was utilised. Although the 7 examples studied do not constitute a full survey, they do illustrate some central problems for MEG analysis in general and homogeneous sphere based modelling in particular.

The most important cautionary point to emerge from our study is that analysis based on a homogenous symmetric sphere model with the sphere centre at the 'cranial centre' is of dubious validity, for deep sources at least. Somewhat more robust predictions may be obtainable by including the three parameters describing the model sphere centre in the fitting procedure and examining closely the quality of fit as a function of sphere centre position. This will yield a range of alternative solutions. These alternatives hopefully can be reduced in number by knowledge of the anatomy and physiology of the cranial region concerned. In addition EEG data may be extremely useful in comparing the various solutions. On the other hand, in real experiments the quality of the data will be low for deep sources as the fields will be weak.

Superficial dipoles were easier to locate accurately than the deeper ones where problems of poor convergence are exacerbated. However, apparently good fits, corresponding to about 20% average error in signal value, can yield quite spurious localisations. Such problems can be avoided by averaging over several good fits. For superficial sources (e.g motor and somatosensory cortex), it may be possible to avoid the necessity to assume a model sphere centre by scanning through model sphere centre space. In contrast, for deeper sources local boundaries may necessitate model sphere centres quite different from the cranial centre.

Quantitative assessments of the accuracy of fitting, together with its relation to noise, must form part of the report of any analysis. Without such indication of the 'quality of fit' there is no means of assessing whether dipole identification might be false. It should also be noted that the dipole is only identified reliably if a full search of parameter space indicates no other solution of similar quality.

This study indicates that the robustness of the model to its assumptions must be investigated in any more sophisticated model subsequently developed. There is little point in adding complexity if the added parameters are irrelevant to the prediction (ie sphere centre

location). On the other hand, if there is strong parameter dependence then the choice of that parameter needs to be carefully justified.

CHICK EGG

5.1 Introduction

In this chapter, experiments that exploited the dc capabilities of our SQUID magnetometer are described. They were made on the developing chick embryo, which in its early stages may be modellable in terms of a region of electrical activity enclosed within a spherical conductor. One aim of the experiments was to gain experience of the dipole in a sphere model with an easily accessible animal. The other was to understand more fully the scantily researched dc electrophysiology of one of the most extensively studied developmental systems.

The fertilized chick egg is a highly organised system with all the attributes essential for normal development. During development, with the aid of external heat and oxygen from the atmosphere, the inert substances available in the egg are converted into the living tissues of the chick. Since there is a close metabolic interdependence between the embryo and the various structures of the egg, a full understanding of the development requires investigation of all processes, physical as well as chemical in the egg. One such physical process is ionic current flow.

Electrophysiologists have measured quasi dc electrical activity at the definite primitive streak stage (15-20 hours after incubation) of a chick embryo (Jaffe and Stern

1979). This will be discussed later. Previous work in our laboratory (Lennard 1984) has shown the presence of a magnetic field which varies slowly in time (from a few hours to a day) and is first detectable from the developing egg some 20-27 hours after incubation.

At early stages of development, the embryo is a localised structure that floats on top of the yolk which in turn floats in the large ellipsoidal conducting egg. The embryo may act as an effective dipole and may thus provide an easily modelled current source. It was thought that a better understanding of the embryo development might follow by characterising the dipole source using non - invasive field measurements and then correlating these observations with those from more invasive experiments on other eggs. For example, the technique of shell windowing enables inspection of the embryo position relative to the extra embryonic components of the egg. Embryo removal, membrane dissection and selective inhibition of possible membrane pumps could help to determine the exact signal location.

Before discussing these experiments in detail, it is essential briefly to review basic embryology and also electrophysiological work relating to chemical fluxes. Development changes can then be related to the ionic currents.

5.2 Embryology

In this section I will concentrate on the early stages after the start of incubation. After describing the development of the embryo itself, I will go on to discuss the extra-embryonic membranes which develop concurrently with the embryo and provide it with protection, nutrition and respiration.

Egg development prior to laying, but after fertilisation and cleavage, includes the development of the germ wall and entoderm (Bodemer 1970). The formation of the germ layers has begun. The stage of development at laying is fairly consistent from egg to egg although not absolutely constant. Only a whitish disk, (3-4 mm diameter), known as the blastoderm, is usually present at this stage. When the egg cools after laying, development ceases but it is renewed when the temperature is raised to the required degree by incubation.

At the time of laying, the shell consists of minute crystals of calcium carbonate and is lined by two membranes which separate out at the caudal (blunt) end to form the air sac (Figure 28). These membranes surround the albumen, which contains proteins, carbohydrates, a trace of fats, minerals, vitamins and is the main reservoir of water. The albumen is inhomogeneous. A dense layer of albumen around the yolk is prolonged, in the form of two spirally coiled opalescent cords (chalazae) towards the

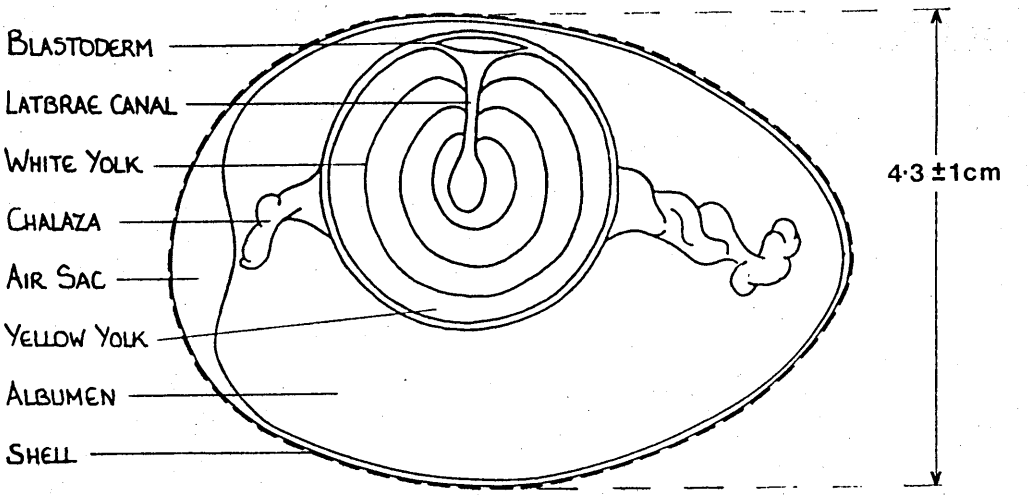

Figure 28 Cross section of the chick egg at time of laying

ends of the egg. These restrict violent movement of the yolk which contains lipids, proteins, carbohydrates, electrolyte and vitamins. The yolk absorbs water from the albumen (increasing the density of the latter). The relatively high fat content (33%) of the yolk (Romanoff 1960) means that it tends to float to the upper surface of the egg and can therefore be approximately located within the intact egg. Because the yolk floats, the embryo (on top of the yolk) comes into contact with the shell membrane and will stick to it if the egg is not turned several times a day to move the yolk within the shell.

In the course of development, the embryo and the extra embryonic membranes arise from the blastoderm. Gastrulation, a process involving migration of cells followed by segregation and delamination, is the first stage of development. The delamination process leads to the formation of the lower hypoblast layer and the upper epiblast layer of cells (Figure 29). The peripheral zone of the blastoderm is an opaque single layered sheet (the area opaca) which later gives rise to the extra embryonic membranes. The central translucent part of the blastoderm (area pellucida) will form the embryo itself.

Movement of cells within the blastoderm leads to the formation of the primitive streak, through which cells migrate to form mesodermal tissue between the two layers (Figure 29b). On average the axis of the primitive streak

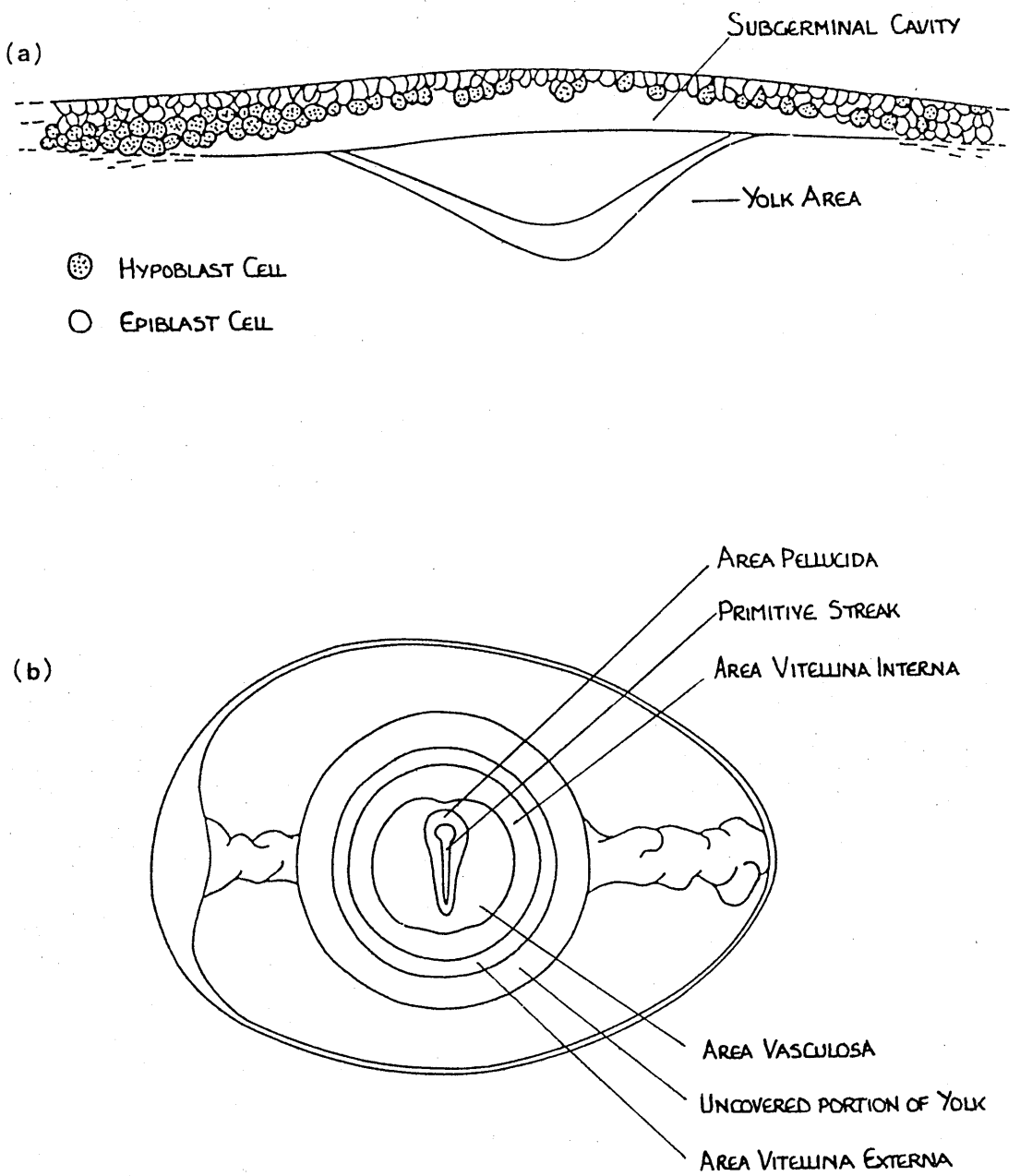

Figure 29 Division of the blastoderm into a.) different layers (shown in cross section at time of laying) and b.) into different regions (viewed from above at ≈ 26 hours after incubation)

is at right angles to the long axis of the egg (Hamilton 1952), although there is variation in the angle (over 25% of the streaks deviate by as much as 45°). Cell division, growth and migration lead to mesoderm formation at eighteen hours after incubation commenced.

From ~ 20 hours, various body folds begin to develop starting with the head fold. Meanwhile, the mesoderm becomes organized into blocks called somites. The number of somites correlates sufficiently closely with the other aspects of development that the stage can be identified by a somite count. Neural folds leading to the formation of the neural tube and brain occur at 24 hours (3 somite stage). At 29 - 37 hours (10 somite stage), the brain is well formed while the heart and blood islands are appearing. The blood islands form within a circle around the embryo and are part of the extra embryonic system described later. The cells on the periphery of these islands join to form the endothelium of the future blood vessels whilst the central ones become corpuscles. Adjacent blood vessels establish contact between themselves and the whole system is gradually transformed into a very irregular network. The network of the area vasculosa (as the region of this network is termed) develops into the area pellucida and eventually establishes connection with the embryo proper at the heart.

By the 13 somite stage (≃ 36) hours, the heart is functioning with blood circulating through a network overlaying the yolk and the brain is a convoluted structure. Head flexures start at the 17 somite stage and the primitive streak begins to be utilized for the tail material at 20 somites (≃40 hours). The lens of the eye is beginning to form at this stage. By the 35 somite stage (≃72 hours) the embryo resembles a young chick.

Thus far I have concentrated on the embryo development. However, the development of the embryo is accompanied by development of the extra embryonic membranes (Figure 30). These are semi autonomous, living structures derived from the blastoderm and continuous with the tissues of the embryonic body.

The amnion, a fluid filled cavity which protects the embryo from dessication, concussion and adhesion to the shell or friction from it (Balinsky 1975, Bodemer 1970) begins to form at 20-25 hours. It slowly envelops the embryo from both the head and tail uniting into a complete structure at 72 hours (36 somites).

Another extra embryonic membrane, the allantois, emerges from the endodermal hindgut as a urinary bladder (Grove and Newell 1974) at the 30 somite stage (50-55 hours). A network of blood vessels develops on the external surface enabling the allantois to supply oxygen to the embryo.

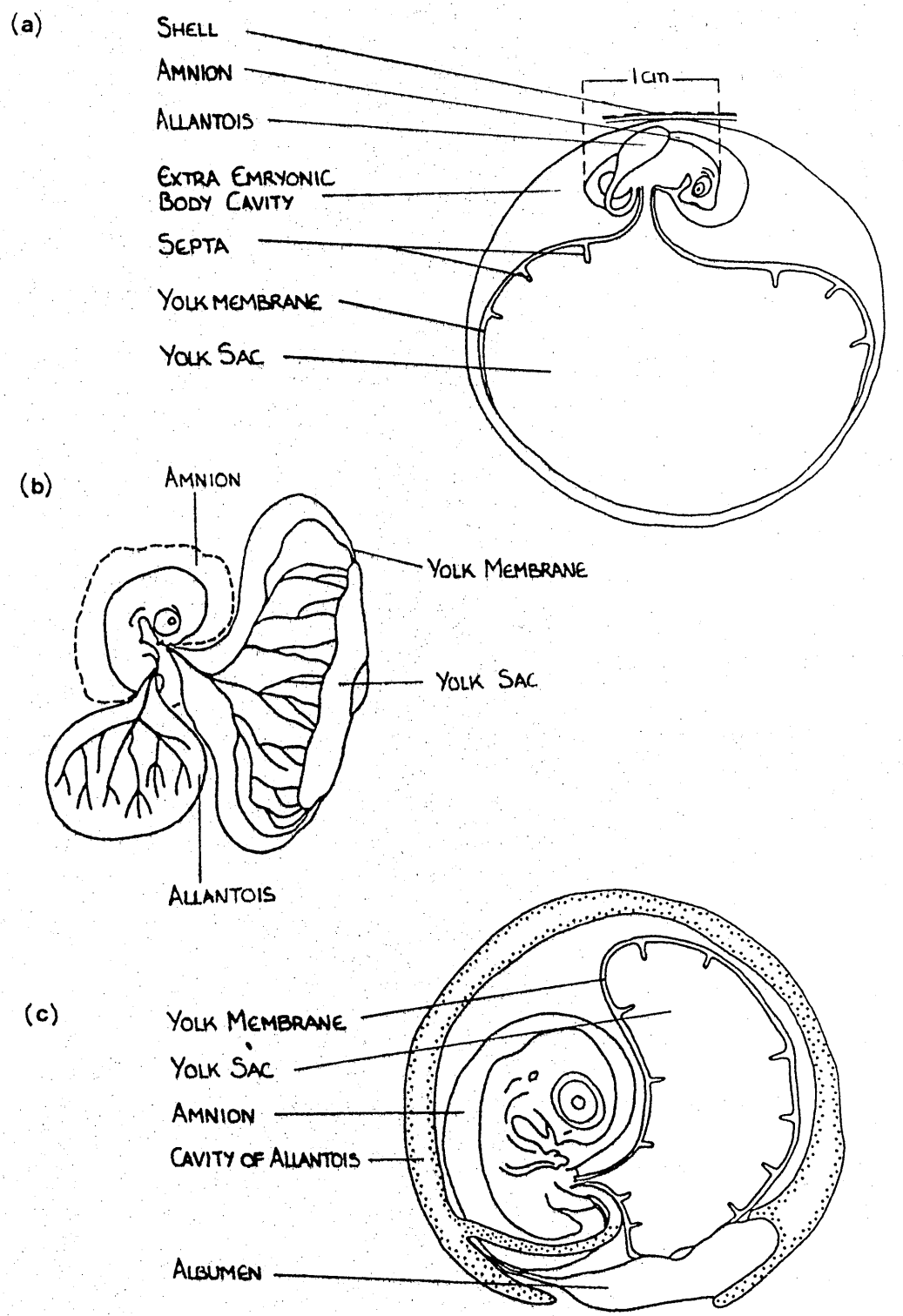

Figure 30 Extra embryonic membrane development at a) 4 days, b) 7 days and c) 9 days after incubation

The third membrane is that surrounding the yolk. This yolk sac membrane is formed from the extra embryonic splanchnopleure and is permanently united to the intestine of the embryo by the yolk stalk. Yolk does not, however, pass through the stalk into the intestine. The yolk membrane is an important extra embryonic structure because of its role in transporting nutrients to the embryo. I will describe some features relating to its function in detail.

The yolk sac membrane spreads over half of the surface of the yolk in the first four days and then continues to spread, but more slowly, over the rest of the yolk (except for a small region at the base) by the seventh day (Figure 30). During the period of spreading, it consists of a medial vascularized region (known as the area vasculosa) and a peripheral non vascular region (the area vitellina), which is conveniently separated into two regions, the area vitellina interna and the area vitellina externa.

The area vitellina represents the zone of extension of the membrane where entodermal cells are dispersed among spheres of yolk. Yolk granules are ingested by young entodermal cells while their activity is at low level. As the cells increase their activity, they liberate enzymes into the yolk and digestion becomes extracellular, hence the absence of yolk granules in the entoderm of the

vascular area.

With the peripheral margin of the area vitellina externa acting as the leading edge, the yolk sac progresses over the yolk, passing the equator by the third or fourth day of incubation. As the yolk sac membrane grows, the area vasculosa also increases in size, invading the regions that previously were area vitellina. As a result the latter eventually disappears completely.

During the third to fifth day the area vitellina extends at the rate of 2.6 to 2.8 mm per day. Its surface continues to increase until the sixth day. Not all the expansion of area is due to growth however; the influx of water from the albumen to the yolk causes the latter almost to double in volume during the same period.

Except for regions derived from the area pellucida, the yolk sac membrane is lined with glandular and absorbing epithelia which digest and absorb the yolk, passing the products to the vitelline circulation. The yolk sac is thick, opaque and covered on its inner surface with extensive villi-like projections and corrugations running in a generally meridional direction following the main arterial directions and containing a multitude of blood vessels and capillaries. The system is most complex at the equator. The yolk sac does not reach full development until the end of incubation (21 days) when the villi like

projections almost touch the opposite walls.

The above description indicates that the extra embryonic membranes are responsible for much of the development of the embryo. The membranes control the inner environment of the egg. Some aspects of their electrophysiology, in the context of briefly reviewing other studies, are highlighted in the next section.

5.3 Electrophysiology Of The Egg

Embryological epithelia have been shown to support potential differences between their two surfaces of ≈3-15 mV (Jaffe and Nucitelli 1977). The epiblast usually has a potential difference of 15 mV across the sheet. The cells rest on a basal lamina on the positive or internal side (Figure 29a). It has been shown (Stern and Mackenzie 1982), that sodium pumps are initially more densely distributed on the internally facing membrane, throughout the zona pellucida. However, just before primitive streak formation, sodium pumps become more numerous on the outer facing cell membranes in the region where the primitive streak will form. Jaffe and Stern (1979) have measured the electrical field around the growing chick embryo *in vitro*. They reported steady currents (≈100 $\mu A\ cm^{-2}$) at the time of primitive streak formation (16 -20 hours of incubation). However, this current is first detectable a few hours before physical formation of the streak. The current left the primitive streak and returned through the

epiblast elsewhere on the sheet. This current may be related to the redistribution of the membrane pumps and hence to the formation of the streak. This provides an example of a developmental current.

As for the role of these currents, it is postulated that early in development ion currents help establish so-called positional values. These positional values are established or re-established by highly localised mechanisms akin to crystallization. However, these regions have to grow. This growth is initiated by ion leaks through sites of discontinuity in positional value (for example at limb bud sites - Jaffe 1981).

Bennet and Trinkaus (1970) reported electrical coupling of epithelial cells by means of extracellular space narrowing and by the formation of specialized junctions in the embryos of Fundulus. The coupling is used to transmit ions and small molecules between cells that are responsible for the coordination of growth and differentiation.

An important property of the yolk sac membrane is high resistance which may serve as a barrier. In addition, this membrane generates a resting potential which is small at fertilization but increases with time. The gradual increase may be due to the development of semipermeability of the membrane and to a redistribution of ion pumps (Bennet and Trinkaus 1970).

The yolk and chorioallantoic (CA) membranes have important water and electrolyte transport functions (Coleman and Terepka 1972). During development, the water available to the embryo comes from either liquid reserves within the egg or from metabolic end products. Water is transported from one compartment to another. Active processes are involved because the three major water compartments (subgerminal cavity, amnion and allantois) are not in ionic or osmotic eqilibrium (Simkiss 1980).

Active transport is not limited to water fluxes. For example calcium ions are transferred from the egg shell into the circulation of the embryo and chloride ions are reabsorbed from the allantois. All these processes involve currents in some form.

From the above remarks it is clear that development may be expected to be accompanied by currents. Given the macroscopic nature of the epithelia and the dramatic changes taking place in terms of compartmentalization and biochemical fluxes it would be unsurprising if such currents were sufficiently unbalanced as to give detectable external fields. However, the extent to which the currents, as physiological entities, control the development is not addressed in this thesis. Our main intention is to explore the extent to which the field measurements can characterize the dc electrophysiology and

hence contribute to the overall understanding of the phenomena.

5.4 Recording The Magnetic Fields

Fertilized eggs (Gallus domesticus) were obtained from a commercial hatchery and incubated at 38°C and 65% humidity in a suitably modified incubator which allowed an egg to be removed and replaced without any disruption to the remaining eggs. For each measurement, the egg at the appropriate incubation period was placed on a non magnetic support with its caudal end pointing along the Y axis and scanned, in zero field (Lennard 1984), in a manner similar to that described for the sphere work. The platform was moved parallel to the X axis along equally spaced (usually 1.4 cm separation) scan lines. The distance of closest approach to the pick up coil was ≈14 mm. SQUID output was averaged over 5 mm intervals and the signal was visually inspected for artefacts after all the scans had been obtained but before averaging the data for each scan.

It was important not to allow the egg to cool to below ≈18°C as initial experiments had indicated cooling of the egg affected the signal amplitude. This was quantified by placing 4 developing eggs in a refrigerator. After one hour, these eggs were reincubated. Figure 31 shows the field signal against time for one egg as an example. Similar results were obtained for all these eggs.

During the typical scanning period necessary for a full field contour plot (≈ 3 minutes with a further 3 minutes for checking the data), the change in observed signal due

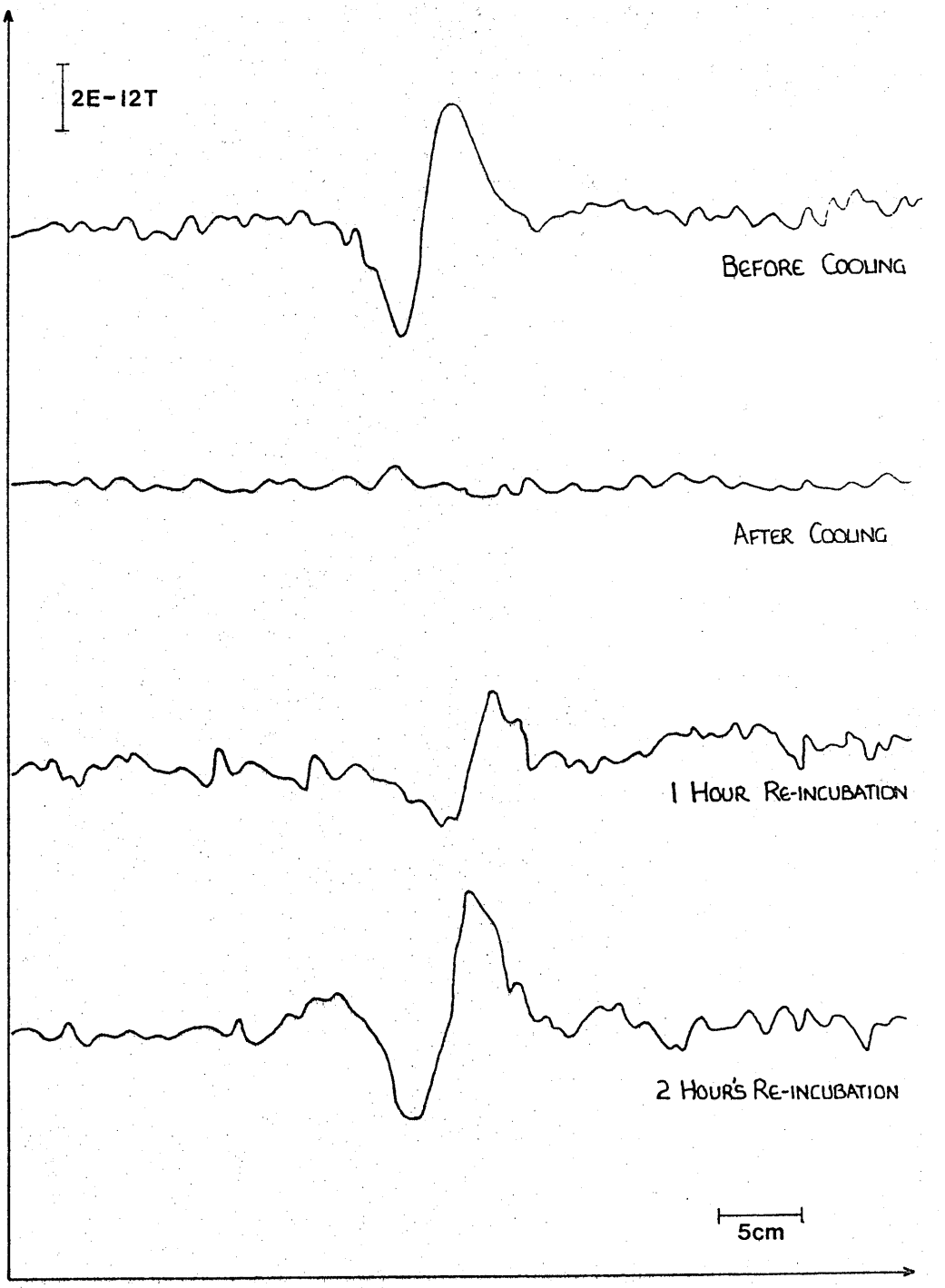

Figure 31 Effect of cooling on a developing chick egg. For each trace a single scan along the X axis was made across the centre of the egg

to cooling is insignificant, although the signals do fall significantly if the egg is left out of the incubator for ≈30 minutes.

In total 12 series of experiments were carried out. Each involved incubating up to 18 eggs at one time. Of these 6 were used in characterizing the signal and the remainder used to check on development throughout the experiment. A large number of fertilized eggs (up to 25% in a commercial hatchery) stop developing at some time before hatching. Sufficient numbers of eggs had to be incubated to allow for this wastage. Several series were used to establish broad patterns of behaviour and an efficient protocol. The data below therefore represent only a small part of the total experimentation.

Series H, J, K and L were used to characterize the range of signals obtainable in ovo and to relate them to physiological development. The eggs were scanned at approximately 6 hourly intervals for the first 5 days. In addition, for series H, eggs were scanned twice daily until the end of incubation.

In the invasive experiments reported later, a total of 14 eggs were used for the dissection experiments and another 27 eggs for the various metabolic inhibitor experiments. These experiments were carried out at ≈72 hours after incubation.

5.5 Results - in ovo

Typically the magnetic field signals became clearly visible above the noise (≈200 fT rms using a 0.33-40 Hz bandwidth) at an incubation time t ≈22 hours and then grew reaching peak to peak values in the range 4 pT to 40 pT at t ≈70 hours (Figure 32). The separation of the field extrema on the contour diagrams (indicating the depth of the effective signal source) was in the range 30 mm to 40 mm during this time (Figure 33). Thereafter, for each egg, the signal fluctuated slowly in strength and pattern but remained present throughout incubation. There was considerable inter-egg variability in signal magnitude which was not related to the size of the egg.

The field pattern before ≈65 hours was approximately bipolar (Figure 34) with positive and negative z-components of the field on each side of the null line that lay most often along the long axis of the egg. The orientation of this pattern in the XY plane has been parameterized by measuring the angle Φ between the X axis and the line from the minimum to the maximum field points (Figure 35). It can be seen that the bipolar pattern is usually oriented in the range $-45° \leq \Phi \leq 45°$ until t≃ 65 hours, after which time the orientation appears random. At this time the observed field pattern from each egg changed dramatically in both magnitude and form over a few hours.

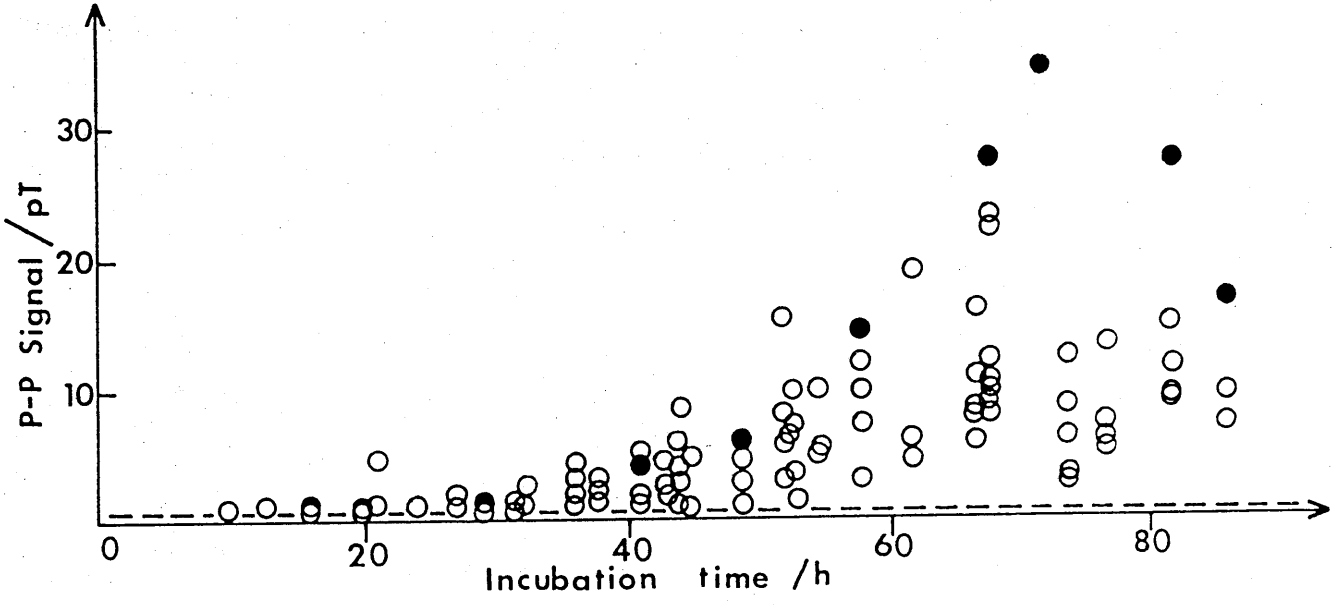

Figure 32 Peak to Peak field signal amplitude over the first three days Broken line indicates noise level. Filled circles indicate the amplitude of one egg. Other eggs showed similar changes

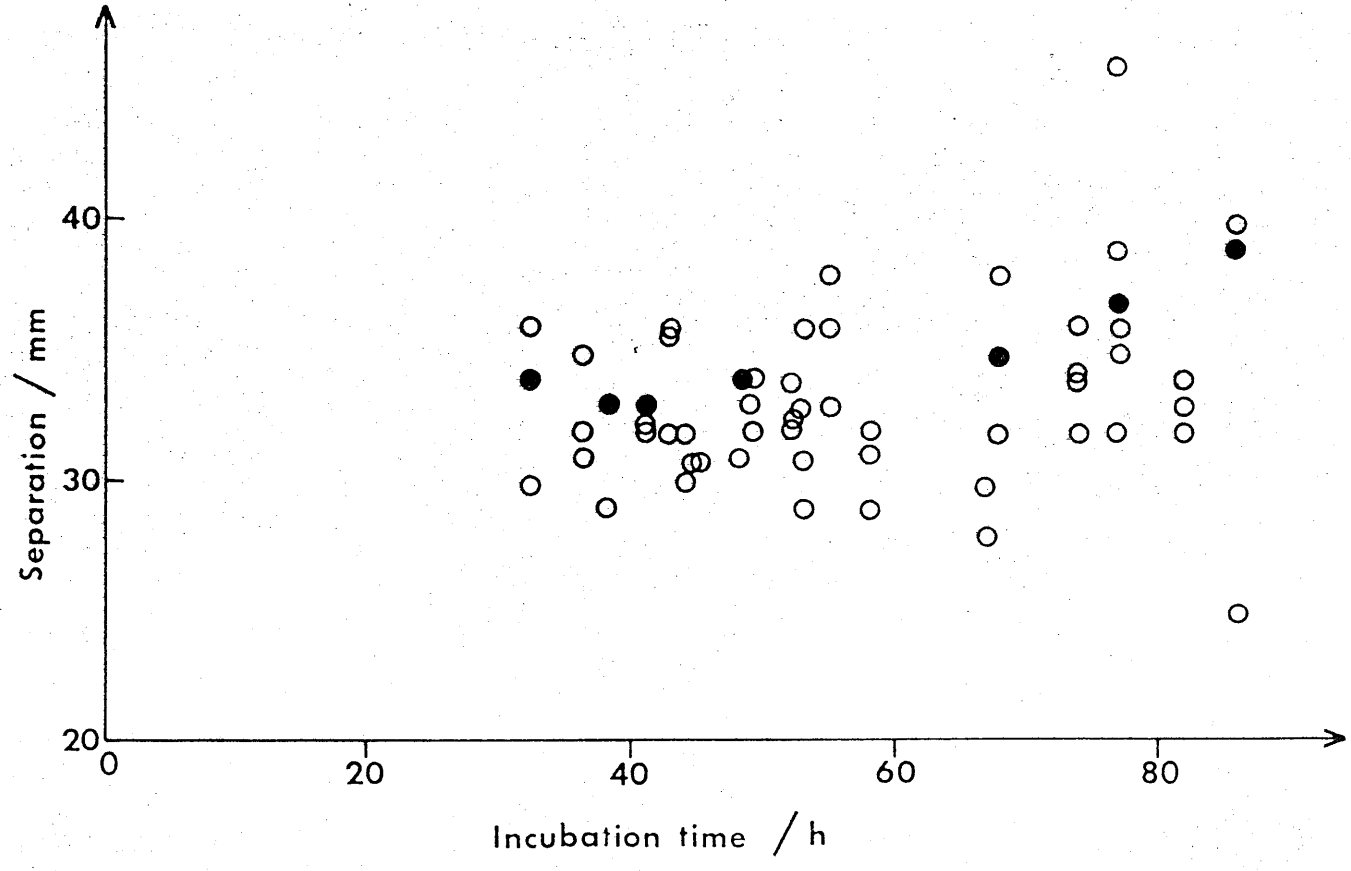

Figure 33 Separation of field extrema over the first three days. Filled circles indicate separations for one egg. Other eggs showed similar changes

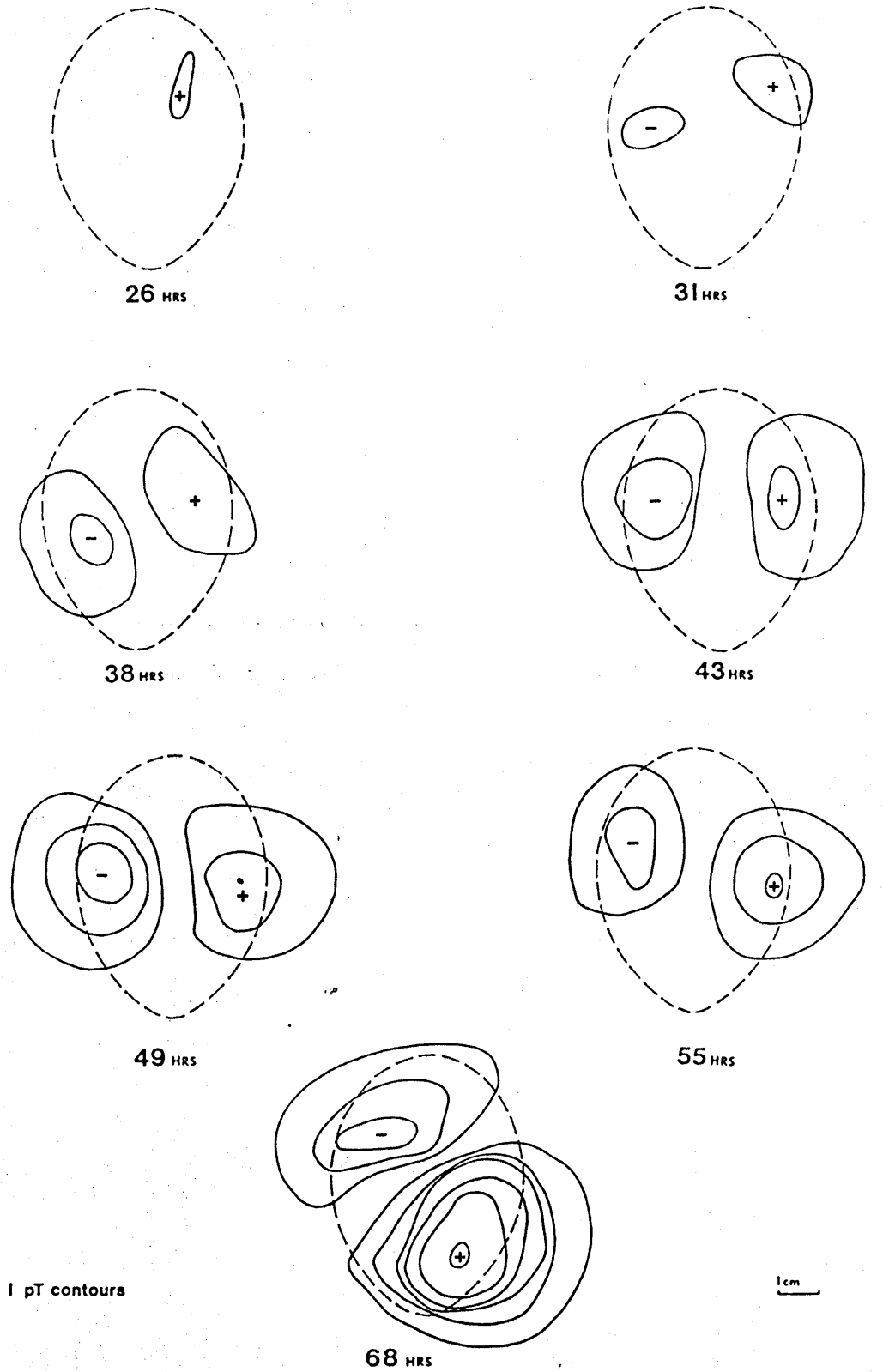

Figure 34 Typical variation of signal with development time. The zero field contour is not shown. (Series L egg 1)

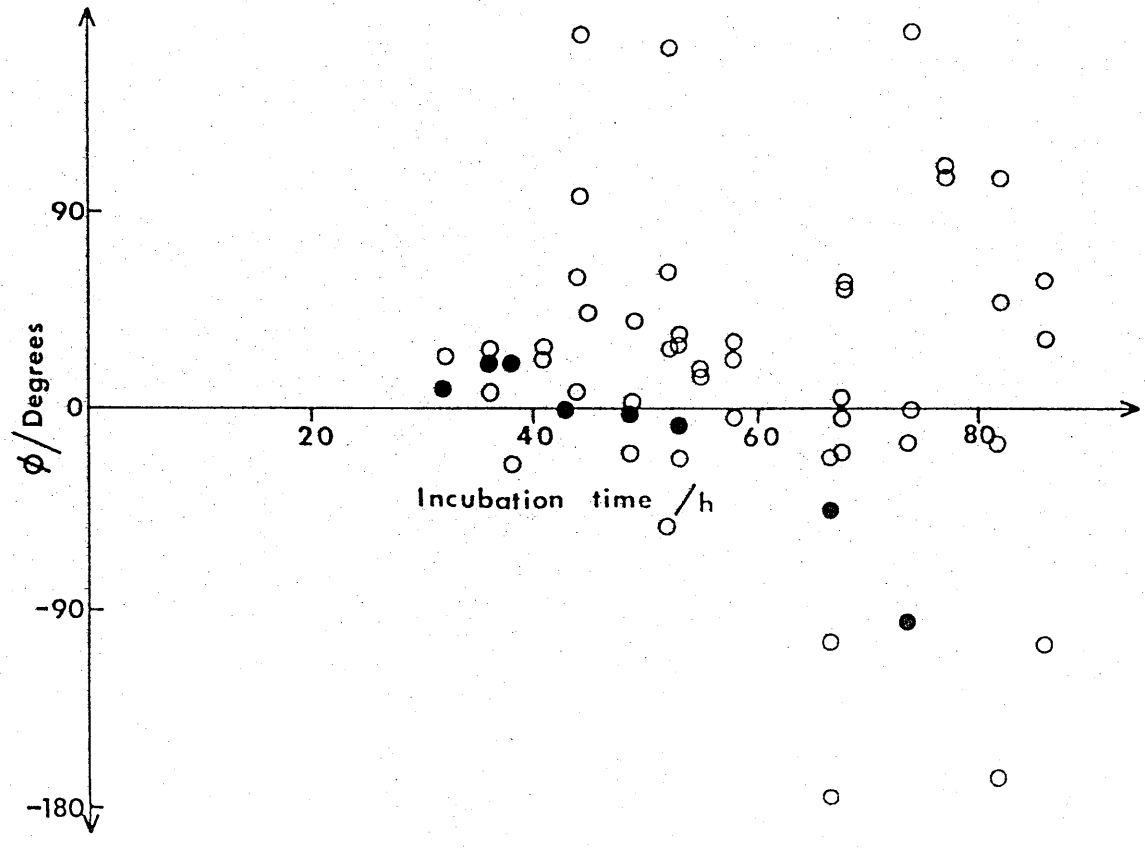

Figure 35 Orientation of the magnetic field pattern. The angle between the line joining the field extrema and the X axis as a function of development time Filled circles indicate results for one egg. Other eggs showed similar changes

Additional experiments were carried out to exclude artefactual sources of signal in these in ovo studies. Empty shells gave no signal, whereas embryos transferred intact with the yolk and extra-embryonic membranes to a dish still produced fields. Exposing 19 eggs to dc fields of ≈0.05 T did not change the field signals in 17 cases. In the remaining 2 eggs, washing the shell with saline to remove surface contamination reduced the magnetization effect. Clearly ferromagnetic contamination is not the signal source from within the egg.

5.6 Determining The Source Location

Windowed Egg Experiments

Thus far the results have been shown to indicate that the signals have a physiological origin and that significant changes take place during development of the embryo. In order to be certain of the relationship between signals and both the extent of development and the orientation of the embryo with respect to the egg, it was necessary to look inside the opaque shell without disturbing the developing system. This was achieved by windowing, a technique whereby a small section of the egg shell is scored with a blade and lifted off the egg without touching the underlying embryo. At the early stages of development, the fatty yolk floats on the albumen with the embryo itself on top of the yolk actually in contact with the shell membranes. These shell membranes have to be removed as they too are opaque. The air sac (≈ 1 cm^3) at

the caudal end is formed by the separation of the two shell membranes and, upon their rupture, collapses. The egg contents fill the air space. In order to maintain the same relative geometry in the windowed egg as in the intact egg, some physiological saline is added. For the developing chick egg this consisted of 0.9% sodium chloride with traces of potasium and calcium.

The greatest risk to a windowed egg is air-borne bacterial infection. The albumen contains avidins (physiological bacteriocides) but, for further protection, a covering of cling film was placed over the window. This covering also reduced fluid loss from the egg (in some situations it was necessary to apply liquid paraffin onto the embryo to prevent excessive loss of fluid). Problems can arise from air-borne contaminants settling on the film. These can be eliminated by removing the film and washing the egg with physiological saline prior to scanning under the magnetometer.

The results of the windowing (Table 7) indicate that the orientation of the embryo with respect to the poles of the egg is uncorrelated with the orientation of the maximum and minimum magnetic field signal shown in Figures 34 and 35. Windowing also enabled a more accurate staging of the development of individual eggs by either counting the number of somites present or by looking for certain features (for example presence of a lens in the eye).

Table 7

Orientation of the embryo capital caudal axis and the field contour null line, both with respect to the X axis. All 6 eggs had 3 days of incubation but windowing revealed difference in development

Egg	Embryo angle/° (± 5°)	Φ/° (± 1°)
1	5	2
2	-85	45
3	90	-20
4	45	-110
5	-30	-94
6	100	-173

Modelling

In order to determine the source location we need to invoke a model. If the dipole in an infinite half space model is used (as a first approximation), separation of the signal extrema is related to the depth of the source by the simple expression of Equation 14. The separation of these extrema is essentially independent of incubation time (from 30 to 70 hours) as shown in Figure 33. The average separation of 33.5 ± 1.5 mm, would require a single dipole source to be located at 7 ± 3 mm from the centre of the egg. The average signal magnitude would correspond to a strength of 25 μAcm. This simple calculation does not take the coil set or conducting geometries into consideration. The finite size of the coil set will lead to smearing of the signal resulting in a lower signal amplitude at the extrema which would also be at a different separation.

A fuller analysis involving integration over the coil set, and the use of the full data set, was carried out using the dipole in a sphere model and the analysis program discussed earlier. Table 8 list results obtained for two eggs. Other eggs gave similar results. In these analyses the centre of the effective conducting sphere was assumed to be the centre of the egg. The contour diagrams were used to determine suitable iteration starting points for the analysis program. These algorithm conditions yielded consistent predictions with lower R values than for

alternative sphere centre positions or very different iteration starting points. When good fits were achieved during the early consistent-signal period, an effective dipole was predicted lying central in the egg and pointing along the longitudinal axis at least 8 mm below the surface. The most reliable data suggest a 10-11 mm depth with the centre of the egg at 21 mm. Although the quality of the fitting is often good, it is not possible to identify an anatomical structure of the embryo corresponding to the predicted dipole. At 26 hours the embryo and its membranes are in contact with the upper membranes of the shell. As the embryo develops, it moves further from the top surface because of the increase in its weight. But by 60 hours, it is still centred above the expected dipole positions. A structure near the predicted depth is the latbrae canal (Figure 28) present during early stages of development. However, ionic flow up through the canal would give rise to radial currents and therefore no fields. Moreover, the signal strength (average 3E-7 Am) is suspiciously large for a single highly localized dipole of physiological origin. (In a 5 mm cube of tissue it would correspond to a current density of $\approx$ 240 μA cm^{-2} which is an order of magnitude greater than is found in most electrophysiologically active systems). An extended volume of source dipoles with a common orientation at a greater radius may provide a more reasonable explanation of the data. (The similarity between the fields produced by a dipole and a shallower

extended sheet of dipoles has been discussed by Okada - 1985).

Table 8

Dipole parameter predictions for 2 typical chick eggs (series L) using the dipole in a sphere model. Between 36 hours and 48 hours the embryo turns onto its left side (caused by increased weight and the various body flexures), dragging all the membranes with it.

Time	X_D	Y_D	Z_D	α	$P_x/E-7$	R
hrs	cm	cm	cm	°	Am	
Egg 1 (L series)						
26	0.20	0.69	2.13	288	1.13	.165
31	0.25	1.30	1.95	290	0.91	.132
38	-0.02	1.70	1.71	294	1.03	.125
43	-0.15	1.86	2.58	268	2.85	.033
49	-0.08	1.75	2.19	281	2.85	.045
55	0.02	0.43	2.39	259	4.92	.051
68	0.05	-0.40	2.66	238	10.40	.335
Egg 2 (L series)						
26	0.45	-1.79	3.29	228	1.25	.424
38	0.37	0.33	2.33	200	1.34	.160
49	-0.60	0.48	2.42	260	2.03	.390
55	-0.26	0.16	2.05	269	2.85	.065
68	0.14	0.17	2.14	224	4.26	.089

Sphere centre space was restricted to a region close to the centre of the egg (0,0,-3.5 cm).

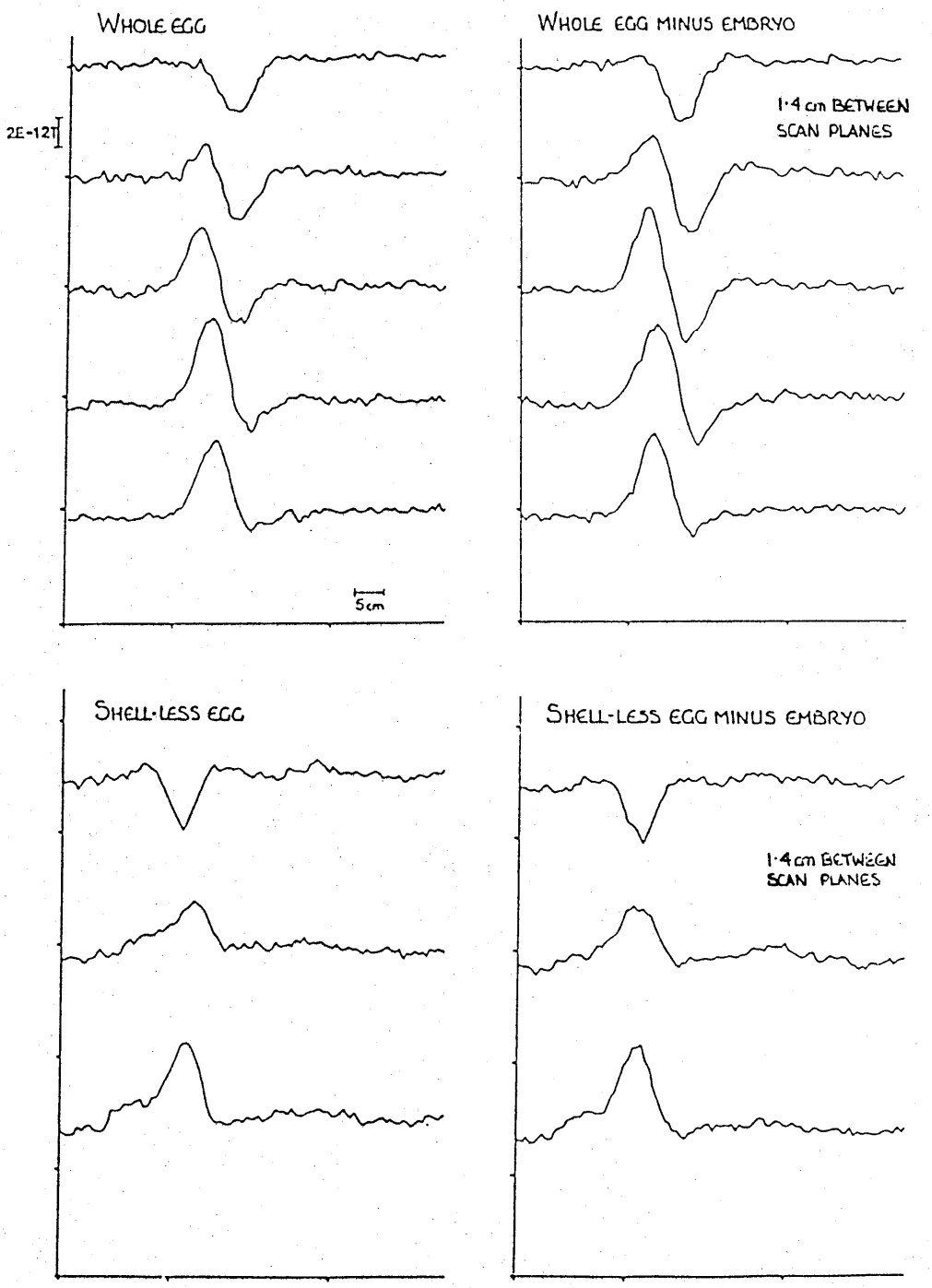

Figure 36 Effect of embryo removal on the magnetic field signal. For the whole egg the embryo was removed through a window. In the shell-less case, the egg contents were transferred to a saline bath resulting in a changed geometry from before

Up to this stage only *in ovo* experiments have been described. These are not definitive in that the detected field signal, or contributions to it, could arise from the embryo or from the extra-embryonic epithelial sheets or even liquid junctions accompanying chemical imbalances caused in a local area by nutrient digestion. By physical isolation of each possible source, the true contributors to the detected signal could be determined. To confirm the location of the source predicted, from both physiological considerations and the inverse solution, invasive and *in vitro* studies were carried out.

5.7 Invasive Experiments

Dissection Experiments

These experiments involved dissecting out well defined regions from the developing egg, starting with the embryo and the amnion around it and then continuing on in stages to the *sinus terminalis* and the yolk sac membrane. For membrane dissection experiments, the contents of the egg were carefully transferred out of the shell into a saline bath and floated onto a dish containing cotton wool. When measuring fields from structures other than those involving the yolk content, a saline-loaded soft sponge was used to support the structure. The change in geometry when the egg contents were in saline, resulted in a change in the detected field signal, but a distinct signal remained present (Figure 36).

These studies will now be reviewed, starting with the experiments involving embryo removal-the predicted effective dipole seemed to be located below the level of the embryo. A 36 hour embryo was dissected away from the attached blood vessels and the underlying yolk. Underlying structures were protected by cutting an opening close to the embryo and sliding a small aluminium spoon underneath the embryo before any subsequent dissection. This spoon also served (together with the cotton wool) to stabilize the yolk which tended to float when manipulated. By subsequent removal of the embryo proper, it was seen that it's removal had little effect on the detected magnetic field signal. Figure 36 shows the result of a typical experiment. Similarly insignificant changes were seen in 4 other eggs.

Draining of the blood within the terminal sinus (by cutting across the terminal sinus at 8 locations and cutting through the major blood vessels) stops the active membrane pumps involved with blood circulation (Armstrong 1975) but, in this case (2 eggs ≈36 hours incubation time), it did not affect the detected signal over a 35 minute period (when the egg was placed back into the incubator between measurements). However when the blood vessels and the directly underlying membranes (partly amnion and partly yolk sac membrane) were removed, the signal was reduced to 10-25 % of it's former value for 5 eggs (36 hours incubation time). Maceration (breaking and

mixing using a spatula) of the yolk membranes without removal of any membranes or embryo always resulted in loss of field signal (9 eggs between 2 and 4 days of incubation). The time from the first measurement set to the second set was less than 2 minutes in all cases. During this time the egg remained outside the incubator.

The above experiments suggest that the source of the signal is within the membranes of the yolk sac itself and although it is directly related to development of the embryo over a long time scale (few hours), it does not arise from the embryo itself. The next stage was to selectively inhibit the various active pumps found within biological organisms.

Poisoning Experiments

The poisons used were specific metabolic inhibitors designed only to inhibit the movement of a single species. Ouabain (a glucoside used in regulating energy delivered to the heart) inhibits the enzyme ATPase and thereby arrests the energy release required for active processes (Stryer 1975); cobalt chloride inhibits active calcium pumps important in embryological development, valinomycin inhibits movement of potassium ions across membranes and FCCP inhibits movement of protons (Catterall 1980) . The latter two act by combining with the species in question and forming a molecule too large to cross the appropriate gates. The final poison used was a detergent whose action

was to break down the membrane.

Final volume concentrations (in the egg) used were 15 - 50 μM. The solute was physiological saline in each case. Each bolus (of volume 1 ml) was injected slowly and was at incubation temperature. When each of the poisons were injected into the immediate vicinity (within 2 mm) of the embryo, the embryo itself died (heart stopped beating within 2 minutes of injection of the bolus), but the magnetic field signal was unaffected. Injection of boli into the amnion and allantois similarly had little effect on the detected signal in the short term (20 minutes). Destruction of the membrane potentials beneath the embryo itself, by use of detergents, had a dramatic effect in that the signals stopped immmediately. Injections of the other poisons into different compartments did not have any immediate effect, (nor did the detergent when injected into different compartments) in the short term. All the poisons killed the embryo within 20 ± 5 minutes and the magnetic signal itself usually stopped within 30 minutes of the embryo's death.

5.8 Discussion

The above account describes how magnetic field measurements, together with physiological consideration of the biological system, can yield information concerning developmental currents. In the case of the chick embryo, the magnetic field detected can be related to the developmental stage but the signal itself does not arise primarily from the embryo. Cooling and subsequent rewarming indicate a physiological origin of the magnetic field signal. The dissection and poisoning experiments show a possible mechanism for the signal genesis in that the ionic movements are related to the existence and integrity of the yolk sac membrane itself. It appears that the absorbtion of nutrients from the yolk underlying the membrane may be implicated. It may result in the formation of chemical imbalances which in turn, via the usual electrochemical equilibrium forces, cause a potential gradient to be set up.

As yet, this result has not been confirmed by electrode measurements but the general mechanism proposed is also indicated by work on the composition of the various compartments of the developing egg (Romanoff 1960).

BRAIN STUDIES

6.1 Introduction

There are a large number of neuromagnetic studies underway at present: they vary from clinical investigation of the locations of epileptic foci (Barth et al 1987, Narici 1987) to academic studies of cognitive processes (Weinberg et al 1987, Kaufman et al 1987). An important element of all these studies is the mapping of the sources. To facilitate this, simplified models and geometries are invoked to represent the brain. The single current dipole in a homogeneously conducting sphere model is very widely used (for example Physics in Medicine and Biology vol 32, 1987).

Thus far in this thesis, the limitations of the dipole in a sphere model have been explored using physical models and its use in the analysis of a real system illustrated by experiments on the developing chick embryo. In each of these cases, the predicted equivalent dipole location could be correlated with the results of physical examination. Now the model will be applied to investigate the magnetic fields associated with the human visual evoked response where direct verification of the dipole location will be impossible. The modelling issues discussed previously will be relevant in assessing the information our data yields on the organisation of the visual cortex.

Before the experiments and the analysis are discussed, the visual pathway through the brain will be described briefly.

6.2 The Visual Pathway

Many texts adequately describe the structure and physiology of the human eye (for example Open University SD286 1982) and, for the purposes of this discussion, only the basic facts of retinal cell organisation are of consequence. Light enters the eye through the lens and is focussed onto photoreceptor cells at the back of the retina. The photoreceptors are behind other retinal cells (Figure 37) and are of two varieties; rods, specialized for low intensity monochromatic vision and cones used for chromatic vision in reasonably bright light. Rods and cones synapse onto the bipolar cell layer and in turn, the bipolar cells synapse onto ganglion cells. The degree of convergence as the signal proceeds from the photoreceptor cells to the ganglia varies across the retina with little or no convergence across the fovea and extreme convergence at the periphery. This reflects the distribution of rods and cones across the retina (Figure 38).The packing density of the cones decreases sharply outside the fovea while that of the rods increases from zero, reaching a maximum just outside the macula. From here to the edge of the retina, the cone density remains at a low level and the rod density slowly declines as well.

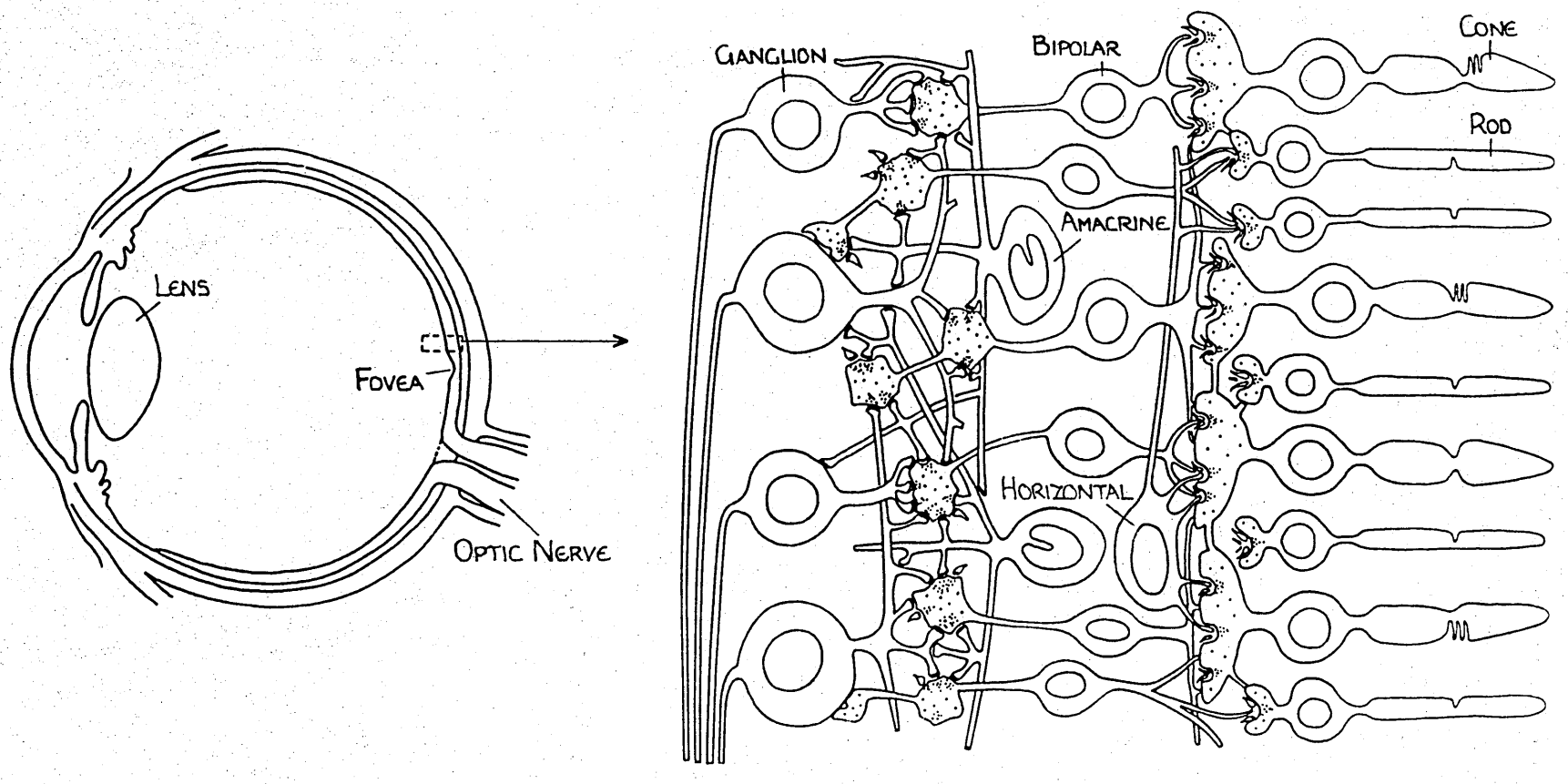

Figure 37 Cross section of the eye and the retina. The photoreceptor cells are behind the primary processing cells. In each diagram light enters from the left

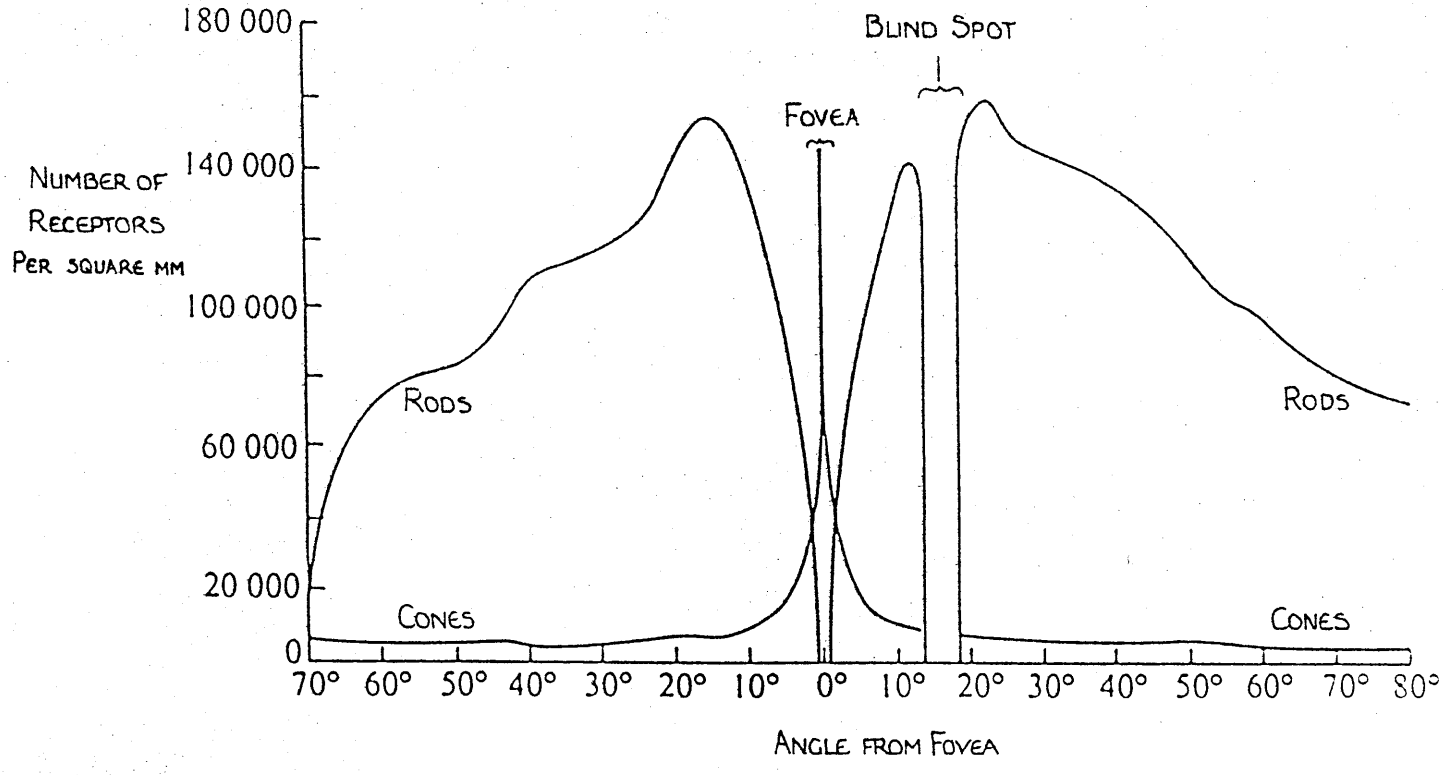

Figure 38 Distribution of the rods and cones across the retina

Absorption of light by the receptor cells causes hyperpolarisation and influences the bipolar cells. In turn the bipolar cells cause a depolarization of the ganglion cells necessary for the initiation of the action potential. This represents the vertical or direct connection. A horizontal control system also exists to influence distant cells within a layer, enabling lateral control (inhibition and stimulation) to occur. This provides, for example, a mechanism of accentuation of brightness contours. An edge between a dark and a light area stimulates the visual system powerfully. This is just one example of the processing via the different layers of retinal cells (Kuffler and Nicholls 1986) that enhances the details of an image before the information is transmitted down the optic nerve as a pattern of action potentials.

Ganglion cell axons travel in the optic nerve to the optic chiasma where they undergo partial decussation and enter one or other of the optic tracts. Most of the fibres in each optic tract then terminate in the lateral geniculate nucleus, which is the thalamic relay nucleus for vision. Geniculate fibres travel through the internal capsule and corona radiata to the primary visual cortex in the region of the calcarine fissure. In addition, a considerable number of optic tract fibres project to the mid-brain and a few to the hypothalamus (Figure 39).

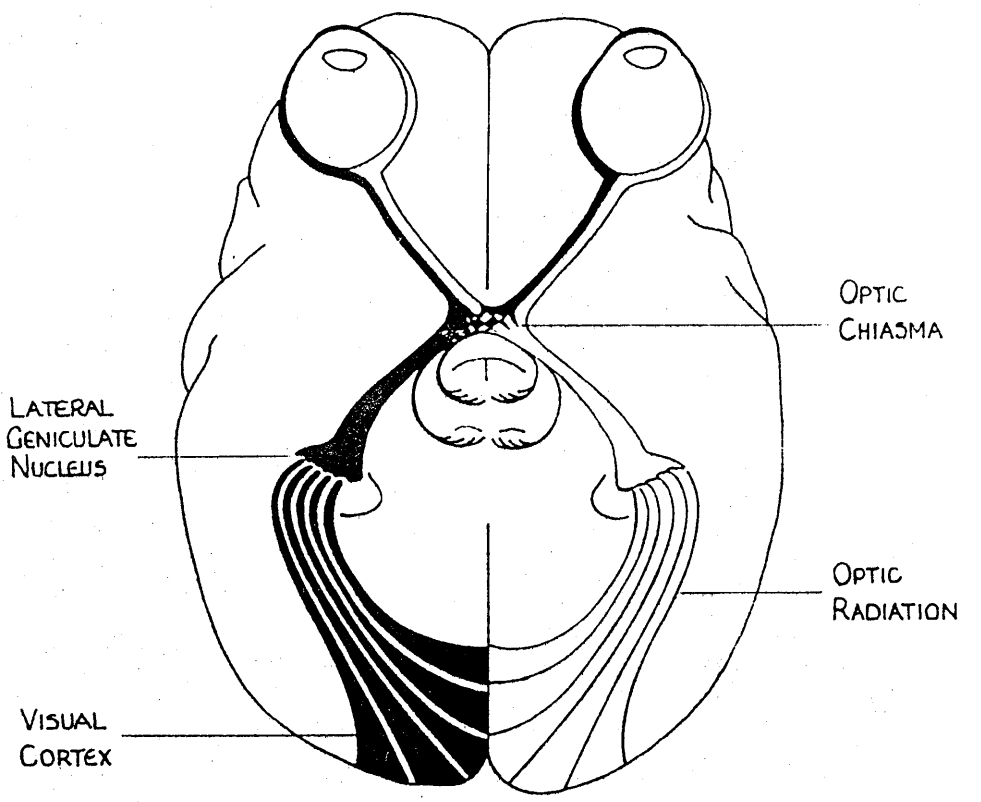

Figure 39 The visual pathway from the eye to the cortex

Retinotopic organization is maintained at the cortex. Inferior visual fields project to the cerebral cortex above the calcarine fissure and superior fields to the cortex below the fissure (Figure 40).Cortical representation is contralateral to the stimulus. The fovea and macula are represented more posteriorly and peripheral fields more anteriorly. Investigation of this representation in the case of one widely used visual stimulus forms the basis for the experiments described in this chapter.

6.3 Visual Evoked Responses

A change in the visual input is rapidly relayed, in a defined manner, to the brain. The small degree of variability is such that by timing how long a signal takes to travel from one area of the visual path to another, neurological dysfunction can be diagnosed. The electrically recorded visual evoked reponse (VER) to various stimuli (pattern onset, offset, reversal) is well known (Halliday et al 1977).

A checkerboard pattern can be made to change abruptly in a variety of ways and each mode of change produces responses with particular characteristics. We chose a pattern reversal stimulus as this gave a sharply defined positive pulse at ~100 ms for the electrical response (Figure 41) with the main positivity to lateral hemifield illumination ipsilateral to the stimulus (although when recording scalp

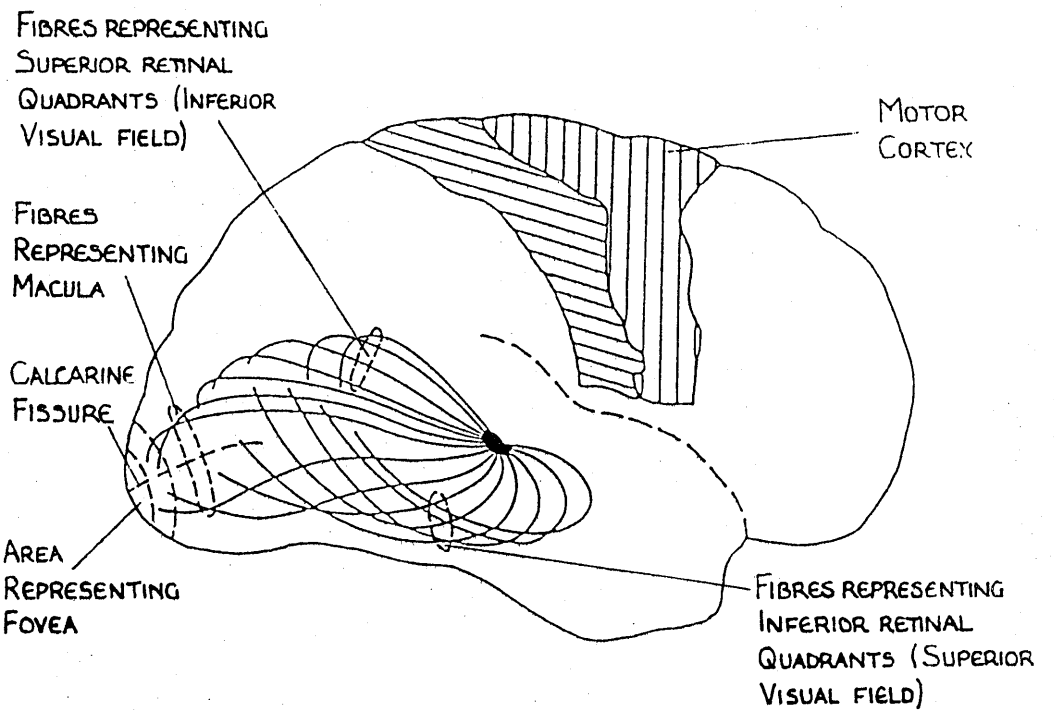

Figure 40 Representation of the optic fibres on the cerebral cortex. Sets of fibres representing different visual regions radiate out from the lateral geniculate nucleus

potentials, cortical positivity may be denoted by a downward deflection depending on the reference point chosen). This pulse is thought to be generated by extrastriate cortex forming the outer occipital convexity (Michael and Halliday 1971). Responses to pattern offset and reversal show similarities in waveform, which are characterized by a negative-positive- negative complex with peaks at 60-70 ms, 90-110 ms and 140-155 ms for full field and lower half field stimulation.

The features of the typical electrical response evoked by a reversing checkerboard pattern can be explained in terms of signal conduction, latencies and velocities. However there are difficulties in forming a simple description as there are different types of ganglia involved in the optic pathway. X cells have small cell bodies and low conduction velocity but are activated rapidly. On the other hand, Y cells are larger, have faster conduction, but have a longer activation time. Within the retina itself, the fibres are unmyelinated and the signal can take up to 25 - 40 ms to reach the optic nerve, the value depending on the amount of convergence. A further 25 - 30 ms is required for the signal to travel from the ganglion cells to the lateral geniculate nucleus. The major component of the signal observed at the scalp is observed at approximately 100 ms; it occurs when the signal reaches the visual cortex. As the signal is then further processed by the visual association areas, further features are seen

in the scalp evoked response.

The area of visual field stimulated dramatically affects the evoked response due to the difference in density of retinal cells and the degree of convergence involved. By stimulating small regions of the visual field and performing the inverse calculation on magnetic field data obtained in the corresponding cortical regions, the exact retinotopic representation of each retinal region on the visual cortex can be studied.

A great number of evoked response studies have been carried out using electrical responses. We have utilized both electrical and magnetic techniques in our study. The electrical potential is recorded differentially with a known reference point. In contrast the magnetic response can be recorded without reference at a given point. Another major difference between the two techniques is the smearing of the electrical signal by the differing conductivities of the brain, cerebro-spinal fluid, skull and scalp. This does not occur for the magnetic field recordings because the permeability of these regions is very similar and hence they are essentially transparent to the magnetic signal. It is also important to note that (in a spherical model) the electrical recording is sensitive to both radial and tangential components of any dipole source whereas the magnetic signal is only sensitive to the tangential component.

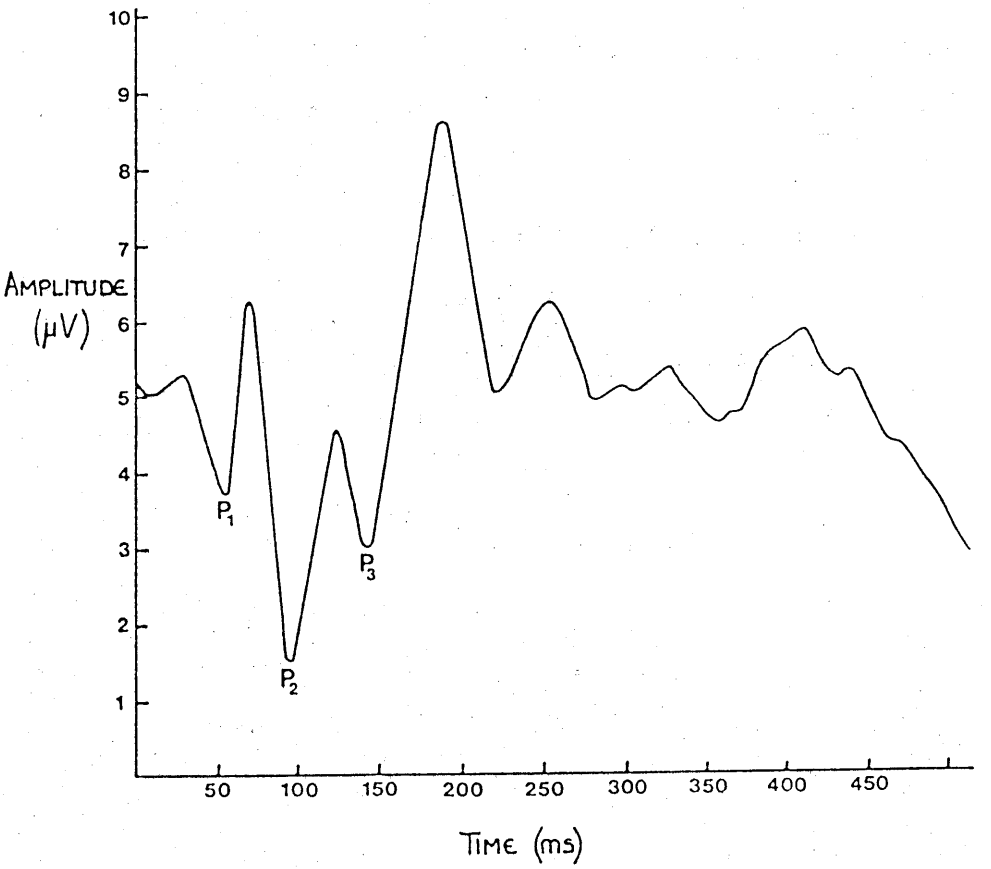

Figure 41 Typical visual evoked response from a pattern reversal checkerboard. (Subject BJ. The electrode positions are F_Z reference, O_1 active and mastoid ground on the 10-20 electrode system). Positive voltages (active-reference) are deflected down on this EEG system (Nicolett Pathfinder 11)

The experiment described in this chapter involved stimulating the right half field and then in turn the upper and lower quarters of the right field. If the retinotopic representation is maintained, then the vectorial summation of the early evoked responses of the two quarter fields should closely resemble the response of the half field. I will discuss the sources evoked by these stimuli later.

6.4 Recording The Evoked Response

The first step in evoked response studies is to devise a standard repeatable stimulus. In our experiments a checkerboard image was back projected, via a mirror mounted on a rotatable shaft and a fixed mirror, onto a translucent diffusing screen (Figure 42). The stimulus consisted of reversal of the checkerboard pattern. It was important to ensure that the stimulus generation did not affect the magnetic field recorded by the SQUID magnetometer. The pattern reversal was achieved through a galvanometer system consisting of a large permanent horseshoe magnet in a double skinned electrically isolated box with a small coil on a shaft between the poles. This shaft projected through a small aperture in the electrical shielding. The shaft, on which the movable mirror was mounted, was rotated by applying a current to the coil. The entire assembly together with the slide projector was placed outside the Helmholtz coils at a distance of ≈ 125 cm from the SQUID magnetometer pick up coils.

The relative positions of the eye and the checkerboard pattern were kept constant by attaching the stimulus generating assembly to the moving platform described earlier. The subject lay face down and peered through two small apertures between the end of the platform and the head restraint looking at the screen below. One slight problem was subject and mirror movement, both of which caused vibrations to be set up resulting in artefacts from

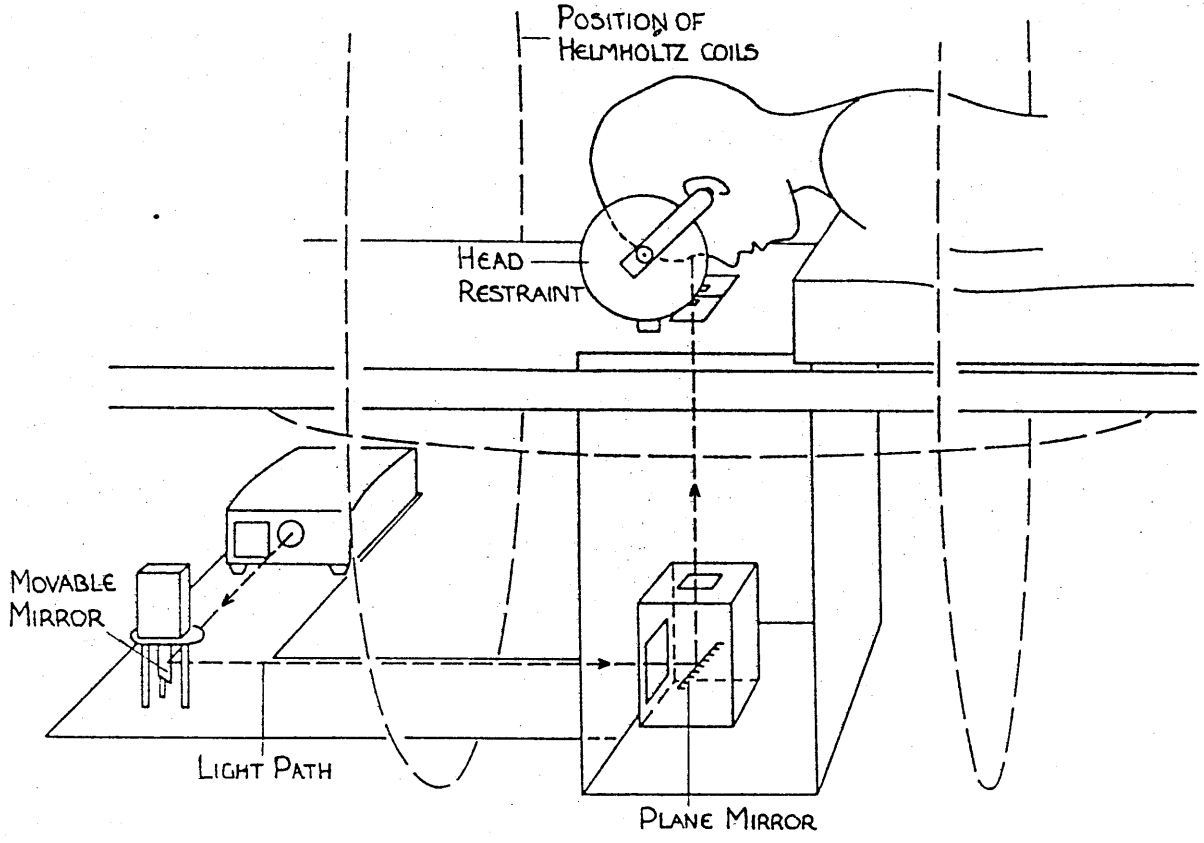

Figure 42 Geometry of the magnetic visual evoked recording experiment

the galvanometer magnet. To overcome this, during the data acquisition phases, lead weights were placed close to the moving mirror assembly to dampen the vibrations. In this way the stimulus artefact signal was reduced to below 20 fT.

Each check subtended 0.22° and the total available screen size was 5° (i.e the visual field stimulated was cone dominated). For the half and quarter field stimuli, the full screen was used with three fixation points on the left edge, at the centre and top and bottom corners. The pattern was reversed by moving the image through one check distance, under computer control, every 0.5 s with a switching time of ≈ 10 ms. A randomly chosen delay of up to 30 ms was introduced to counter subject anticipation. Evoked response data was collected every 6 ms for 414 ms. The pattern movement and the data acquisition were controlled by the same computer program (Figure 43). Each pattern reversal represented one data sweep. Noisy groups of sweeps were detected by calculating the maximum difference within each subset of 10 sweeps. If an appropriately chosen threshold level was exceeded, all 10 sweeps were eliminated from the data. An 8 s rest period was introduced every 50 sweeps. 400 sweeps were averaged in the magnetic field measurement but only 200 sweeps were required for the electric potential response because of the more favourable signal to noise ratio. The illumination of the whole pattern at the eye was 5 lux,

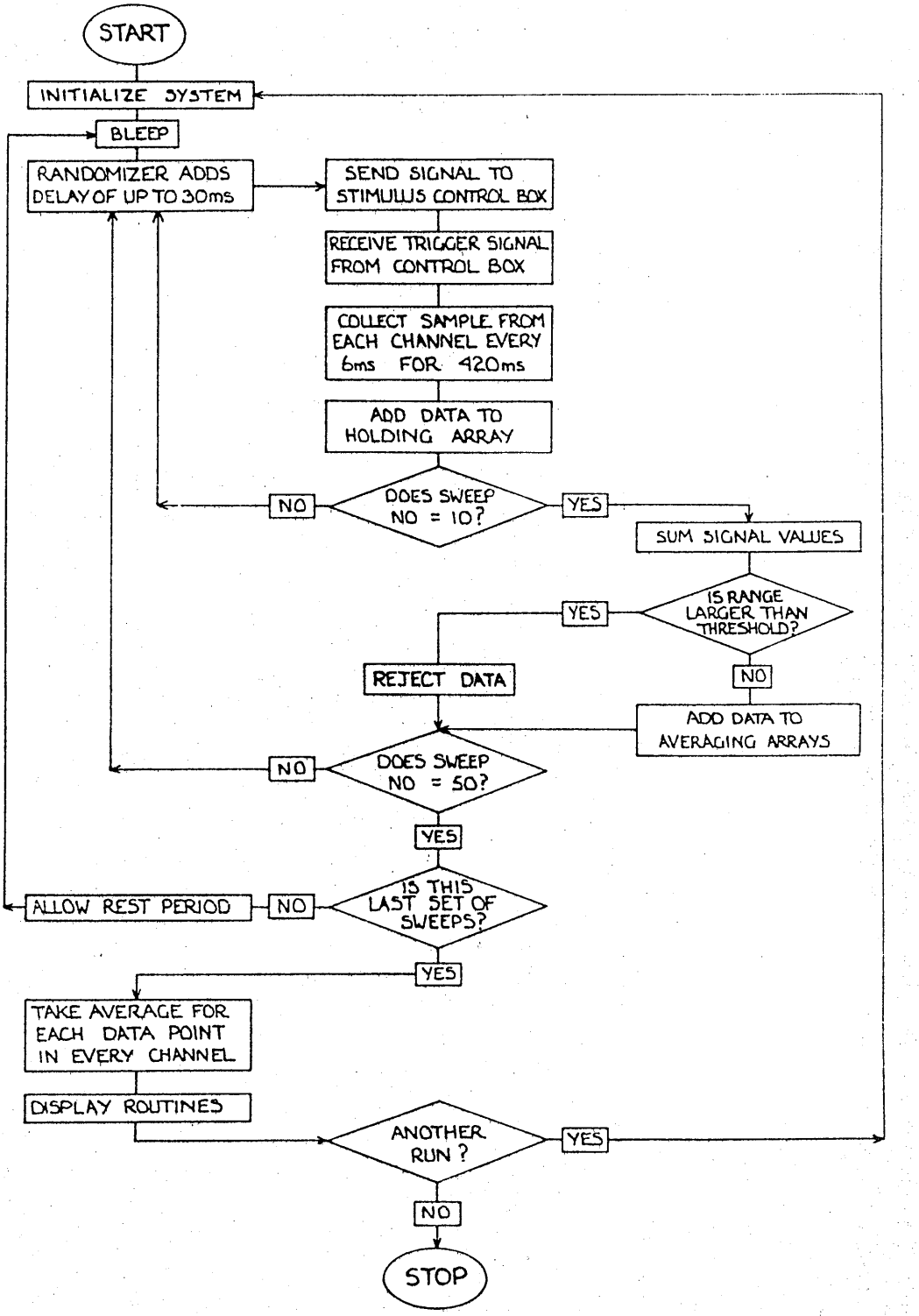

Figure 43 Block diagram of the visual evoked data acquisition program

with 65% contrast between the light and dark squares. All experiments were carried out in a semi-darkened room.

In the electric potential measurements silver chloride cup electrodes (SLE) were glued onto the scalp. Skin impedance for each electrode was below 2 kΩ after abrasion of the skin and the filling of the electrode cup with conducting gel (Camjel). The recording sites were referenced to the vertex and the mastoid was used as ground (Figure 44). Differential signals were filtered (0.3 Hz high pass and 65 Hz low pass) and amplified by a commercial EEG amplifier system (Digitimer DM 5000) before input to the computer.

Magnetic field measurements of the evoked responses were made with the magnetometer previously described. A line frequency notch and a 65 Hz low pass filter were used. Throughout the experiments the dewar remained fixed. Only single channel recordings were possible with our magnetometer. Data was collected over a number of sessions, with rest periods in between and a complete mapping made over the back of the head. The signals were highly repeatable (Figure 45).

The subject was positioned at points on a square grid (2 cm x 2 cm covering an area of 12 cm x 8 cm) in a horizontal plane under the detector by movement of the bed. Accuracy of positioning was ± 2 mm. To ensure correct

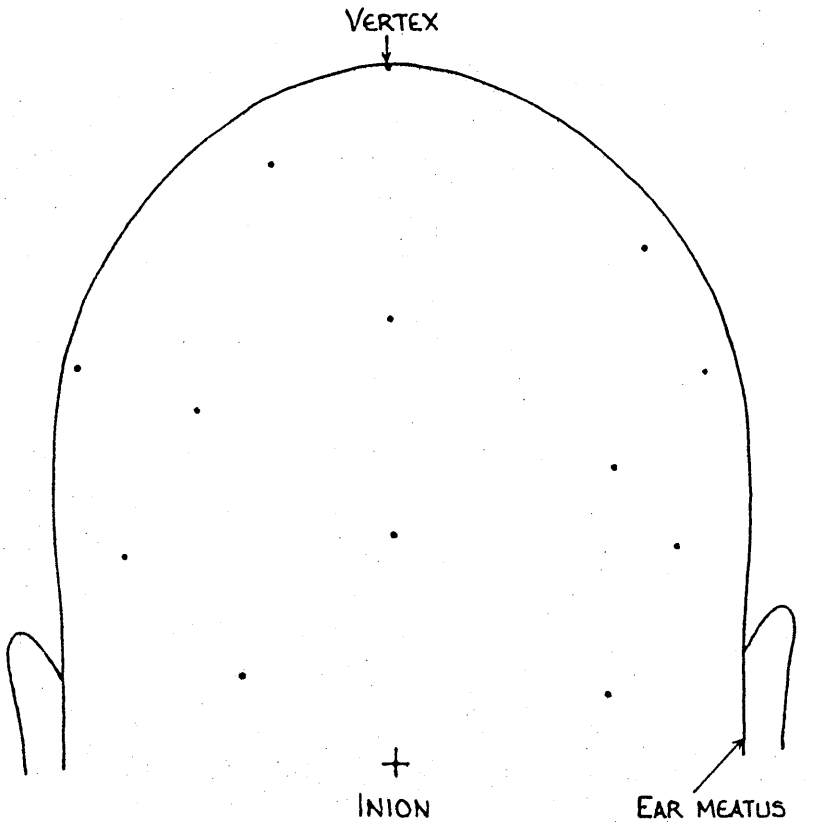

1cm

Figure 44 Electrode sites used for the half and quarter field stimulation experiment

positioning of the subject on the bed a head restraint system was used. Position of the ear meatus on each side was noted and the subject looked through two small apertures ensuring that the screen was fully visible. On each subsequent repositioning the exact position was reproduced to view the screen with the ear meati in the same positions. Centre of the SQUID dewar tail was positioned over the inion as a reference point for each recording session. The shape of the head was determined by measuring the vertical distance from a fixed point on the dewar support to points on the head.

For both cases, electric potential and magnetic field recordings, the data was transferred to the main frame computer for processing. Signal contours were produced for each data epoch prior to any analysis.

6.5 Results And Discussion

The three areas of retinal illumination used were the top right quarter field, the bottom right quarter field and the right half field. The strengths of the observed responses as a function of latency were parameterized by summing the squares of the individual values in the data set for that latency. We termed this quantity, the signal power P. For the magnetic field signal this was simply

$$P = \sum_i S_i^2$$

where S_i was the data value at the ith measurement position. However, for the electric potential, there is a complication in that all the signals were referenced to the vertex. In this case the average value for the whole data set for that latency was subtracted from each individual value for that latency, prior to summing the squares and calculating the power P which is then independent of the reference signal. Now the power term is defined by

$$P = \sum_i \left[\left[S_i - S_r \right] - \sum_i \left[S_i - S_r \right] / N \right]^2$$

$$= \Sigma \left[S_i - \hat{S}_i \right]^2$$

where S_i is the potential at the ith site, S_r is the reference potential (at the vertex) and N is the total number of points.

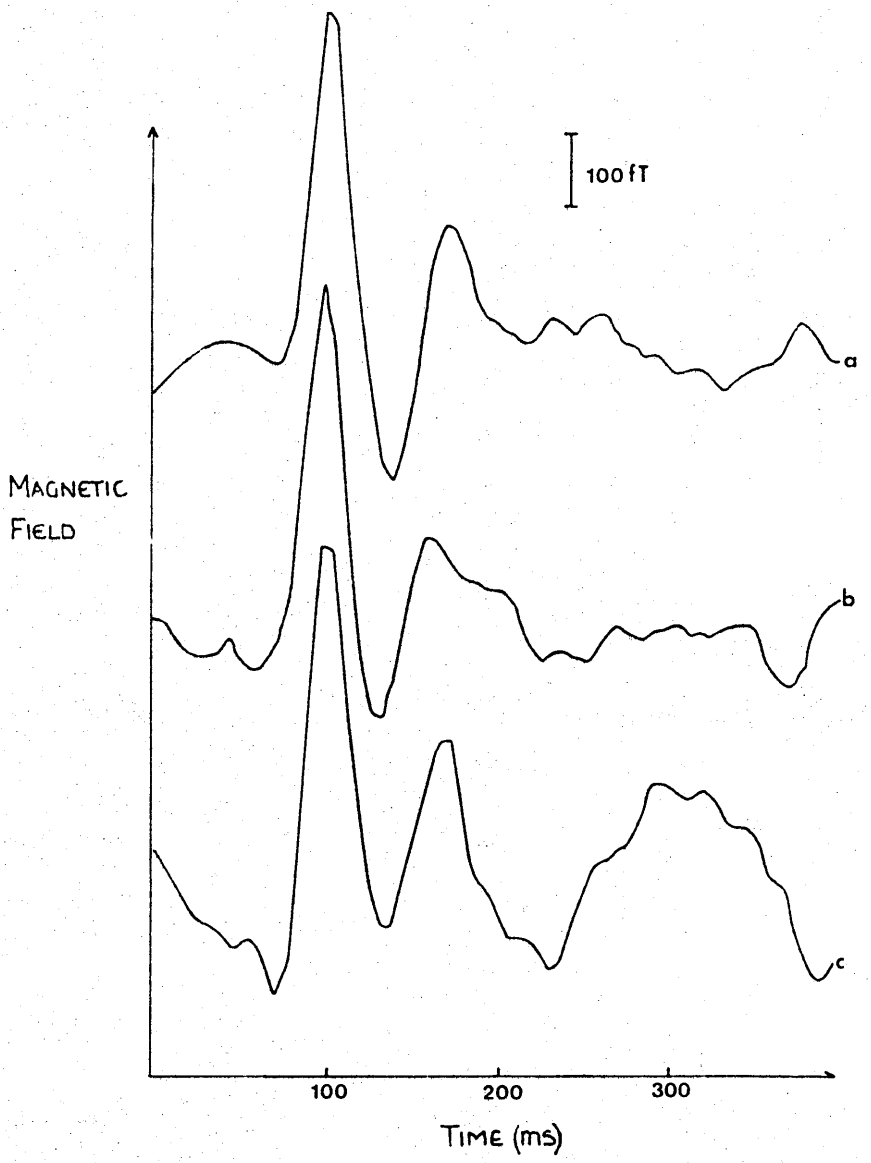

Figure 45 Magnetic fields as a function of latency recorded at a position on the midline 4 cm superior to the inion. a) and b) were recorded with right hemifield stimulation one week apart. c) is the sum of the two right quarter field responses at the same site

The signal power for electric potential and magnetic field for the three areas of illumination (for subject SS) are shown as a function of latency in Figures 46 and 47. The P100m is clearly visible at a latency of 96 ms for the half field data obtained with magnetic measurements. In contrast the peak signal power for the potential data occurs at a latency of 84 ms for the same region of stimulation. This difference was unexpected and repeatable. It cannot be explained by instrumental effects as the same filter levels were used for both types of signal. The bottom quarter field power peak for the electric potential also occurred at 84 ms and the top quarter field peak occurred at 90 ms while the magnetic signal peak occurred at 96 ms again for both top and bottom quarter fields.

Contour maps of the magnetic field and electric potential at a latency of 96 ms are shown in Figure 48 for the three types of stimulation. Location of the equivalent current dipole for each set of data was attempted by the iterative fitting procedure using the dipole in a sphere model as described previously. The fitting was again carried out as a function of model sphere centre position. The 'cranial centre', defined for our purposes as the centre of the sphere that was the best fit to the back of the head, was calculated from the shape of the head. Table 9 summarizes the predicted dipole parameter results.

Table 9

Predicted dipole parameters for half and quarter field stimulation experiment. Analysis was carried out over a cubic grid of model sphere centre space for subject SS at a latency of 96 ms. The inion is at (0,0,-1.5) and the cranial centre at (0,4.7,-9.9)

	X_D	Y_D	Z_D	α	P	R
	cm	cm	cm	°	E-8Am	
Half field	(Lowest R sphere centre 0,5,-10)					
Lowest R	-0.70	1.65	-3.62	-9	7.83	0.16
Average	-0.81	1.57	-3.67	-11	8.37	0.18
Top Quarter	(Lowest R sphere centre 0,5,-9)					
Lowest R	0.91	2.80	-4.93	67	13.50	0.36
Average	1.10	2.40	-4.21	57	12.40	0.38
Bottom Quarter	(Lowest R sphere centre 0,4,-10)					
Lowest R	-0.74	3.10	-2.92	-44	4.87	0.22
Average	-0.67	3.11	-2.92	-44	4.85	0.23

The lowest R sphere centres are all close to the cranial centre. In this case a sphere centred on the cranial centre has been shown to be the most appropriate model

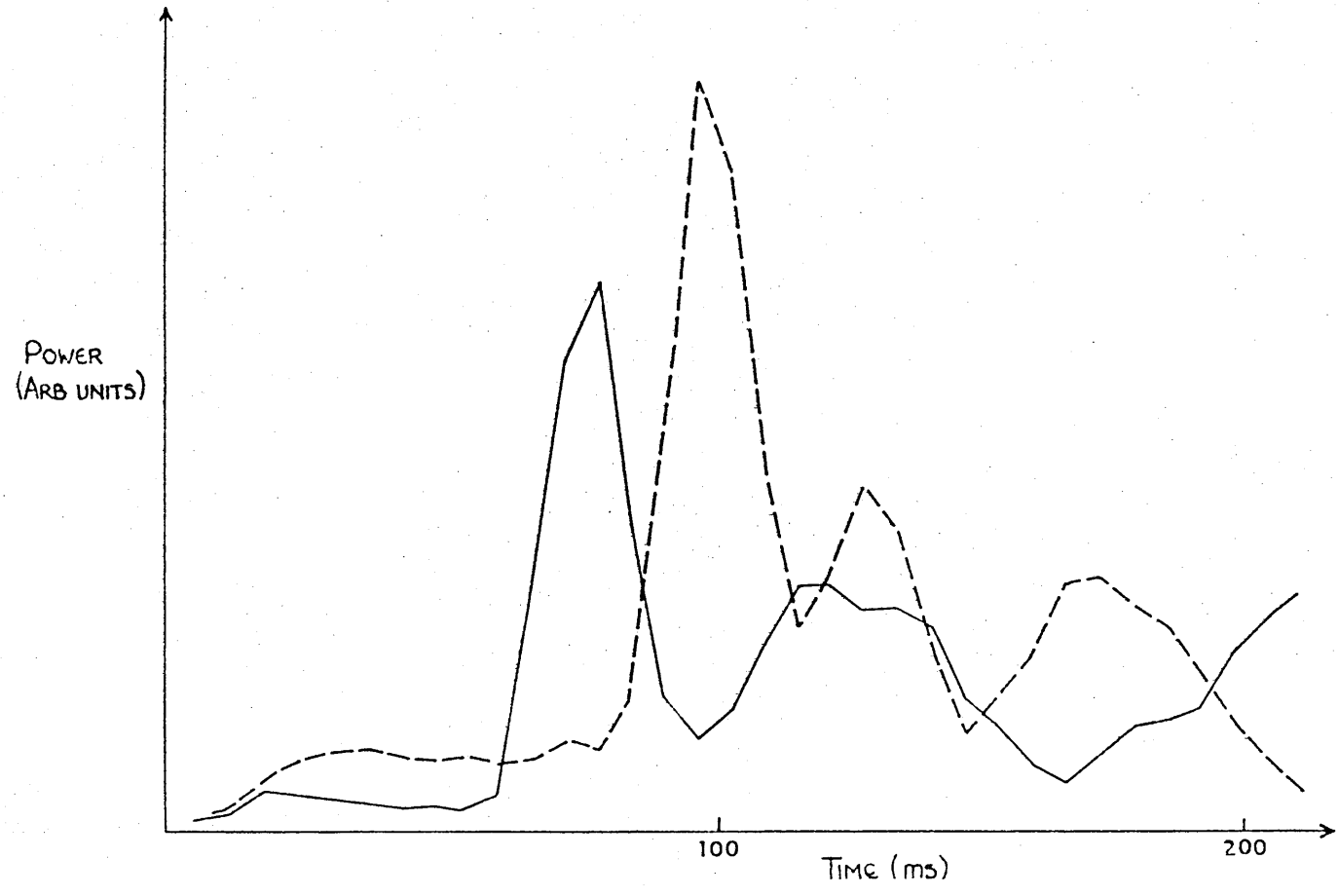

Figure 46 Signal power curve for the electric potential (solid) and magnetic field (dashed) data (half field stimulation -subject SS)

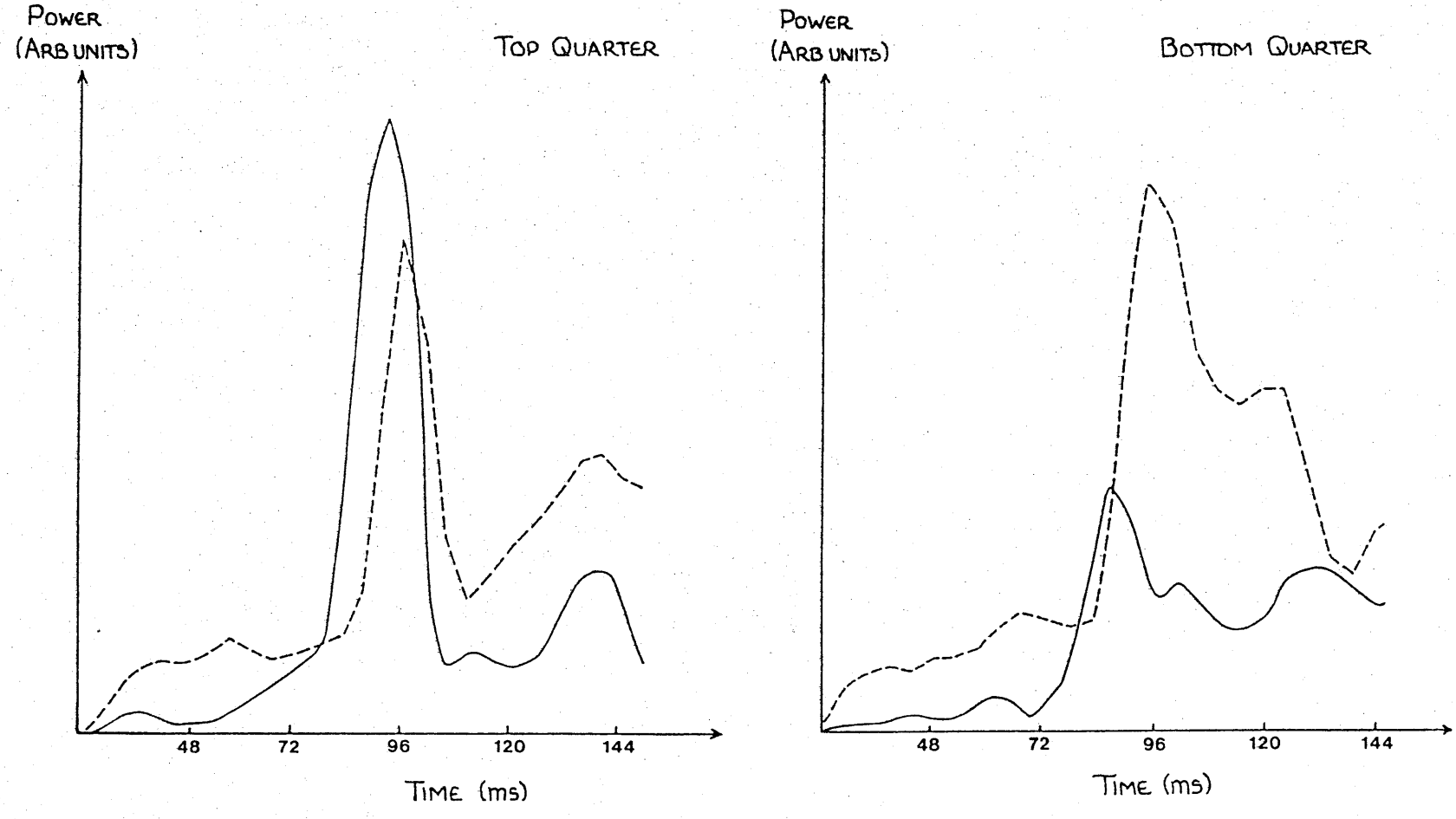

Figure 47 Signal power curves for the electric potential (solid) and magnetic field (dashed) data (quarter field stimulation)

Thus far, the contour maps and analysis are concerned with a single latency. However, there may be additional information available from the evoked response. The signal power curve may indicate other latencies when the underlying activity is coherent and the source distributions likely to be dipolar. Contour maps were drawn (Figures 49, 50 and 51) and analysis carried out at latencies which were at or close to peaks in the magnetic signal power curves (Figures 46 and 47). Model sphere centres chosen were restricted now to a region around the cranial centre. A latency corresponding to a trough was also investigated for each stimulation field (Figure 52). These results are summarized in Table 10. The predicted dipoles are plotted on the relevant figures.

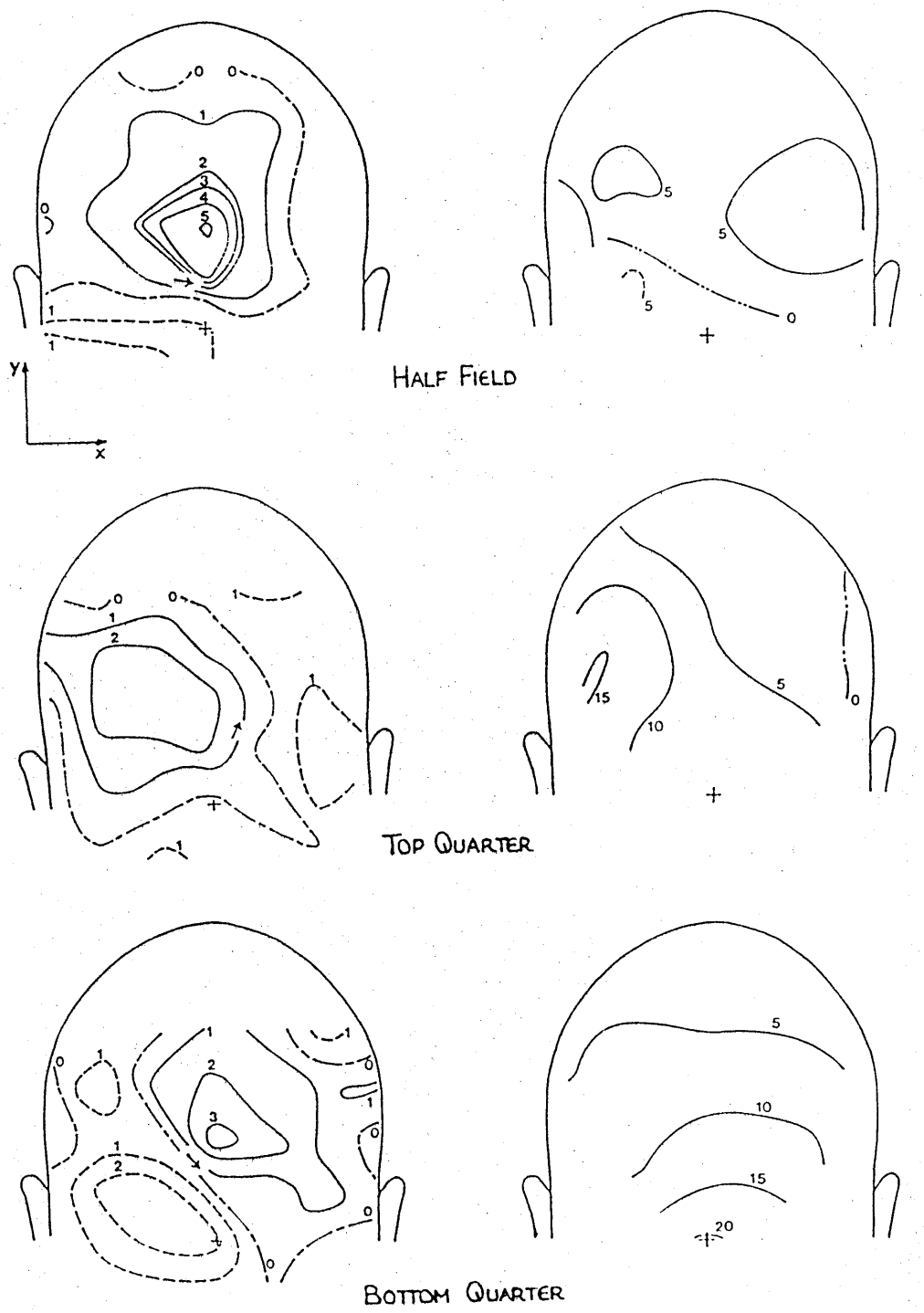

Figure 48 Contour maps for magnetic field (left) and electric potential (right) data at 96 ms latency. Contours are at 100 fT and 5 mV intervals, solid lines indicate positive B_z and V_i-V_r

Table 10

Predicted dipole parameter (lowest R) values for latencies near peaks in the signal power curves. Model sphere centres chosen were close to the cranial centre

Latency/ms	X_D/cm	Y_D/cm	Z_D/cm	α/°	P/E-8Am	R
Half field stimulation						
90	-0.57	1.52	-3.20	-5	4.39	0.25
96	-0.70	1.65	-3.62	-9	7.83	0.16
102	-0.90	1.66	-3.69	-16	7.60	0.19
126	-1.65	1.48	-3.81	23	5.73	0.26
168	-3.01	1.88	-2.83	-57	2.16	0.46
Top quarter field stimulation						
90	1.06	3.20	-4.70	79	9.02	0.44
96	0.91	2.80	-4.93	67	13.50	0.36
102	1.33	3.11	-4.30	79	7.82	0.41
138	-0.63	3.39	-6.59	58	23.09	0.38
144	-0.36	4.23	-6.45	66	22.93	0.32
Bottom quarter field stimulation						
96	-0.74	3.10	-2.92	-44	4.87	0.22
102	-0.99	3.06	-2.95	-45	4.65	0.25
108	-1.42	2.96	-2.64	-58	3.12	0.31
126	-1.31	2.23	-4.00	-138	6.49	0.32
132	-2.99	2.19	-4.01	-192	5.82	0.32
Latencies corresponding to troughs in the power curves						
Half 114	-1.50	2.23	-2.45	-92	1.78	0.43
Top quarter 114	0.45	4.78	-3.25	-11	2.18	0.61
Bottom " 84	0.76	3.10	-2.22	-60	1.22	0.59

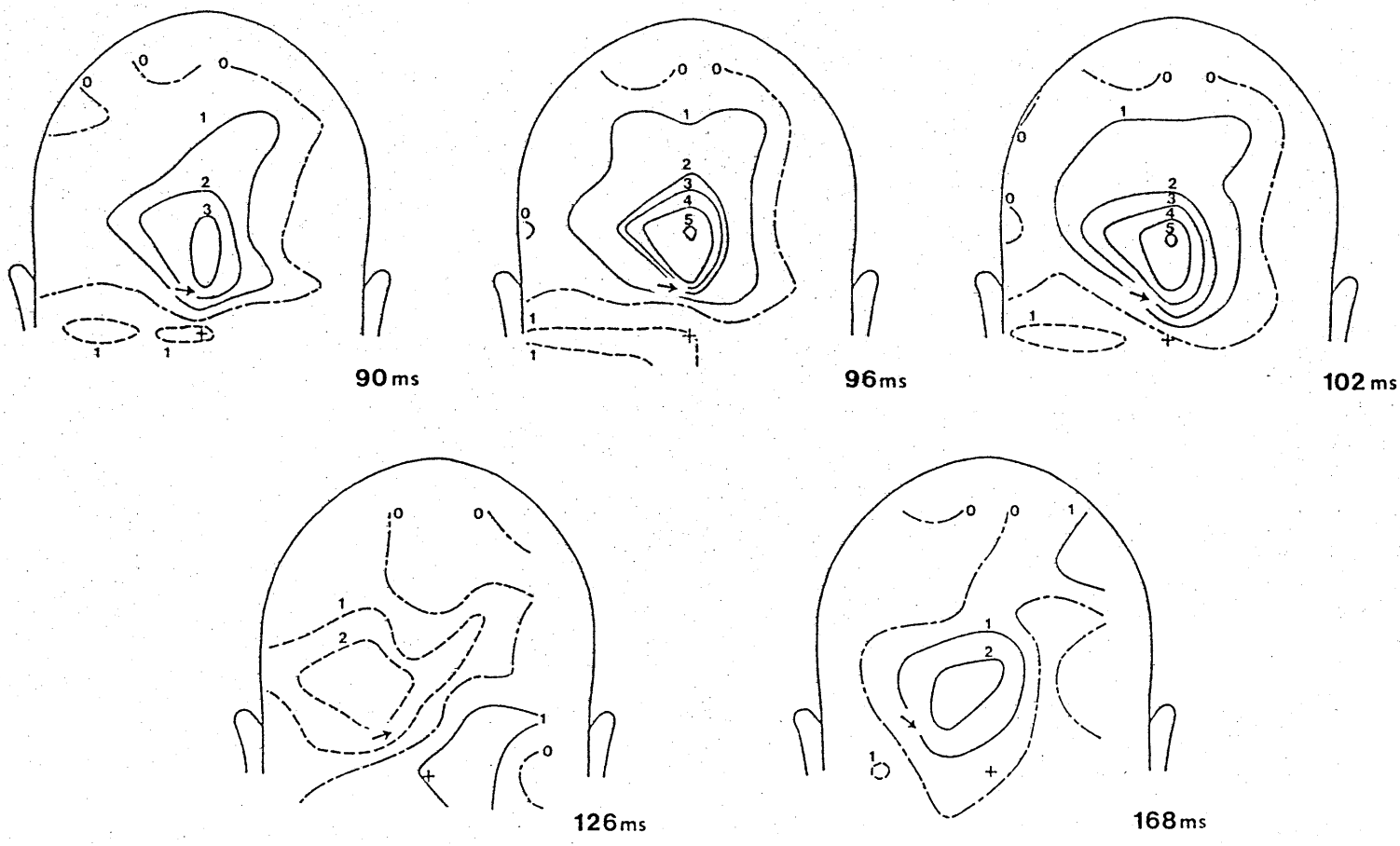

Figure 49 Contour maps of magnetic field data for latencies corresponding to peaks in the signal power curve - Half field stimulation. Solid lines are positive Contours are at 100 fT intervals

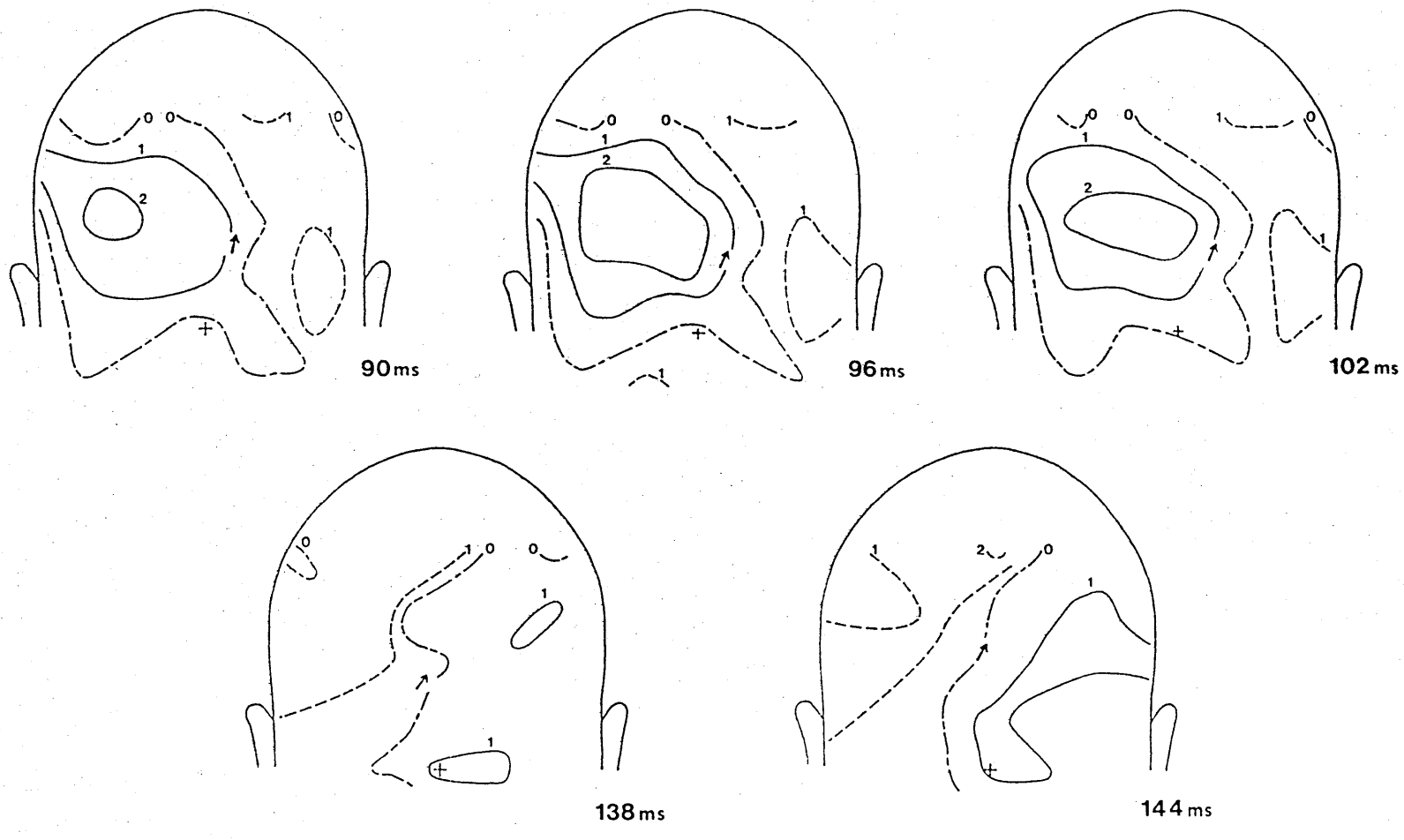

Figure 50 Contour maps of magnetic field data for latencies corresponding to peaks in the signal power curve - Top quarter field stimulation. Solid lines are positive

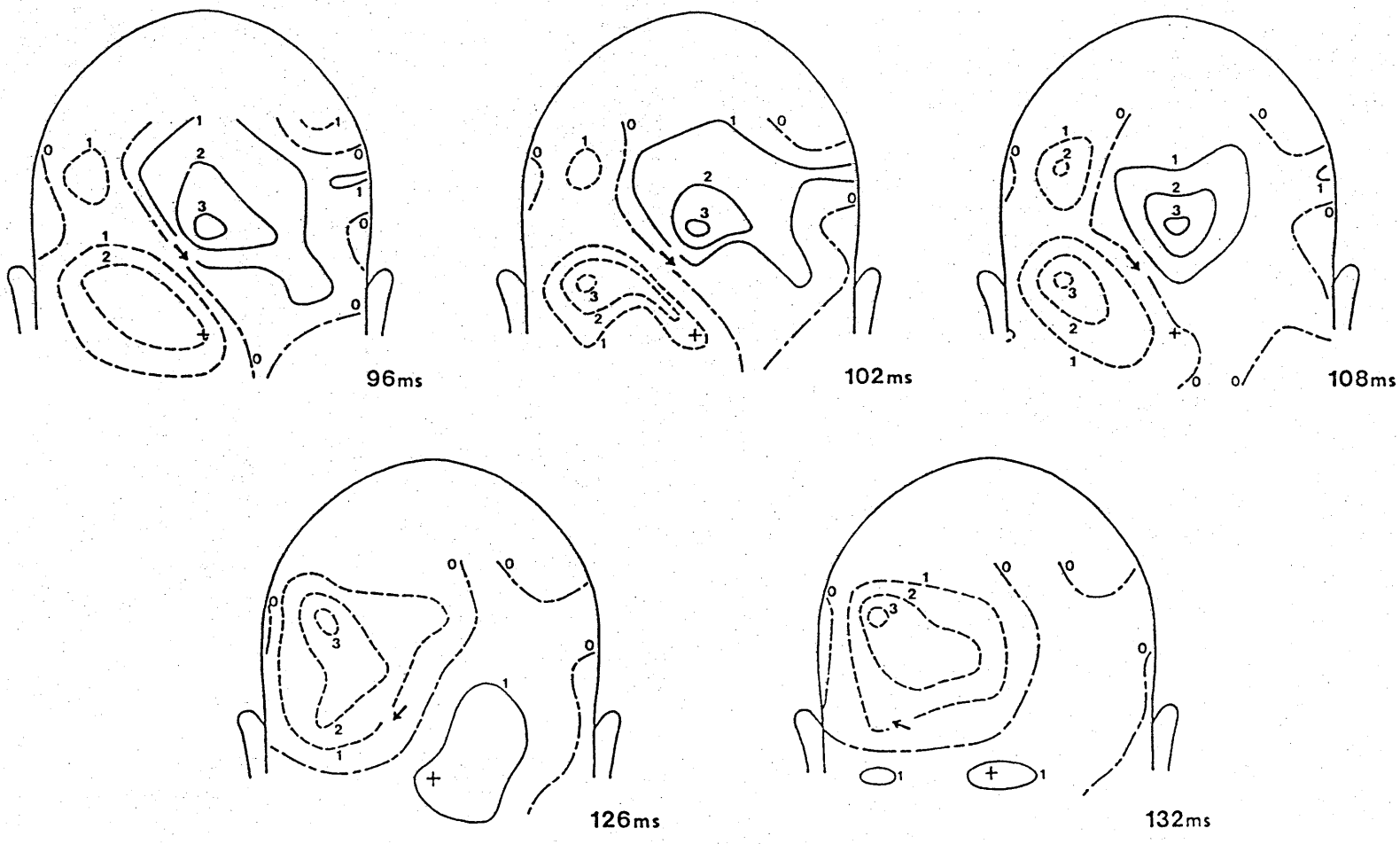

Figure 51 Contour maps of magnetic field data for latencies corresponding to peaks in signal power curve - Bottom quarter field stimulation. Solid lines are positive. Contours are at 100 fT

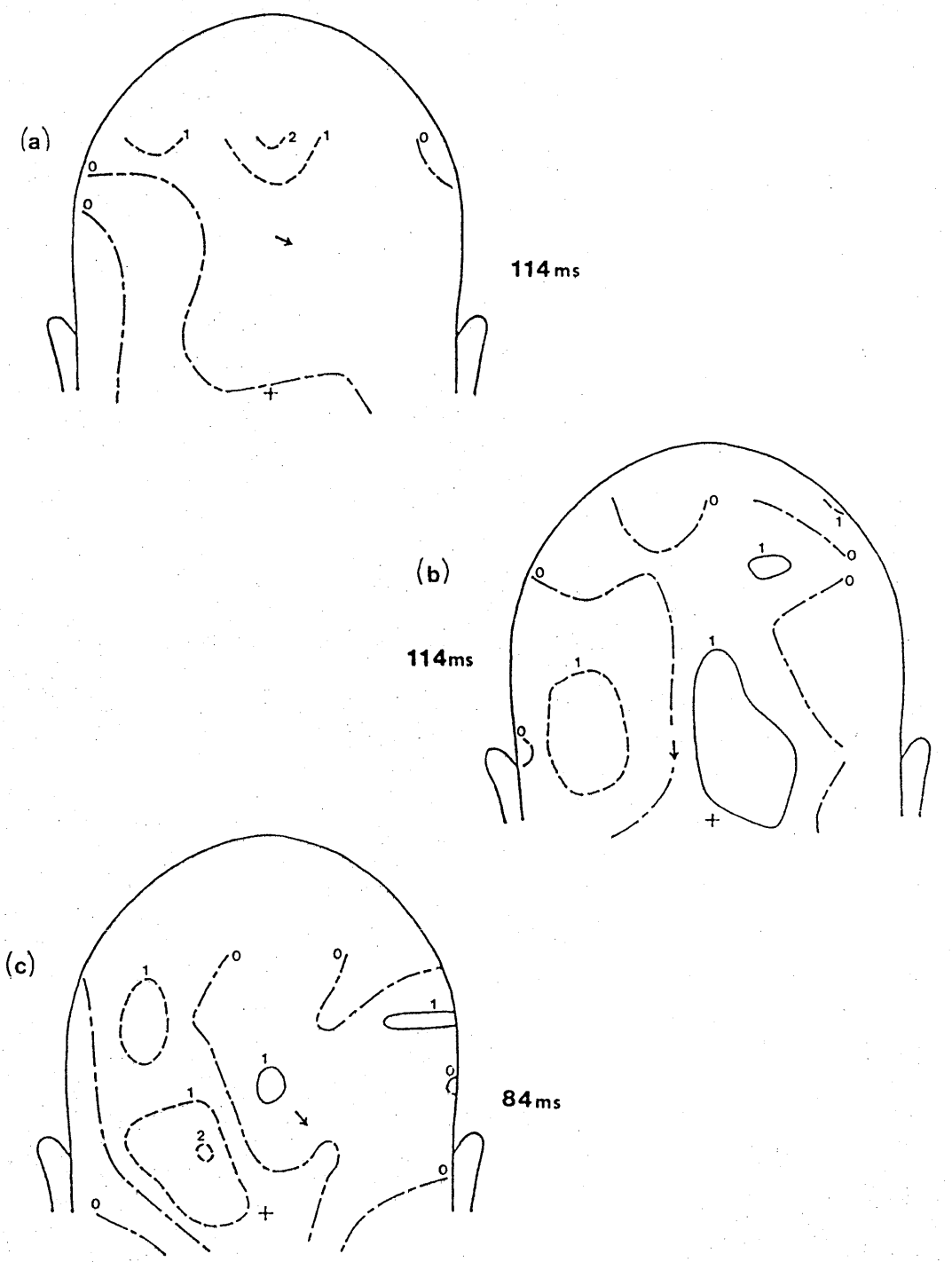

Figure 52 Contour maps at latencies corresponding to troughs in the signal power curve. a) Top quarter b) Half field and c) Bottom quarter stimulation. Solid lines are positive

The major difference between the contours at the peak value and those at the trough for any particular stimulation field is signal magnitude. As the signal to noise ratio decreases (for latencies corresponding to troughs), the fitting becomes more difficult. This was particularily noticeable for the example in Figure 52c where the dipole prediction was strongly dependent on the iteration starting point in dipole parameter space.

For latencies 90 ms -102 ms, consistent dipole positions were found for each of the half field and bottom quarter field data sets. This consistency and the values of $R \simeq 0.2$ argue for the physical significance of the predicted effective dipole. From computer simulation studies we would expect the noise itself to produce $R \simeq 0.1$ with a similar contribution attributable to dewar positioning errors. It appears therefore that the misfit can be explained by experimental error without any significant contribution from model inadequacy. The dipole positions predicted (close to the calcarine fissure) are consistent with previous work using electrodes (Butler at al 1987, Halliday et al 1977).

For these latencies the upper quarter field data were more difficult to fit but consistent results were achieved for 90 ms and 102 ms. Again the suggested locations were broadly consistent with previous work with, in this case, a somewhat deeper cortical source.

During this period the half field response broadly corresponds to the sum of the two quarter field responses, indicating independent sources. In addition, the half field effective dipole appears to be midway between the two quarter field dipoles.

Table 10 indicates that the dominant sources during later peaks in power are unlikely to be located in the same cortical region as the P100m signal, though this conclusion must be tentative given the generally high R values involved.

Thus far I have only discussed the magnetic field signals. Current dipoles were not fitted to the electric potential data. However, the power curves for the electrode and magnetometer data show distinct peaks, but at different latencies, suggesting that the generators are not the same. The results were repeatable indicating that there were no significant problems relating to stationarity. This might indicate that dominant sources of the P100 recorded electrically are predominently radial. This is reasonable given that the fovea is represented around an occipital convexity a few cm above the inion.

The results presented in this chapter are confined to just one subject. Four other subjects were studied but, because of the time and discomfort involved in data acquisition,

the quality and quantity of the other data is not sufficient to add to the conclusions already noted. However, it is worth reporting that a similar latency shift between the electric and magnetic power peaks was a common feature.

Our conclusions are tentative but, in summary, they indicate that precise magnetic mapping allied with a careful analysis based on the dipole in a sphere model can indicate the existence of a wider range of source generators for this stimulus than was previously suspected. Combining electric and magnetic measurements should allow a fuller understanding of the retinotopic organisation corresponding to this and other VER data.

Conclusions And Further Work

The dipole in a sphere model has been shown to work well for spheres, part spheres, unless the dipole is very close to the boundary, and skulls, where dipoles are superficial. For other situations, proper use of the model requires account to be taken of the model sphere centre. In some systems (i.e deeper dipoles with the skull), the choice of sphere centre is highly significant to dipole prediction and full scanning of all reasonable alternatives is necessary.

The work reported above indicates that a prediction is robust if the sphere centre choice, within physically acceptable limits, does not affect the result significantly. Including the sphere centre in the fitting procedure gives information about the robustness of the model and predictive accuracy can be improved by intelligent choice of assumed sphere centre(s).

The dipole in a sphere model has been demonstrated to be useful for the two biological systems studied; namely chicks where the fitting suggested a non embryonic source which was subsequently confirmed, and human VER where use of the model suggested that the electric and magnetic generators of the P100 are different

Suggestions for further work can be divided into two

areas; analysis and systems. In particular the analysis needs to be extended to allow comparisons of the sphere model with the homogeneous head model (Meijs et al 1987) and there is also a need to evaluate the effects of inhomogenieties in more detail. In relation to the fitting procedures, a better analysis of the relevance of R is required so that misfit due to noise and misfit due to model inadequacy can be more easily discriminated. Finally the analysis should be capable of determining multiple dipoles. A tentative strategy, involving spatial segmentation of the data, has been suggested.

Many developments of the experiments on the biological systems are possible. Firstly chick electrolyte levels, which lead to the formation of liquid junction and membrane potentials, need to be determined as a function of development time. This will help to identify possible signal sources. In addition use of a miniature magnetometer will help to identify any components of the signal associated with the embryo itself.

In the case of brain studies, more precise visual stimuli (e.g separate octants of the visual field as opposed to just half and quarter fields) are needed to accurately map the retinotopic representation. Again a smaller magnetometer with better spatial resolution would be required. The immediate need is for more subjects to be used in order to properly verify the reported results

fully.

Finally, a cautionary note for further brain studies. In addition to improvements in the analysis, multiple SQUID sensors need to be used to reduce the data acquisition time and the signal to noise needs to be improved before MEG can be justified in clinical situations.

References

Armstrong, C.M
Ionic pores, gates and gating current. Quarterly Rev. Biophys. Vol 7 p179 - 210 1975

Balinsky, B.I
The extra embryonic structures in reptiles and birds. In Introduction to embryology . W B Saunders Philadelphia p254 - 259 1975

Barth, D.S and Sutherling, W
Simultaneous multichannel magnetic field measurements show approximately dipolar patterns of interictal spikes in complex partial epilepsy without apparent dipolar patterns in the scalp electric field. 6th Int. Conf. Biomag. p102 Tokyo 1987

Barth, D.S., Sutherling, W., Broffman, J. and Beatty, J.
Magnetic localization of a dipolar current source implanted in a sphere and a human cranium. Electro. Clin. Neurophysiol. Vol 63 p260 - 273 1986

Bennett, M.V.L. and Trinkaus, J.P.
Electrical coupling between embryonic cells by way of extracellular space and specialised junctions. J. Cell Biol. Vol 44 p592 - 610 1970

Bodemer, C.W.
The early development of the chick embryo. In Modern embryology. Holt, Reinhart and Wilson London 1970

Butland ,J
Simpleplot. Bradford University Research Ltd Bradford 1982

Butler, S.R., Georgio, G.A., Glass, A., Hancox, R.J. and Smith, K.R.H.
Cortical generators of the CI component of the pattern onset visual evoked potential'. Electro. Clin. Neurophysiol. Vol 68 p256-67 1987

Catterall, W.A.
Neurotoxins that act on voltage sensitive sodium channels in excitable membranes. Ann. Rev. Pharmacol. Toxicol. Vol 20 p15 - 43 1980

Cohen, D. and Hosaka, H.
Magnetocardiograms. Francis Bitter National Magnet Lab. MIT Vol 89 p41 1975

Coleman, J.R. and Terepka, A.R.
Fine structural changes associated with the onset of calcium, sodium and water transport by the chick chorioallantoic membrane. J. Membrane Biol. Vol 7 p111 - 127 1972

Cuffin, B.N.
The role of model and computational experiments in the biomagnetic inverse problem. Phy. Med. Biol. Vol 32 p33-43 1987

Cuffin, B.N.
Effects of fissures in the brain on electroencephalograms and magnetoencephalograms. J. Appl. Phys. Vol 57 p146 - 153 1985

Cuffin, B.N. and Cohen, D.
Magnetic fields of a dipole in special volume conductor shapes. IEEE Trans. Biomed. Eng. Vol 24 p372 - 381 1977

Cuffin, B.N. and Cohen, D.
Modelling magnetic fields of biological sources. Elect. Clin. Neurophysiol. Vol 47 p132 -146 1979

Fenwick, P.
The inverse problem; a medical perspective. Phys. Med. Biol. Vol 32 p5 - 11 1987

Geselowitz, D.B.
On the magnetic field generated outside an inhomogeneous volume conductor by internal sources. IEEE Trans. Mag. Vol MAG6 p346 -347 1970

Grove and Newell

Animal biology. UTP Oxford 1974

Halliday, A.M., Barret, G., Halliday, E. and Michael, W.F.
Cortical representation of checkerboard stimuli. In Visual evoked potentials in man: new developments. Eds J.E. Desmedt. Clarendon Press, Oxford 1977

Halliday, A.M., Butler, S.R. and Paul, R.
A text book of clinical neurophysiology. John Wiley Chichester 1987

Hamburger, V. and Hamilton, H.L.
A series of normal stages in the development of the chick embryo. J. Morphology Vol 88 p49 - 92 1951

Hamilton, H.L.
Lillie's development of the chick. Holt New York 1952

Hansen, J.S., Ko, H.W., Fisher, R.S. and Litt, B.
Practical limits on the biomagnetic inverse process determined from in vitro measurements of dipoles in spherical conducting volumes. Phys Med Biol Accepted 1987

Jaffe, L.F. and Nuccitelli, R.
An ultra sensitive vibrating probe for measuring steady extra cellular currents. J. Cell Biol. Vol 63 p614 - 628 1971

Jaffe, L.F. and Stern, C.D.
Strong electrical currents leave the primitive streak of chick embryos. Science Vol 206 p553 - 566 1979

Kaufman, L., Curtis, C. and Williamson, S.J.
Divided attention revisited: selection based on location or pitch. 6th Int. Conf. Biomagnet. Ibid

Kuffler, S.W. and Nicholls, J.G.
From neuron to brain. Sinauer Associates Inc. Sunderland 1986

Lennard, R.F.
The measurement of small ionic currents in living organisms by means of sensitive magnetometry. PhD thesis Open University, Milton Keynes 1984

Meijs, J.W.H., Bosch, F.G.C., Peters, M.J. and Lopes de Silva, F.H.
On the magnetic field distribution generated by a dipolar current source situated in a realistically shaped compartment model of the head. Electro. Clin. Neurophysiol. Vol 66 p286-98 1987

Melcher, J.
Dependence of the magnetoencephalogram on source orientation in the rabbit head. MS thesis MIT, Boston 1986

Narici, L.
Synchronization of brain activity revealed by neuromagnetic measurement. 6th Int. Conf. Biomagnet. Ibid

Nunez, P.L.
The brain's magnetic field: some effects of multiple sources on localization methods. Electro. Clin. Neurophysiol. Vol 63 p75-82 1986

Okada, Y.
Discrimination of localised and distributed current dipole sources and localized single and multiple sources. In Biomagnetism applications and theory. Eds H. Weinberg, G. Stroink and T. Katila. Pergammon Press New York 1985

Okada, Y., Lauritzen, M. and Nicholson, C.
MEG source models and physiology. Phys Med Biol Ibid

Pistella, F., Barone, P., Narici, L., Ocello, N., Pizzella, V. and Romani, G.L.
Improved procedure for neuromagnetic localisation. Phys. Med. Biol. Vol 32 p115 - 120 1987

Pizzella, V., Romani, G.L., Narici, L., Rossini, P., Salustri, C., Modena, I. and Cilli, M.
Magnetic brain topography under median nerve stimulation. 6th Int. Conf. Biomagnet. Ibid

Romanoff, A.L.

The avian embryo. Macmillan New York 1960

Sarvas, J.

Basic mathematical and electromagnetic concepts of the biomagnetic inverse problem. Phys. Med. Biol. Vol 32 p11 - 23 1987

SHE Corp

Biomagnetic probe BME06 Document No EL 330X 02A. SHE Corp San Diego 1980

Simkiss, K.

Water and ionic fluxes inside the egg. Amer. Zool. Vol 20 p385 - 393 1980

Stern, C.D. and Mackenzie, D.O.

Sodium transport and the control of epiblast polarity in the early chick embryo. J. Embryol. Exp. Morp. Vol 77 p73 - 98 1982

Stryer, L.

Biochemistry. Freeman San Francisco 1975

Swithenby, S.J.

SQUIDS and their applications in the measurement of weak magnetic fields. J. Phys. E Sci. Instr. Vol 13 p801 - 813 1980

Tripp, J.H.
Magnetic field distortion caused by boundaries. Biophys. J. Vol 18 p269-73 1977

Tripp, J.H.
Physical concepts and biological models. In Biomagnetism - an interdisciplinary approach. Eds Williamson, Kaufman, Modena and Romani. Plenium press New York p101 - 139 1983

Ueno, S., Wakisako, H. and Harada, K.
Flux reversal phenomena in spatial distributions of the MEG. In Biomagnetism Applications and Theory. Eds Weinberg, Stroink and Katilla Pergamon New York 1985

Weinberg, H., Brickett, P., Robertson, A. and Crisp, D.
Neuromagnetic investigation of steropsis. 6th Int. Conf. Biomagnet. Ibid

Weinberg, H., Brickett, P., Coolsma, F. and Baff, M.
Magnetic localisation of intracranial dipoles: simulation with a physical model. Electro. Clin. Neurophysiol. Vol 64 p159 - 170 1986

Williamson, S. and Kaufman, L.
Biomagnetism. J. Mag. Magnetic Materials. Vol 22 p129 - 201 1981

Zimmerman, J.

Magnetic quantities, units, materials and measurements. In Biomagnetism an interdisciplinary approach. Eds Williamson, Kaufman, Modena and Romani. Plenum New York 1983